



ATTENUATION AND REFRACTION OF AN ELECTROMAGNETIC  
WAVE IN AN ELECTRON BEAM GENERATED PLASMA

THESIS

Nathaniel P. Lockwood, Captain, USAF

AFIT/GAP/ENP/01M-06

DEPARTMENT OF THE AIR FORCE  
AIR UNIVERSITY

AIR FORCE INSTITUTE OF TECHNOLOGY

Wright-Patterson Air Force Base, Ohio

APPROVED FOR PUBLIC RELEASE; DISTRIBUTION UNLIMITED.

20010925 280



**ATTENUATION AND REFRACTION OF AN ELECTROMAGNETIC  
WAVE IN AN ELECTRON BEAM GENERATED PLASMA**

**THESIS**

Nathaniel P. Lockwood, Captain, USAF

AFIT/GAP/ENP/01M-06

**DEPARTMENT OF THE AIR FORCE  
AIR UNIVERSITY**

**AIR FORCE INSTITUTE OF TECHNOLOGY**

---

---

**Wright-Patterson Air Force Base, Ohio**

**APPROVED FOR PUBLIC RELEASE; DISTRIBUTION UNLIMITED.**

The views expressed in this thesis are those of the author and do not reflect the official policy or position of the United States Air Force, Department of Defense, or the U.S. Government

AFIT/GAP/ENP/01M-06

ATTENUATION AND REFRACTION OF AN ELECTROMAGNETIC WAVE  
IN AN ELECTRON BEAM GENERATED PLASMA

THESIS

Presented to the Faculty

Department of Engineering Physics

Graduate School of Engineering and Management

Air Force Institute of Technology

Air University

Air Education and Training Command

In Partial Fulfillment of the Requirements for the

Degree of Master of Science in Applied Physics

Nathaniel P. Lockwood, B.S.

Captain, USAF

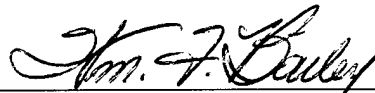
February 2001

APPROVED FOR PUBLIC RELEASE; DISTRIBUTION UNLIMITED

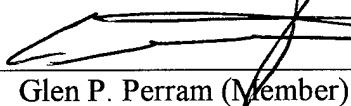
ATTENUATION AND REFRACTION OF AN ELECTROMAGNETIC WAVE  
IN AN ELECTRON BEAM GENERATED PLASMA

Nathaniel P. Lockwood, B.S.  
Captain, USAF

Approved:



\_\_\_\_\_  
William F. Bailey (Chairman)



\_\_\_\_\_  
Glen P. Perram (Member)



\_\_\_\_\_  
David E. Weeks (Member)

8 March 01  
date

8 Mar 01  
date

8 Mar 01  
date

### Preface

I wish to thank Dr. Bill Bailey for suggesting this wonderfully interesting topic and for his encouragement, suggestions, and guidance during my research. I would also like to thank my wife [redacted] for her patience, loving devotion and for helping me keep my sanity during the long months that it took to develop this report.

<u>Table of Contents</u>	Page
Preface .....	1
List of Figures .....	5
List of Tables.....	7
Abstract .....	8
I. Introduction.....	9
Objectives.....	10
Background .....	12
II. EM Wave Propagation in a Plasma .....	16
Refraction of an EM Wave in a Collisional Plasma.....	16
Ray Tracing using the Eikonal Method.....	17
Comparison of Eikonal Methods.....	18
Comparison of Analytic and Numeric Ray Tracing Results.....	23
Attenuation of an EM Wave in a Collisional Plasma.....	30
Implementation of the EM Wave Propagation Model (EMWPM).....	32
Description of Functions and Subroutines .....	35
EMWPM Inputs and Outputs .....	41
Capabilities of the EMWPM Program .....	41
III. Electron Impact Cross Section Theory.....	43
Background Theory of Scattering .....	43
Mott's Elastic Scattering Cross Section .....	46
Ionization Cross Section.....	48
Bethe's Relativistic Ionization Cross Section .....	48

Mott's Ionization Cross Section.....	51
Binary Encounter Bethe Ionization Cross Section.....	57
Comparison of Cross Section Results .....	61
IV. Electron Beam Propagation .....	67
Simple Electron Beam Propagation Model (SEBPM) .....	67
Axial Density Profile with No Angular Scattering .....	67
Model Theory .....	68
Numeric Model Theory.....	72
Results of Simple Electron Beam Propagation Model.....	73
Results of the RNE Scenario .....	74
Results of the ESE Scenario.....	75
Monte Carlo Method .....	80
Monte Carlo Techniques .....	81
Descriptive Statistics .....	87
Electron Beam Simulation (EBS) (Monte Carlo) Description.....	88
Design Philosophy.....	89
Inputs .....	92
Outputs .....	93
Description of Functions and Subroutines .....	94
Plasma Density Loss Mechanisms .....	100
Results of Plasma Chemical Reaction Calculations.....	106
V. Results and Conclusions.....	113
Plasma Density and Spatial Distribution.....	113

Static Plasma Distribution.....	113
EM Wave Attenuation and Refraction due to the Plasma Density Distribution.....	123
Distortion of the Electromagnetic Wave Front .....	123
Spatial Variations in Attenuation .....	128
Spatial Variations in Attenuation Considering Plasma Loss Mechanisms .....	135
Summary and Conclusions.....	135
Limitations of the Study and Recommendations .....	138
Appendix A: Derivation of the Radius of Curvature .....	140
Appendix B: Input Parameters for the EBS Simulation.....	145
Appendix C: Primary Chemical Reactions in the Plasma.....	148
Appendix D: Results of Rate Equation Calculations .....	155
Bibliography.....	159

## List of Figures

	Page
Figure 1. Trajectory of an EM Wave in a Layered Medium.....	16
Figure 2. Refraction an EM Wave Propagating Perpendicular to $\vec{\nabla}n$ .....	17
Figure 4. Comparison of Eikonal Methods in a Linearly Varying Plasma .....	25
Figure 5. Comparison of Methods in an Exponentially Varying Plasma .....	26
Figure 6. Symmetry Comparison of the Trajectory of an EM Wave.....	28
Figure 7. Check for a Constant Value of $n \sin \theta$ in a Medium with Parallel Strata .....	29
Figure 8. Diagram of a Cell in the Plasma Density Table.....	35
Figure 9. MainProg Flow Diagram from the EMWPM Program .....	39
Figure 10. PlasmaRefract Function Flow Diagram from the EMWPM Program.....	40
Figure 11. Rutherford Scattering Diagram.....	44
Figure 12. Total Ionization Cross Section from Bethe's Equation .....	51
Figure 13. Mott's Wave Vector Relationships.....	53
Figure 14. Mott's Angular Distributions for Molecular Nitrogen .....	56
Figure 15. Mott's Ejection Energy Distribution.....	57
Figure 16. Comparison of Mott and NIST differential cross sections .....	63
Figure 17. Comparison of Bethe, RBEB, Mott, and NIST Ionization Cross Sections .....	65
Figure 18. Diagram of Energy States in the SEBPM Numerical Method .....	73
Figure 19. Electron Longitudinal Density Profile from the RNE Scenario .....	75
Figure 20. Axial Profile of 1 MeV Electrons in ESE scenario .....	77
Figure 21. Axial Profile of 2 MeV Electrons in ESE scenario .....	77

Figure 22. Axial Profile of 5 MeV Electrons in ESE scenario .....	78
Figure 23. Flow Diagram of Main Program.....	90
Figure 24. Flow Diagram of SimControl. ....	91
Figure 25. EBS Setup, Electron Beam Propagation Direction, and Coordinate System .....	94
Figure 26. Comparison between the SEBPM and EBS Simulations Axial Electron Density Profile for the RNE scenario .....	99
Figure 27. Detachment Cross Sections .....	105
Figure 28. Log of Steady State Electron Density Versus Log of Electron Beam Source Term $\gamma$ .....	108
Figure 29. Ratio of Electron Densities with and without Loss Mechanisms.....	111
Figure 30. Plasma Distribution Results from the EBS simulation.....	115
Figure 31. Maximum Length and Displacement of Plasma versus Electron Energy at Various Altitudes.....	118
Figure 32. Plasma Profile versus Altitude.....	119
Figure 33. Transverse Distribution of the Electron Beam Generated Plasma .....	120
Figure 34. Contour Plot of Electron Beam Generated Plasma.....	123
Figure 35. Refraction in the Electron Beam Plasma at 5 km Altitude .....	128
Figure 36. Plot of the Imaginary Index of Refraction, $n_i$ , versus $\omega/\omega_p$ with a $v/\omega_p$ of 0.5 .....	130
Figure 37. Spatial Attenuation at 5 km Altitude .....	132
Figure 38. Attenuation versus Frequency at 5 km Altitude .....	134
Figure 39. Chemical Kinetics Results for Electron Beam Pulse of 5 ms .....	158

<u>List of Tables</u>	Page
Table 1. Comparison of Eikonal Methods in a Linearly Varying Plasma .....	24
Table 2. Comparison of Eikonal Methods in an Exponentially Varying Plasma .....	26
Table 3. Description of EMWPM Subroutines and Functions .....	36
Table 5. Results of Cascade Model for a RNE Scenario .....	74
Table 6. Results of ESE Scenario for Initial Energies of 1 MeV, 2 MeV, and 5 MeV .....	77
Table 7. Test for Energy Conservation for the RNE scenario .....	78
Table 8. Test for Energy Conservation for the ESE scenario .....	79
Table 9. SEBPM Minimum and Maximum Beam Length Results.....	79
Table 10. Description of Subroutines for the EBS Program.....	95
Table 11. Electron Energy Ranges.....	103
Table 12. Run Matrix .....	114
Table 13. EBS Parameters for all Simulation Runs .....	114
Table 14. Input Variables to EBS program.....	146
Table 15. List of Dominant Chemical Reactions for a Nitrogen-Oxygen Plasma.....	148

### Abstract

Artificially generated plasmas may be employed to alter the propagation characteristics of electromagnetic waves. The purpose of this report is to study the propagation of electromagnetic waves in an electron beam generated plasma. To understand the physics related to this concept requires the development of computational tools dealing with a plasma created by an electron beam, an assessment of the temporal and spatial evolution of the plasma, and a characterization of the refraction and attenuation of electromagnetic (EM) waves in a collisional plasma. Three computer programs were developed to characterize the effectiveness of an electron beam generated plasma in refracting and attenuating an EM wave. The spatial extent and density distribution of a plasma generated by a relativistic electron beam were determined using an axisymmetric Monte Carlo model. This plasma density distribution was used as a source term in the second code, a temporal solution of the plasma evolution based on a time dependent analysis of the plasma rate equations. The third code developed, evaluates the attenuation and refraction of an EM wave in the resulting plasma by using a ray tracing method based on the eikonal approach of Sommerfeld. The theoretical foundation and validation procedures are presented for each program. A limited exploration of the dependence of the plasma distribution on neutral densities and the electron beam energies was performed. For neutral densities corresponding to 5 km altitude, the plasma longitudinal extent ranged from 52 to 868 cm and the radial extent ranged from 18 to 292 cm for initial electron energies between 100 keV and 1 MeV respectively. Plasma chemistry plays a critical role in determining the electron plasma density and dictates the beam format required to achieve a desired level of EM wave attenuation.

# ATTENUATION AND REFRACTION OF AN ELECTROMAGNETIC WAVE IN AN ELECTRON BEAM GENERATED PLASMA

## I. Introduction

The purpose of this study is to examine the attenuation and refraction of an EM wave traversing an electron beam generated plasma. This chapter starts with a more detailed statement of the objectives of the study and then describes the general approach taken to achieve those objectives. The last part of the chapter gives background information on plasma characteristics that will be useful for the remainder of the study.

Chapter II first summarizes the theory of the refraction and attenuation of an EM wave propagating through a collisional plasma. The computer program, written to evaluate the refraction and attenuation of an EM wave traversing an electron beam generated plasma, is then discussed.

Chapter III provides background theory on electron collision cross sections that are used to model the plasma generation. The theoretical cross sections are compared with experimental values compiled by the National Institute of Standards and Technology (NIST). The comparison is done to validate the theoretical models as well as insure that they are implemented correctly.

In Chapter IV, the simple electron beam propagation model used to obtain bounding values for the densities and spatial extent of the plasma is introduced. The Monte Carlo based program used to determine the plasma density and spatial distribution is then discussed. The plasma loss mechanisms and a model for estimating the loss in the plasma density are then considered and addressed.

Chapter V presents a demonstration of the capabilities of the computer simulations that were developed in the first four chapters. Results from the computer simulations are discussed and conclusions are drawn. Finally, the limitations to the study and recommendations for future work are discussed.

### Objectives

The objective of this study is to examine the attenuation and refraction of an EM wave traversing an electron beam generated plasma. The significance of the spatially dependent attenuation will be cast in terms of a spatially averaged attenuation of the incident EM wave.

Specifically this study was designed to develop tools to determine:

1. The electron density distribution of a plasma generated by a relativistic electron beam.
2. The temporal and spatial evolution of the plasma density accounting for attachment and recombination.
3. The spatial attenuation and refraction of an EM wave with finite spatial extent due to the temporally evolving electron density distribution resulting from a relativistic electron beam. The spatial attenuation and refraction is determined as a function of certain electron beam and environmental parameters such as power, initial electron energy, air density and temperature.

The determination of the electron density and spatial distribution caused by a relativistic electron beam ionizing the air was approached in two phases. The first phase bounded the problem by examining the forward scattering case. This case assumes that the electrons are not scattered laterally and all energy lost by the initial electrons results

in the formation of new electrons through ionization. These assumptions result in an electron beam that travels straight through the air and decays only in energy as it propagates. The decay in energy is due to the ionizing collisions that occur when the incident electron, an electron from the electron beam, impacts the electrons of a neutral molecule. For these simplified cases, ionizing collisions result in a loss of energy to the incident electron and the formation of a new electron that has either zero energy or half the energy of the incident electron. The second phase accurately determines the electron density distribution using a Monte Carlo simulation. In the Monte Carlo simulation, a triple differential cross-section (TDCS) developed by Mott was used to determine the angular scattering of the incident electron, the amount of energy imparted to the ejected electron, and the ejection angle of the liberated electron after the collision. The results of the Monte Carlo simulation are smoothed using group statistics and used to determine a two-dimensional electron density distribution for the plasma.

The variation in plasma density over time was modeled from a rate equation standpoint using differential equations developed from the various attachment, recombination, and detachment processes that occur in the plasma. A Runge-Kutta numerical method was employed to solve seventeen first order non-linear differential equations. Those equations describe the temporal evolution of the concentrations of the various species in the plasma. To simplify the problem, only electron densities and densities of atomic and molecular nitrogen and oxygen and their respective positive and negative ions were considered in the calculations. The results of these calculations were used to modify the plasma density, so that it reflected the loss of electrons due to attachment and recombination processes.

The attenuation and refraction of the EM wave is calculated by using a ray tracing method based on the Sommerfeld eikonal method. This method propagates the wave through the plasma iteratively and determines the amount of refraction the wave undergoes based on the index of refraction of the plasma and its gradient. The amount the EM wave is attenuated, in general, depends on the frequency of the EM wave and the electron, positive and negative ion, and neutral density of the plasma and their respective temperatures.

### Background

Tonks and Langmuir used the word “plasma” in 1929 “to designate that portion of an arc-type discharge in which the densities of ions and electrons are high but substantially equal”(Sturrock, 1994:6). However, the term plasma has been broadened to describe the fourth state of matter in which a large number of the atoms or molecules of a gas have been ionized or have an electrical charge. Plasma also has the characteristic of being quasi-neutral and exhibiting collective effects. A parameter that is commonly used to describe the collective effects of a plasma is the plasma frequency. The plasma frequency describes the maximum undamped frequency at which the electrons oscillate in a plasma. The plasma frequency for an electron and positive ion plasma is described by the equation

$$\omega_p = \sqrt{\frac{4\pi n_e e^2}{m_e}} \quad (1)$$

where

$\omega_p$  = plasma frequency

$n_e$  = electron density

To evaluate the effects of a plasma on EM wave propagation, a dispersion relationship is developed for the plasma. The dispersion relationship enables us to determine the wavelength, the phase and group velocity, and the index of refraction of an EM wave in a plasma. If the index of refraction is complex then the EM wave will attenuate as it traverses the plasma. The simplest dispersion relationship is associated with a collisionless, cold plasma with no impressed magnetic field:

$$\omega^2 = \omega_p^2 + c^2 k^2 \quad (2)$$

where

$\omega$  = angular frequency of the EM wave

$k$  = the wave number ( $2\pi/\lambda$ )

A cold plasma is a plasma in which the thermal velocities of the constituents are negligible (Sturrock, 1994:73). From equation (2), we obtain an expression for the group velocity of an EM wave:

$$v_g = \frac{d\omega}{dk} = c \sqrt{1 - \frac{\omega_p^2}{\omega^2}} \quad (3)$$

and the index of refraction for that EM wave is

$$n = \sqrt{1 - \frac{\omega_p^2}{\omega^2}} \quad (4)$$

where

$v_g$  = group velocity

$n$  = index of refraction

However, plasmas in a dense gas, such as air at atmospheric pressure, have a large collision frequency between its constituents, therefore, we must use a dispersion

relationship for a collisional plasma. The dispersion relationship for a collisional, cold plasma is derived using an effective frictional force term combined with the forces on the electrons due to an EM wave

$$\vec{F}_{coll} = -m\nu\vec{v} \quad (5)$$

where

$\nu$  = collision frequency

$\vec{v}$  = particle velocity

Using Maxwell and Lorentz's equations, we obtain the following dispersion relationship

$$\omega^2 = \frac{\omega_p^2}{1 + i\frac{\nu}{\omega}} + c^2 k^2 \quad (6)$$

Using a hard sphere approximation, the collision frequency of electrons with neutral particles is given by

$$\nu = \frac{4}{3}\pi a^2 \bar{v} N_m \quad (7)$$

where

$$\bar{v} = \sqrt{\frac{8kT}{\pi m}} \quad (8)$$

$\nu$  = collision frequency of the plasma

$a$  = hard sphere radius of the molecules ( $a=1.2 \times 10^{-8}$  cm)

$\bar{v}$  = average thermal velocity of the electrons

$N_m$  = molecular number density of air

T = temperature of the electrons

(Ginzburg, 1984: 41). Equation (6) results in an index of refraction described by

$$n = n_r + i n_i \quad (9)$$

where

$$n_r = \left(1 + \frac{\omega_p^4 - 2\omega_p^2\omega^2}{\omega^2(\omega^2 + v^2)}\right)^{1/4} \frac{1}{\sqrt{1 + \frac{v^2\omega_p^4}{\omega^2(\omega^2 + v^2 - \omega_p^2)^2}}} \quad (10)$$

$$n_i = \left(1 + \frac{\omega_p^4 - 2\omega_p^2\omega^2}{\omega^2(\omega^2 + v^2)}\right)^{1/4} \frac{v\omega_p^2}{\sqrt{\omega^2(\omega^2 + v^2 - \omega_p^2)^2 + v^2\omega_p^4}} \quad (11)$$

Due to the index of refraction being complex in a collisional plasma, the EM wave will attenuate as it propagates through the plasma (Clemmow, 1976:188-189).

## II. EM Wave Propagation in a Plasma

### Refraction of an EM Wave in a Collisional Plasma

Snell's law is:

$$n_1 \sin \theta_1 = n_2 \sin \theta_2 \quad (1)$$

where

$n_1$  = index of refraction for the initial medium

$n_2$  = index of refraction for the final medium

$\theta_1$  = angle of EM wave in the initial medium with respect to normal

$\theta_2$  = angle of EM wave in the final medium with respect to normal

This simple equation describes the refraction of an EM wave as it passes from one medium to another with a different index of refraction and provides the foundation of geometric optics. An approximation of the refraction experienced by an EM wave using Snell's law can be obtained by considering a medium that slowly varies in index of refraction, such that it can be divided into discrete layers. The refraction of the EM wave is calculated at the boundary of each layer resulting in a curved trajectory of the EM wave as it traverses the medium. A sample trajectory of the EM wave is given in Figure 1.

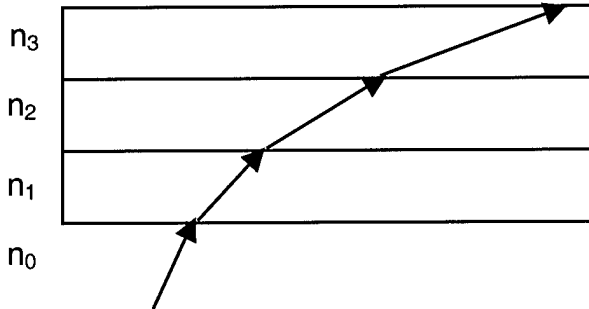


Figure 1. Trajectory of an EM Wave in a Layered Medium

where

$$n_0 > n_1 > n_2 > n_3$$

At the peak of the ray trajectory, the ray is parallel to the layers of changing index of refraction and perpendicular to  $\vec{\nabla}n$ . At the top of the trajectory, Snell's law fails us because it indicates that the ray would travel parallel to the layers without being refracted because the index of refraction is no longer changing. This failure is due to Snell's law considering the EM wave to be a ray with no spatial extent. If we consider the spatial extent and phase velocity of the EM wave, described by  $\frac{c}{n}$ , then at the top of the trajectory the lower portion of the EM wave will travel slower than the upper portion of the EM wave, hence causing the wave to refract downward (see Figure 2).

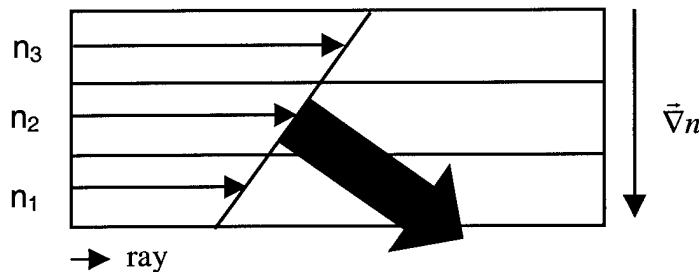


Figure 2. Refraction an EM Wave Propagating Perpendicular to  $\vec{\nabla}n$

The eikonal method (described in the next section), unlike Snell's law, considers the curvature of the phase front of an EM wave as it propagates through an inhomogeneous medium. Therefore, it will be used to determine the trajectory of an EM wave as it travels through the plasma.

#### Ray Tracing using the Eikonal Method

Eikonal is the name given to a function that describes the constant phase front of a wave. The most commonly used eikonals are planar, cylindrical, spherical, and quadratic. Geometric optics primarily utilizes planar waves while Fourier optics utilizes

planar, spherical, and quadratic phase fronts in a homogenous medium with discontinuities (i.e. lenses, aperture stops, prisms, etc.). The eikonal, however, is not restricted to those simple geometric forms for the phase front and in an inhomogeneous medium it may become very complex. The next section describes three different methods that utilize the eikonal function to determine the trajectory of a wave through an inhomogeneous medium.

### Comparison of Eikonal Methods

Three different methods of determining the refraction of a wave in an inhomogeneous medium were inspected for possible use as a means of propagating an EM wave through the plasma. All three of the methods inspected utilized the eikonal approach, however, each ray tracing method was developed differently. The following section compares these propagation methodologies.

The first ray tracing method evaluated was named the Sommerfeld Iterative Method (SIM) because it was based on the curvature vector equation developed by Sommerfeld. The curvature vector of a ray in an inhomogeneous medium is described by

$$\vec{K} = \frac{1}{n} (\vec{s} \times \vec{\nabla} n) \times \vec{s} \quad (2)$$

where

$\vec{K}$  = curvature vector

$\vec{s}$  = ray propagation unit vector

(Sommerfeld, 1964:339)(See Appendix A for details on the derivation of equation (2)). The magnitude of the curvature vector is the radius of curvature of the path of the EM wave as it is refracted in the medium. In Appendix A, it is shown that the curl of the

eikonal is zero; hence the change in the eikonal is path independent. Using that fact and the relationship

$$dL = R d\theta \quad (3)$$

where

$$R = 1/|\vec{K}| \quad (4)$$

$$dL = v_g dt \quad (5)$$

We can derive a first order differential equation that describes the rate of change of the angle of the ray propagation direction in the lab coordinates in an inhomogeneous medium. The rate of change of the angle,  $\theta$ , in an inhomogeneous medium is given by

$$\frac{d\theta}{dt} = v_g(x, y) |\vec{K}(x, y)| \quad (6)$$

and the rate of change of the x and y position of the ray is determined by the x and y components of the group velocity using the differential equations

$$\frac{dx}{dt} = v_g(x, y) \cos(\theta) \quad (7)$$

$$\frac{dy}{dt} = v_g(x, y) \sin(\theta) \quad (8)$$

Equations (6), (7), and (8) are then used to trace the ray path in an inhomogeneous medium. These equations appear to be benign at first, but no analytic solution has been obtained from them except for the trivial case of a homogeneous medium.

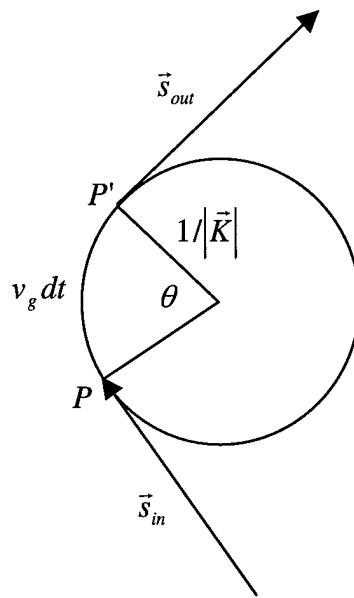


Figure 3. Diagram of the Sommerfeld Radius of Curvature

Haslegrove also developed a set of differential equations for ray tracing in an inhomogeneous medium. His equations are derived from the differential form of Snell's Law, but are very similar to the equations obtained in the SIM. The three first order differential equations are

$$\frac{dx}{dt} = \frac{c}{n^2} (n \cos(\theta) + \sin(\theta) \frac{\partial n}{\partial \theta}) \quad (9)$$

$$\frac{dy}{dt} = \frac{c}{n^2} (n \sin(\theta) - \cos(\theta) \frac{\partial n}{\partial \theta}) \quad (10)$$

$$\frac{dy}{dt} = \frac{c}{n^2} (\frac{\partial n}{\partial y} \cos(\theta) - \frac{\partial n}{\partial x} \sin(\theta)) \quad (11)$$

(Haslegrove, 1954:355-358). One notable difference between the two ray tracing methods is that the propagation velocity is the phase velocity of the wave,  $\frac{c}{n}$ , in Haslegrove's equations, where in the SIM the group velocity from Section I, equation (4) is used for the propagation velocity of the wave. Since, the group velocity is the rate at

which the energy and information travel through the medium, it is of more interest to us than the phase velocity. Equations (9) – (11) are intended for use in a curvilinear plane, a

curved two-dimensional plane, which is the reason for the  $\frac{\partial n}{\partial \theta}$  term. If the term  $\frac{c}{n}$  is

replaced by  $v_g$  and the  $\frac{\partial n}{\partial \theta}$  terms are set to zero then the Sommerfeld Iterative Method

and the Haslegrove Method are identical.

Budden also developed an analytic expression for the path of a ray in a linear and exponentially varying plasma. The analytic solution presented later in this section was obtained by using an integral equation Budden developed to trace the path of a ray in a medium that varies in index of refraction in only one-dimension (Budden, 1961:178).

The form of the integral is

$$x = - \int_0^z \left( \frac{\partial q}{\partial S} \right) dz \quad (12)$$

For a medium varying in one dimension the following relationships can be used

$$S = n \sin(\theta) \quad (13)$$

$$q^2 = n^2 - S^2 \quad (14)$$

Therefore

$$\frac{\partial q}{\partial S} = - \frac{S}{q} \quad (15)$$

$$x = S \int_0^z \frac{dz}{q} \quad (16)$$

For a medium that varies linearly in  $z$  and an EM wave that has angle of incidence,  $\theta_i$ , to the medium, the value of  $q$  becomes

$$q^2 = \cos^2 \theta_I - \frac{\alpha z}{f^2} \quad (17)$$

where

$f$  = frequency of the EM wave

$$\alpha = \frac{\omega_p(z)^2}{2\pi z}$$

Substituting (17) into (16) and integrating, we obtain the expression for the path of the EM wave through the linearly varying plasma

$$x = \frac{f^2 \sin 2\theta_I}{\alpha} - \frac{2f^2 \sin \theta_I}{\alpha} \sqrt{\cos^2 \theta_I - \frac{\alpha z}{f^2}} \quad (18)$$

It should be noted that the Budden's equation predicts that the path will be exactly parabolic. Next we will consider a plasma which exponentially varies in density in one dimension such that  $q$  has the form

$$q^2 = \cos^2 \theta_I - \frac{\omega_p(0)}{2\pi f} e^{\alpha z} \quad (19)$$

where

$$\omega_p^2 = \omega_p^2(0) e^{\alpha z} \quad (20)$$

$$\alpha = \frac{1}{z} \ln \frac{\omega_p^2}{\omega_p^2(0)} \quad (21)$$

Substituting (19) into (16) and integrating we obtain the expression for the path of the EM wave in an exponentially varying plasma

$$x = \frac{2 \sin \theta_I}{\alpha \cos \theta_I} \ln \left\{ \frac{\tan \frac{1}{2} \varphi_2}{\tan \frac{1}{2} \varphi_1} \right\} \quad (22)$$

where

$$\sin \varphi_2 = \frac{\omega_p(0)}{\omega \cos \theta_I} e^{\frac{1}{2} \alpha z} \quad (23)$$

$$\sin \varphi_1 = \frac{\omega_p(0)}{\omega \cos \theta_I} \quad (24)$$

SIM and Haslegrove's differential equations usually do not result in analytic solutions, but can be used to determine the trajectory of the ray using a standard numerical technique for solving differential equations. Haslegrove's equations are limited to use in a one-dimensional, curvilinear plane whereas the SIM can be used for a two or even three-dimensional varying plasma. Budden's equation for the limited cases of a one-dimensional, linearly and exponential varying plasma results in an analytic solution. However, for more complex medium an analytic solution is rarely obtained. There is also a two dimensional version of Budden's integral equations (Budden 1961:176), which can be used to determine ray trajectories using numerical integration techniques. This method, however, provides no capabilities above what has already been presented in this section.

#### Comparison of Analytic and Numeric Ray Tracing Results

To validate the Sommerfeld Iterative Method, a comparison of trajectory results was performed for the three methods described in the chapter. The first comparison case examined the trajectory of an EM wave in a plasma linearly varying in density in one-dimension. Figure 4.a shows the trajectory of an EM wave for all three eikonal methods in a plasma that increases in density linearly with increasing  $y$  values. From Figure 4.b, we see that the index of refraction of the plasma decreases with increasing plasma

density. We expect from Snell's law that the angle of the ray relative to the y axis would increase because  $n_2$  is less than  $n_1$  which results in  $\theta_2$  increasing to compensate.

Therefore, the ray refracts in the direction of  $\vec{\nabla}n$  over the entire path of the ray making a parabolic trajectory as seen in Figure 4.a. From the analytic result of Budden, we know that the trajectory in this ideal linearly varying plasma is perfectly parabolic.

Table 1 compares the differences between the trajectories in Figure 4.a by examining the differences between the y coordinate of the ray trajectories at corresponding x values. The analytic result of Budden and the numeric results of Haslegrove's equations are considered to be the correct answer because they are the established ray tracing methods.

Table 1. Comparison of Eikonal Methods in a Linearly Varying Plasma

Category	Measurement
Average difference between y coordinate at corresponding x coordinate for the SIM and Haslegrove's equations	253.74 m
Average difference between y coordinate at corresponding x coordinate for the SIM and Budden equation	254.28 m
Average difference between y coordinate at corresponding x coordinate for the Haslegrove's equations and Budden's equation	0.55 m

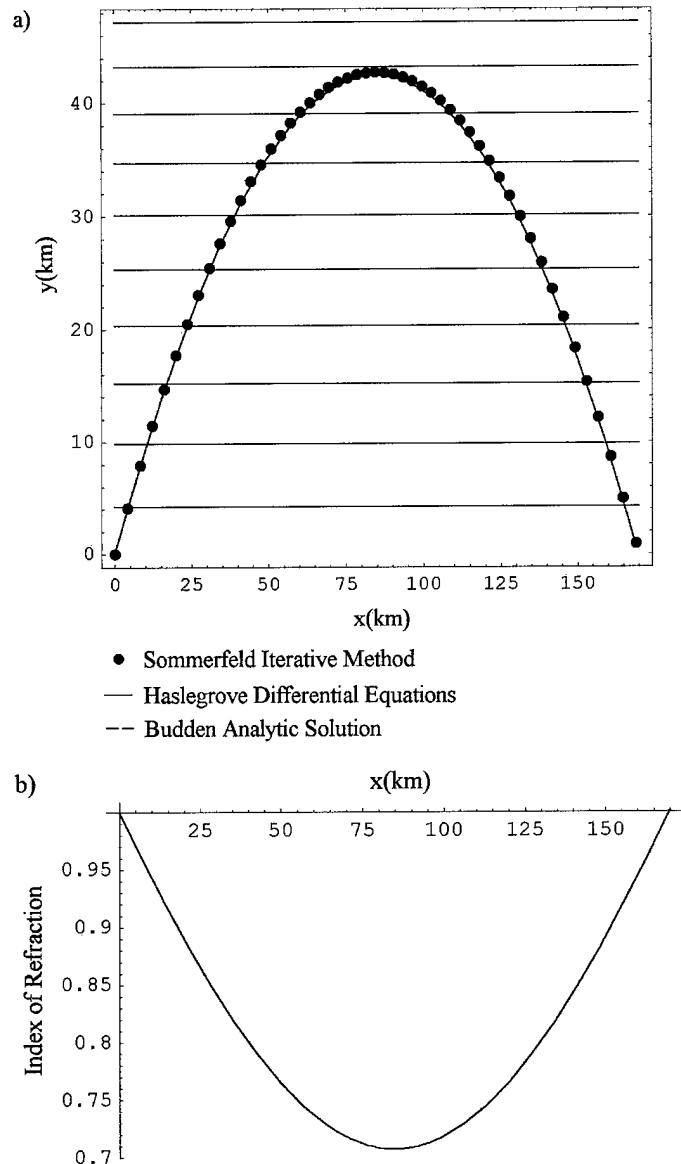


Figure 4. Comparison of Eikonal Methods in a Linearly Varying Plasma  
 a) Trajectory b) Index of Refraction

The second comparison case examined the trajectory of an EM wave in a plasma exponentially varying in density in one dimension.

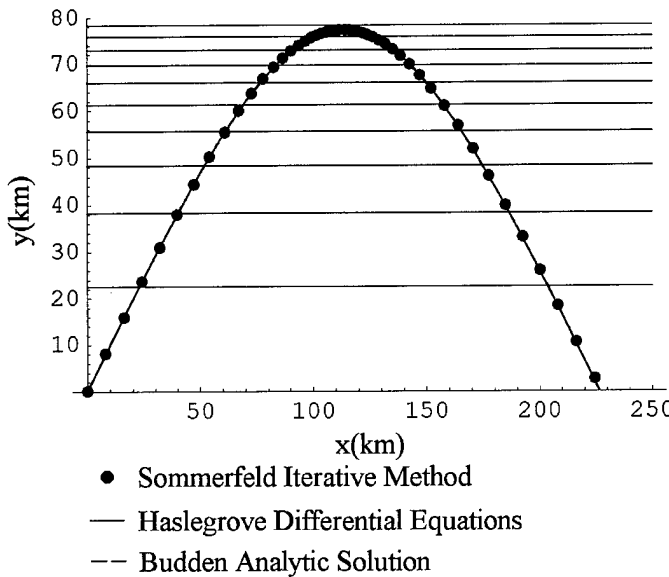


Figure 5. Comparison of Methods in an Exponentially Varying Plasma

The index of refraction decreases exponentially in the y direction, which results in a trajectory very similar to the linearly varying plasma case except that the trajectory is no longer parabolic. Figure 5 shows that the trajectories predicted by each method are close enough to each other that they are virtually indistinguishable.

Table 2. Comparison of Eikonal Methods in an Exponentially Varying Plasma

Category	Measurement
Average difference between y coordinate at corresponding x coordinate for the SIM and Haslegrove's equations	80.2 m
Average difference between y coordinate at corresponding x coordinate for the SIM and Budden equation	79.7 m
Average difference between y coordinate at corresponding x coordinate for the Haslegrove's equations and Budden's equation	0.51 m

A symmetry comparison between different implementations of SIM was performed to insure that the SIM was properly tracing the ray path of the EM wave. Due to an intuitive understanding of Snell's law and the analytic results of Budden, we expect

the path of an EM wave refracted by a plasma with perfectly parallel strata to refract through the atmosphere symmetrically (i.e. if the trajectory of the EM wave was folded in half, the halves should overlay each other and the time of travel should be the same for both halves of the trajectory). The following graph compares the symmetry of the calculated trajectory using various versions of SIM for an EM wave traversing a linearly varying plasma with parallel strata.

The three different implementations of SIM included:

- 1) Original Algorithm - This version of the algorithm represented the most basic implementation of SIM. It is simply a Euler numeric method that calculates the group velocity and radius of curvature of an EM wave at each x, y coordinate and alters the trajectory of the EM wave according to the magnitude of the radius of curvature at a particular point in the plasma.
- 2) Predictor-Corrector Methodology - uses the same methodology as the original algorithm to predict the next point of the trajectory of the EM wave. The P-C methodology then corrects the group velocity and radius of curvature by averaging their values over the path of the ray and uses these average values to determine the next point in the trajectory of the ray.
- 3) Symmetric Reflection Algorithm - this algorithm insures that when the EM wave is reflected in the plasma that the reflection is symmetric (i.e. the trajectory of the EM wave symmetric about the vector  $\vec{\nabla}n$ ). A reflection occurs when the Z component of the vector resulting from the cross product of the ray direction,  $\vec{s}$ , and  $\vec{\nabla}n$  changes sign. Symmetry is insured by transposing the position and angle of the EM wave before the

reflection about  $\vec{V}n$ . This is done so that the angle into the reflection point equals the angle exiting the reflection point resulting in a symmetric reflection.

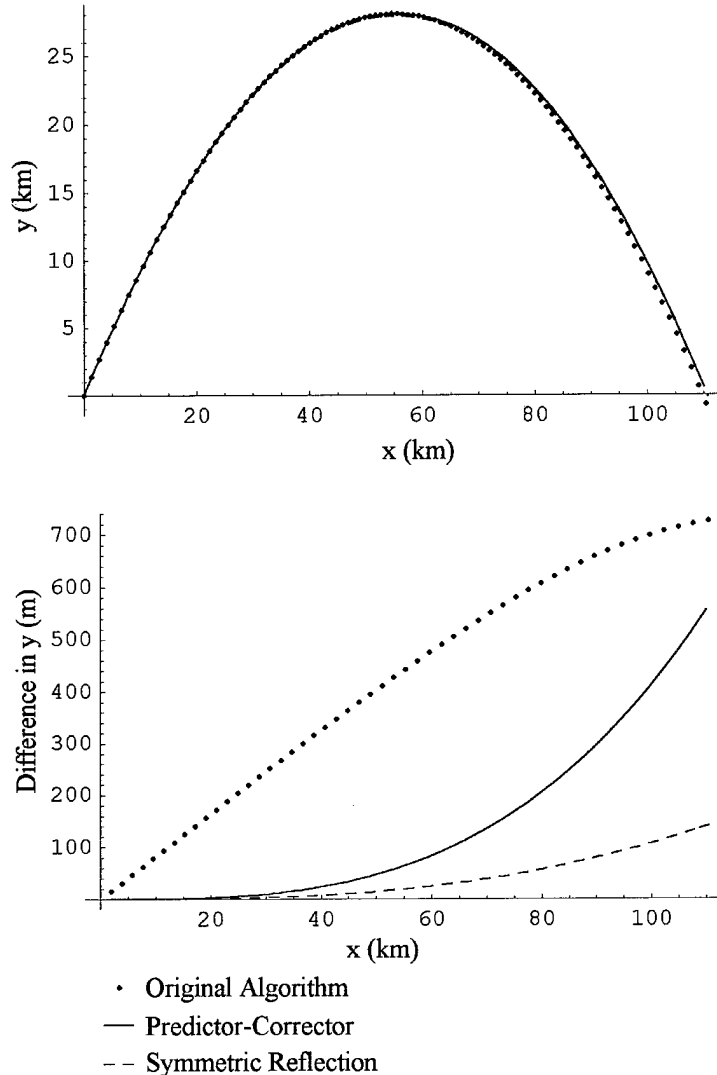


Figure 6. Symmetry Comparison of the Trajectory of an EM Wave in a Linearly Varying Plasma a) EM Wave Trajectory b) Comparison of Relative Difference in y Coordinate at Corresponding x Values over EM Wave Trajectory

Figure 6 indicates that the predictor-corrector and symmetric reflection algorithms make the trajectory of the EM wave substantially more symmetric which increases the accuracy of the trajectory, propagation time, path length of the EM wave. The accuracy

of the calculation of those quantities will be critical when determining the attenuation and refraction of the EM wave over very short distances of the plasma.

According to Sommerfeld, as a plane wave traverses a medium with changing index of refraction and parallel strata, the quantity  $n \sin \theta$  should remain constant. Therefore, a check to insure that the original SIM algorithm was maintaining a constant value of  $n \sin \theta$  was performed using an EM wave propagating through a linearly varying plasma. The following figure is a graph of  $n \sin \theta$  over the trajectory of the EM wave in Figure 4.

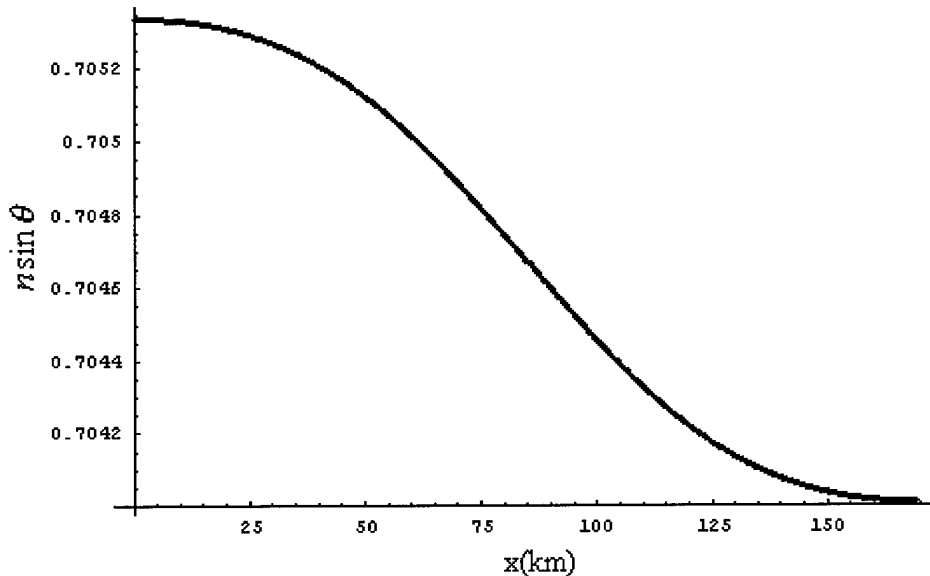


Figure 7. Check for a Constant Value of  $n \sin \theta$  in a Medium with Parallel Strata

It should be noted that the value  $n \sin \theta$  only varies in value by 0.001 over the entire trajectory of the ray.

This chapter presented the ray tracing methods of Haslegrove, Budden, and SIM as well as a comparison of these methods. The SIM compared well to the established analytic results of Budden and the numeric results of Haslegrove's equations. It also was

validated by the symmetry check and the constant  $n \sin \theta$  check. SIM also is capable of ray tracing in two or three dimensions. Therefore, the SIM will be the model of refraction used to determine the trajectory of an EM wave as it traverses the electron beam generated plasma. Since we have developed a means to calculate the refraction of an EM wave in a plasma, we now will develop the equations for the attenuation of an EM wave as it traverses the plasma.

### Attenuation of an EM Wave in a Collisional Plasma

The time-dependent wave equation derived from Maxwell's equations is

$$\vec{\nabla}^2 \vec{E} - \frac{k^2}{\omega^2} \frac{\partial^2 \vec{E}}{\partial t^2} = 0 \quad (25)$$

where the plane wave solution to the second-order differential equation is given by

$$\vec{E} = \tilde{E}_0 e^{i(\vec{k} \cdot \vec{r})} \quad (26)$$

and

$$\tilde{E}_0 = E_0 e^{-i(\omega t + \phi)} \quad (27)$$

where

$\tilde{E}_0$  = electric field phasor

$E_0$  = electric field amplitude

The wave number for the plane wave described in equation (26) is given by

$$k = \frac{n\omega}{c} \quad (28)$$

Since the index of refraction is complex, the wave number is complex, therefore

$$\vec{E} = \tilde{E}_0 e^{-(\vec{k}_i \cdot \vec{r})} e^{i(\vec{k}_r \cdot \vec{r})} \quad (29)$$

where the term  $e^{-(\vec{k}_i \cdot \vec{r})}$  represents the amplitude attenuation of the beam as it travels a distance  $\vec{r}$  through the medium. The attenuation of the EM wave intensity over a distance  $|\vec{r}|$  is expressed by

$$\Gamma_I = \frac{I_a}{I} = \frac{|\vec{E}_a|^2}{|\vec{E}|^2} = e^{-2(\vec{k}_i \cdot \vec{r})} \quad (30)$$

where

$\Gamma_I$  = intensity attenuation

$I_a$  = intensity of the attenuated EM wave

$I$  = intensity of the unattenuated EM wave

If we consider a plasma whose complex wave number is changing as a function of position in the plasma then a more appropriate attenuation equation is given by integrating the complex index of refraction over the path of the ray through the plasma. Integrating over the path of the ray results in the equation

$$\Gamma_I = \exp\left(-2 \int_{r_0}^{r_1} \vec{k}(r)_i \cdot d\vec{r}\right) \quad (31)$$

which describes the attenuation of an EM wave over its entire path through the plasma. Equation (31) will allow us to determine the intensity or power attenuation of an EM wave as it propagates through the plasma. In the next section equation (31) is combined with the SIM to create a high fidelity model of the refraction and attenuation of an EM wave in a plasma.

### Implementation of the EM Wave Propagation Model (EMWPM)

To estimate the attenuation and refraction of an EM wave as it traverses an artificially generated plasma, a wave propagation model capable of computing the trajectory and the attenuation of an EM wave at any frequency in a two-dimensional, inhomogeneous medium was required. To meet this requirement, a fortran program was written which combined the ray tracing method, SIM, the amplitude attenuation model given by equation (31), and a two-dimensional linear interpolation method (described later in this section).

SIM was incorporated into EMWPM by using a Euler predictor-corrector method with an adaptive step size (which is described in greater detail in the section, [Comparison of Analytic and Numeric Ray Tracing Results](#)). The predictor calculates the next step using the ray angle and group velocity at the current point. The corrector modifies the ray angle and group velocity by performing a weighted averaging of the curvature of the ray and the group velocity over the length of the predictor step, hence producing a more accurate step. If the distance between the end points of the predictor step and the corrector step are larger than the error threshold set by the user then the time step of the calculation is halved until the difference between the end points is within the error threshold.

The intensity attenuation of the EM wave is based on equation (31) where  $|\Delta\vec{r}_i|$  is the path length of each ray segment calculated by SIM and the imaginary part of the wave number,  $k_i$ , is given by

$$k_i = n_i \frac{\omega}{c} \quad (32)$$

where  $n_i$  is calculated from Chapter I, equation (12). From equation (31), the following equation was developed to calculate the total power attenuation of the EM wave as it propagates through the plasma

$$\Gamma_I = \exp\left[-2\sum_l \left|\vec{k}_i\right| \left|\Delta\vec{r}_l\right|\right] \quad (33)$$

The input to the EMWPM consists of a grid of densities of the plasma that are generated using the Electron Beam Simulation (which is described in Chapter IV). To reduce the number of grid points required to accurately sample the plasma density, a two dimensional linear interpolation method, based on the Taylor series expansion of a function of two variables, was used to determine the plasma density between grid points.

The linear interpolation is performed using the following equation

$$\hat{s} = \bar{s} + \frac{\Delta_x}{2} A + \frac{\Delta_y}{2} B + \frac{\Delta_{xy}}{2} AB \quad (34)$$

where

$$\bar{s} = \frac{m_1 + m_2 + m_3 + m_4}{4} \quad (35)$$

$$A = \frac{x - (x_2 + x_1)/2}{(x_2 - x_1)/2} \quad (36)$$

$$B = \frac{y - (y_2 + y_1)/2}{(y_2 - y_1)/2} \quad (37)$$

$$\Delta_x = \frac{m_3 + m_2}{2} - \frac{m_1 + m_4}{2} \quad (38)$$

$$\Delta_y = \frac{m_4 + m_3}{2} - \frac{m_1 + m_2}{2} \quad (39)$$

$$\Delta_{xy} = \frac{m_1 + m_3}{2} - \frac{m_2 + m_4}{2} \quad (40)$$

$m_n$  = plasma density at that point

$x_i, y_j$  = coordinates of the grid end points

(Kiemele, 1997:8-15). Figure 8 depicts the relationships between the coordinates  $(x_i, y_j)$  and the  $m_n$  variable. The terms  $\Delta_x$  and  $\Delta_y$  represent the change in the plasma density in the x and y direction and the term  $\Delta_{xy}$  represents the change in the plasma density in the diagonal direction. The terms A and B are the coordinate x and y, respectively, scaled to a value between -1 and 1. Using equations (34) – (40), the plasma density can be calculated for any point in a particular cell. As the EM wave propagates through the plasma, EMWPM determines the cell in the grid of electron densities, which is required for the SIM calculation. EMWPM then performs a linear interpolation using equations (34)-(40) to determine a closer approximation of the plasma density along the path of the EM Wave.

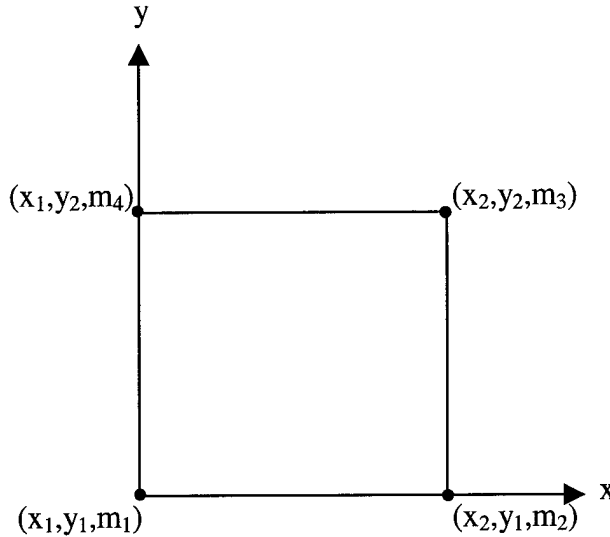


Figure 8. Diagram of a Cell in the Plasma Density Table where  $m_1$  is the Plasma Density at the Point  $(x_1, y_1)$

The SIM, attenuation, and linear interpolation algorithms described in this section provide the core of the EMWPM program. A further description of how these algorithms fit together is provided in the next section.

#### Description of Functions and Subroutines

This section describes the main algorithms and subroutines as well as the logical flow of the EMWPM program. For a top-level flow diagram of the EMWPM program see Figures 9 and 10. Table 3 contains a brief description of the functions and subroutines in the EMWPM program. The SIM method described in the previous subsections is incorporated into the EMWPM program via the subroutine `PlasmaRefractFunction`. The linear interpolation method described in the previous section is implemented in the `NumberDensity` subroutine and is essential to all calculations of the plasma frequency, index of refraction, group velocity, etc. of the EM wave in the plasma. The first column in Table 3 provides the name of the subroutine or

function in the EMWPM program. The second column gives a brief description of the function a particular subroutine followed by a more in-depth description of the subroutine.

Table 3. Description of EMWPM Subroutines and Functions

Subroutine Name	Brief Description
MainProg	<u>Main Program</u> Obtains input from the user from the Fortran function NAMELIST I/O, checks input files for errors, imports the plasma density table, calls the PlasmaRefractFunction, and outputs results (see Figure 9.). Results include the ray trajectory, group velocity, index of refraction, and intensity attenuation of the EM wave.
PlasmaRefractModule	
PlasmaRefractFunction	<u>Implements numeric solution of SIM Differential Equations</u> The controlling algorithm for the EMWPM program. PlasmaRefractFunction both controls the flow of the EMWPM and calls all the functions used to calculate the refraction and attenuation of the EM wave (see Figure 10 for details).
AirDensity	<u>Calculate <math>N_m</math></u> Calculates the air density at the altitude given by the user. AirDensity assumes the atmosphere is exponential and uses a scaling height of 8180 m (Al'pert, 1960:84)
CollisionFreq	<u>Calculate <math>v</math></u> Calculates the collision frequency between thermal electrons at a temperature specified by the user and neutral air molecules using Chapter I, equation (8).
NumberDensity	<u>Calculate <math>N_e</math></u> Determines the cell that a coordinate falls in by dividing the x and y coordinate of interest by the cell width and height respectively. This provides the location of the array element in the three dimensional array that describes the plasma density distribution. Once the density at the four corners of the cell is established, NumberDensity function linearly interpolates using equations (34) – (40) providing an estimate of the density at any point in between the cell's corners
PlasmaFreq	<u>Calculate <math>\omega_p</math></u> Calculates the plasma frequency using Chapter I, equation (1) based on the number density provided by the function NumberDensity.

GroupVelocity	<u>Calculate</u> $v_g$ Calculates the group velocity of the plasma using Chapter I, equation (4).
IndexofRefraction	<u>Calculate</u> $n$ , Calculates the real index of refraction of the plasma using Chapter I, equation (11).
WaveNumberImag	<u>Calculate</u> $k_i$ Calculates the imaginary wave number of the EM wave using equations (8) and Chapter I, equation (12).
GradIndexofRefraction	<u>Calculate</u> $\vec{\nabla}n$ Calculates the gradient of the index of refraction of the EM wave using a three-point difference formula in each direction with the $\Delta x$ specified by the user
PropagationDirection	<u>Calculate</u> $\vec{s}$ Calculates the ray propagation unit vector, $\vec{s}$ , in Cartesian coordinates using the equation $\vec{s} = \cos(\theta)\hat{x} + \sin(\theta)\hat{y}$ .
CurvatureVector	<u>Calculate</u> $\vec{K}$ Calculates the curvature vector describing the refraction of the EM wave as it propagates through the plasma using equation (2)
Magnitude	<u>Calculate</u> $ \vec{v} $ Calculates the magnitude of a vector
CrossProduct	<u>Calculate</u> $\vec{v}_1 \times \vec{v}_2$ Determines cross product of two arbitrary vectors
GetNewAngle	<u>Calculate</u> $\Delta\theta$ Computes a new angle of propagation for the ray by sampling the plasma density at the end points and the mid point of the predicted path of the ray. A new group velocity and radius of curvature is calculated for each of these points, then those values are averaged, using a weighted average toward the midpoint, to obtain a better estimate of the radius of curvature and group velocity of the ray. The averaged group velocity and radius of curvature are then used in equation (5) to determine the change in angle of the ray. The term $\nabla n \times \vec{s}$ , determines if the change in angle is added or subtracted from the initial angle. If $\nabla n \times \vec{s}$ is positive in the $\hat{z}$ then the change in angle is added to the initial angle, and if $\nabla n \times \vec{s}$ is negative the change in angle is subtracted.

Figures 9 and 10 provide an overview of how the subroutines described in Table 3 work together in the EMWPM program. Figure 9 describes the data flow in the EMWPM program for a time varying plasma. The logical flow of the subroutine, PlasmaRefractFunction, is presented in Figure 10 and is a direct result of the modified Euler method, the predictor-corrector algorithm, and the adaptive time step that are used to solve the SIM differential equations.

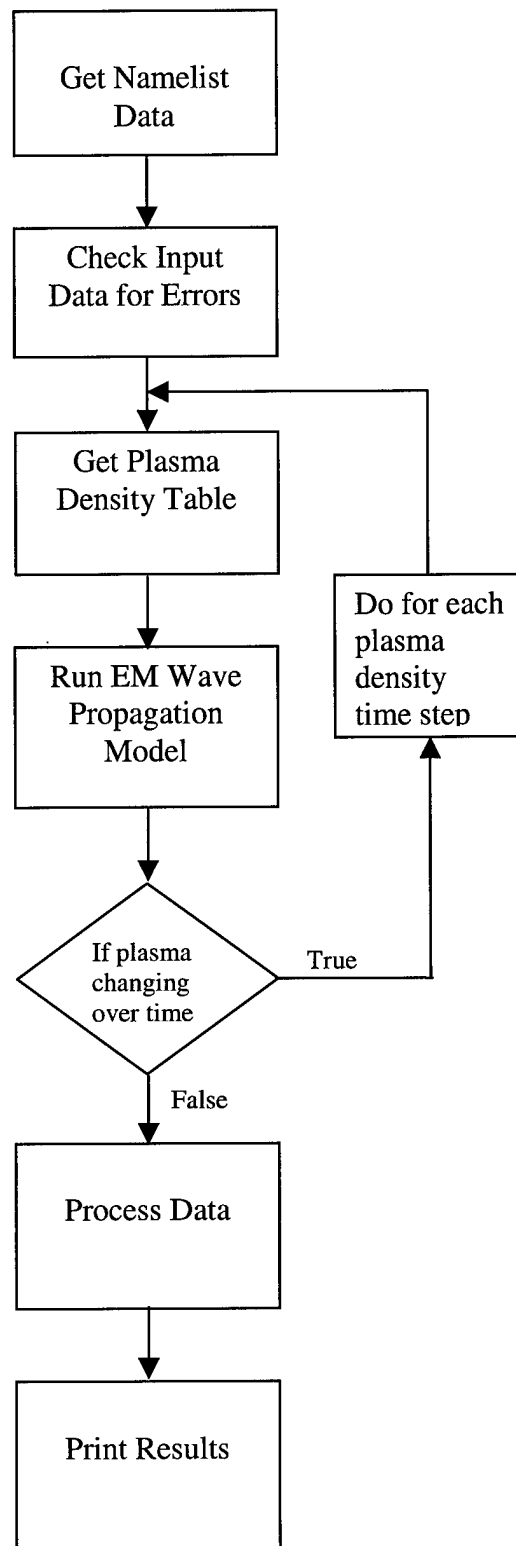


Figure 9. MainProg Flow Diagram from the EMWPM Program

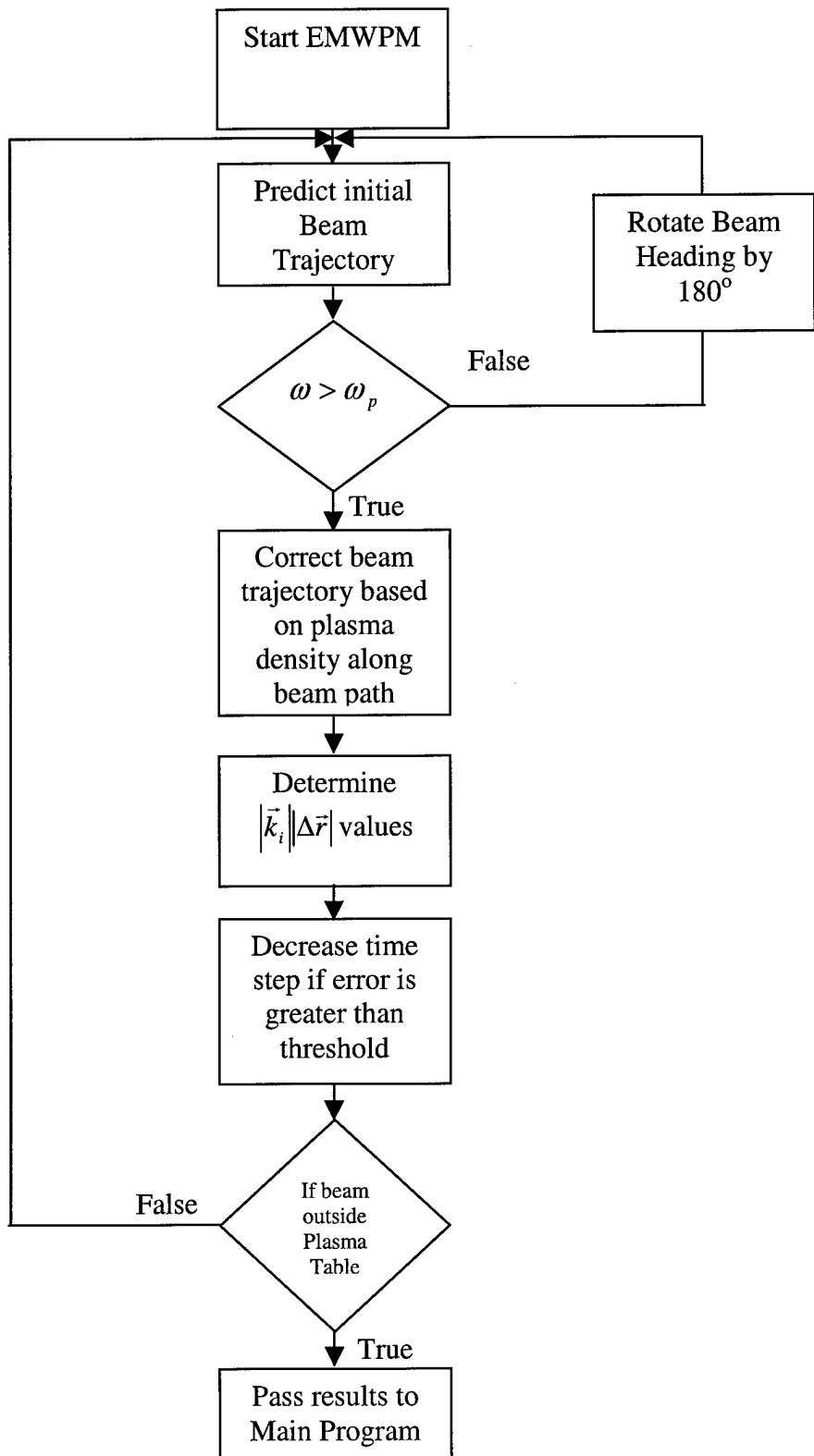


Figure 10. PlasmaRefract Function Flow Diagram from the EMWPM Program

### EMWPM Inputs and Outputs

The user controls the simulation EMWPM via a Fortran NAMELIST file. The file contains such parameters as the number of simulations to run, maximum dimensions of the plasma, initial starting point of the EM wave, number of rays, spatial extent of the modeled wave, average electron temperature and the frequency of the EM wave. The plasma density is read from a file containing the x and y position as well as the plasma density at those coordinates. If the plasma is varying in time, then a file describing the density of the plasma at each time step is required (This is acquired from Electron Beam Simulation described in Chapter IV).

EMWPM outputs a single file for each simulation run, containing data on the trajectory of the ray, propagation time, index of refraction,  $\vec{V}n$ , group velocity, ray attenuation, plasma frequency, and complex wave number,  $k_i$ . If multiple rays are simulated, the file is divided into multiple sections, with one section containing the complete history of one of the simulated rays. If multiple simulations are run, then multiple output files are produced with each file containing the ray trajectory histories for a certain set of parameters. If the plasma density varies in time then a file describing the ray path for each time step is produced as well.

### Capabilities of the EMWPM Program

The EMWPM program is a highly flexible beam propagation and attenuation model that allows the user to simulate multiple rays refracting and attenuating in arbitrary, inhomogeneous plasma. The multiple rays may be used to represent an EM wave of finite spatial extent refracting and attenuating in a plasma. The EMWPM is

capable of modeling an EM wave with any frequency in the Radio Frequency (RF) to optical range, but EMWPM assumes that the wave is at a single frequency (i.e. negligible bandwidth for purposes of attenuation and refraction). EMWPM is also capable of modeling an inhomogeneous plasma that varies in density over time.

Now that we have a program for determining the attenuation and refraction of the EM wave as it propagates in an arbitrary plasma, we must develop a means to describe the spatial density distribution of the plasma. Since the plasma will be generated through electron impact with air molecules, the next section will describe electron impact theory, which includes both elastic scattering and electron impact ionization of neutral molecules.

### III. Electron Impact Cross Section Theory

To develop a code to calculate the spatial extent and density distribution of the electron beam generated plasma, the collision cross sections between an electron and the molecules in the air must be obtained. Due to limited experimental data on electron impact ionization cross sections at electron energies between 2 keV and 5 MeV, we must use theoretical models to obtain the ionization cross sections for our plasma generation model. Currently there are several theories that have been developed to describe the cross section of an electron colliding with a neutral molecule. The elastic scattering cross sections discussed in this section deal with the electron scattering due to the coulomb field of the nucleus. The ionization cross sections deal with a free electron colliding with an atomic or molecular electron. Some of these models (such as Mott's ionization cross section) not only describe the probability that the incident electron will ionize the molecule, but also the energy lost and the angle scattered by the incident electron as well as the energy and direction of the ejected electron. This information can be used in a simulation that models the trajectories, energy loss, and number of ionizations that occur as a beam of electrons propagates through the air. From the results of such a simulation, we will be able to determine the density of the plasma generated by a relativistic beam of electrons ionizing the air.

#### Background Theory of Scattering

Rutherford scattering provides a classical view of how an electron is scattered by another charged particle due to the interaction of the electron with the coulomb field of the nucleus. Consider a fast electron passing near a nucleus of charge  $Ze$  and mass  $M$ .

The perpendicular distance between the electron velocity and the nucleus is referred to as the impact parameter,  $b$ . From Figure 11, we see that as the electron passes by the nucleus it is deflected by an angle  $\theta$  due to the coulomb attraction between the electron and the nucleus.

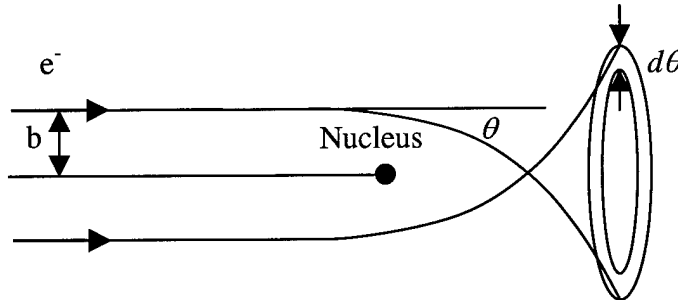


Figure 11. Rutherford Scattering Diagram

According to Fermi,

“The cross section for scattering of the incident particle at an angle  $\theta$  in the range  $d\theta$  is defined to be the total area perpendicular to the initial path of the particle such that if the particle passes through this area it is deflected by an angle  $\theta$  in  $d\theta$ .”

(Orear, 1949:35). The area perpendicular to the initial velocity of the electron that will scatter into the angle  $\theta$  in the range  $d\theta$  given by

$$d\sigma(\theta) = 2\pi b(\theta) db(\theta) = 2\pi b(\theta) \frac{db(\theta)}{d\theta} d\theta \quad (1)$$

Classical mechanics gives the following formula for the relationship between the angle of deflection and the ratio of the potential and kinetic energy for two particles interacting via a coulomb force (for details of the derivation see (Evans, 1955:843))

$$\tan \frac{\theta}{2} = \frac{Ze^2}{m_e v^2 b} \quad (2)$$

the impact parameter,  $b$ , being specified as:

$$b(\theta) = \frac{Ze^2}{m_e v^2} \cot \frac{\theta}{2} \quad (3)$$

We can calculate  $\frac{db(\theta)}{d\theta}$  for purposes of substituting into equation (1)

$$\frac{db(\theta)}{d\theta} = \frac{Ze^2}{2m_e v^2} \csc^2 \frac{\theta}{2} \quad (4)$$

giving us a single differential cross section (SDCS) described by

$$d\sigma(\theta) = \frac{\pi Z^2 e^4}{(m_e v^2)^2} b^2 \cot \frac{\theta}{2} \csc^2 \frac{\theta}{2} d\theta \quad (5)$$

To determine the expression for a particle scattered into a solid angle  $\Omega$  in the range of  $d\Omega$ , we can easily change equation (5) using an expression for a differential solid angle

$$d\Omega = 2\pi \sin \theta d\theta = 4\pi \sin \frac{\theta}{2} \cos \frac{\theta}{2} d\theta \quad (6)$$

resulting in the equation

$$d\sigma(\theta) = \frac{Z^2 e^4}{4(m_e v^2)^2} \frac{1}{\sin^4 \theta/2} d\Omega \quad (7)$$

Hence, we have developed the nonrelativistic, SDCS for the elastic scattering of an electron through the solid angle  $d\Omega$  in the laboratory frame of reference. To convert to a relativistic, differential cross section the following relationships can be used for the mass and velocity of the electron

$$v = \beta c \quad (8)$$

$$m = \frac{m_e}{\sqrt{1 - \beta^2}} \quad (9)$$

which results in the relativistic differential cross section

$$d\sigma(\theta) = \frac{z^2 Z^2 e^4}{4(m_e c^2)^2} \left( \frac{1 - \beta^2}{\beta^4} \right) \frac{1}{\sin^4 \theta/2} d\Omega \quad (10)$$

(Evans 1955:593). This equation results in a scattering angle distribution for an electron scattering off a bare nucleus of an atom. By integrating (10), we can obtain the total elastic scattering cross section of an electron with a bare nucleus. However, the equation has a singularity at a scattering angle of zero and from experiment we know that the probability of the electron scattering into the angle  $\theta = 0$  is not infinite. Therefore, a common method of circumventing the flaws in this classical approach is to use a lower limit of integration other than 0 (Lawson, 1988:257). The value of the lower limit is discussed in the next section, which presents a quantum mechanical approach to determining the elastic scattering angle distribution of the electron.

### Mott's Elastic Scattering Cross Section

Due to the Heisenberg uncertainty principle, the classical theory of scattering is limited to the domain where

$$\frac{2Zz}{137\beta} \gg 1 \quad (11)$$

(Evans, 1955:593). Thus Rutherford's scattering cross section is limited to slow electrons colliding with a nucleus containing many protons. Since the electrons that we are interested in will have energies on the order of  $10^6$  eV resulting in  $\beta \approx 1$  and a nuclei, with a Z of 7 or 8, therefore, a quantum mechanical treatment of the elastic scattering cross section will be required.

Using the relativistic Dirac theory of the electron and the First Born Approximation, Mott obtained the full form of the relativistic differential cross section of particles scattering

under the influence of a coulomb field. He then developed an approximate form yielding a differential cross section very similar to the Rutherford scattering cross section:

$$d\sigma(\theta) = \frac{z^2 Z^2 e^4}{4(m_e c^2)^2} \left( \frac{1 - \beta^2}{\beta^4} \right) \frac{\left[ 1 - \beta^2 \sin^2 \frac{\theta}{2} + \pi \beta \alpha (1 - \sin \frac{\theta}{2}) \sin \frac{\theta}{2} \right]}{\sin^4 \theta / 2} d\Omega \quad (12)$$

where the new term represents the effect of electron spin and indistinguishability on the scattering of the electron (Mott, 1965:235). Integrating equation (12) gives the total collision cross section, however equation (12) predicts that a singularity occurs at  $\theta = 0$ . From experiment we know that the probability of the electron scattering into the angle  $\theta = 0$  is not infinite. Therefore, a common method of circumventing this problem is to use a lower limit of integration other than 0 (Lawson, 1988:257). The minimum angle of scattering for an electron scattering off a nucleus will occur when the electron impact parameter is approximately the same as the atomic electron screening radius. According to Lawson,  $\theta_{\min}$  can be calculated by

$$\theta_{\min} = \frac{\lambda}{r_s} = \frac{\lambda \alpha^2 Z^{1/3}}{r_e} = \frac{\alpha Z^{1/3}}{\beta \gamma} \left( \frac{m_0}{m_e} \right) \quad (13)$$

(Lawson, 1988:257), where

$\lambda$  = de Broglie wavelength of the incident particle

$r_s = \frac{r_e}{\alpha^2 Z^{1/3}}$  = electron screening radius

$m_0$  = rest mass of the electron

The maximum angle of scattering for an electron scattering off a nucleus will occur when the electron undergoes a head on collision with the nucleus and therefore is  $\pi$ , except in the ultra-relativistic cases (Lawson, 1988:257). Therefore, the total elastic cross section

for an electron scattering off a nucleus after integrating equation (12) is described by the equation

$$\sigma = \frac{4\pi e^4 Z^2}{2c^4 \beta^4 m_e^2 \gamma^2} \left[ \alpha \pi Z \beta (\csc \frac{\theta_{\min}}{2} - 1) + \frac{1}{2} (\csc^2 \frac{\theta_{\min}}{2} - 1) + \alpha (\pi Z \beta + \frac{\beta^2}{\alpha}) \ln \left\{ \sin \frac{\theta_{\min}}{2} \right\} \right] \quad (14)$$

### Ionization Cross Section

Currently there are several theories that have been developed to describe the cross section of ionization for an electron impacting a neutral molecule. All of these models can be used to obtain the total ionization cross section of an electron impacting a neutral molecule. However, some of these models (such as Mott's ionization cross section) provide additional information such as the angular scattering distribution of the incident electron as well as the angle and energy distribution of an ejected electron. Using these distributions, we can develop a simulation that models the trajectories, energy loss, and number of ejected electron produced as an electron travels through the air. From those results, we will be able to determine the density of our plasma due to the electron beam firing into the air.

### Bethe's Relativistic Ionization Cross Section

Bethe performed a detailed quantum mechanical calculation using the First Born Approximation to determine the average energy lost by a fast particle when colliding with an electron bound to a nucleus. His perturbation calculation starts with the coulomb potential between the bound electron and the stationary nuclear charge,  $Ze$ . He then added two perturbation terms that represent the potential energy between the incident

particle and the nucleus and the bound electron. His solution was extended to atoms containing  $Z$  electrons by replacing the standard coulomb potential of a bare nucleus with a field due to a bare nucleus plus the field due to the  $(Z - 1)$  atomic electrons (Evans 1955:579). This results in a non-relativistic ionization cross section that is proportional to  $1/Q^2$ , where  $Q$  is the energy of the ejected electron, and an energy loss per unit path length described by

$$\frac{dT}{ds} = \frac{4\pi z^2 e^4}{m_0 V^2} NZ \ln\left(\frac{2m_0 V^2}{I}\right) \quad (15)$$

where

$T$  = kinetic energy of the incident electron

$V$  = velocity of the incident particle

$m_0$  = rest mass of the incident particle

$z$  = charge of the incident particle

$I$  is the geometric mean of all the ionization and excitation potentials of the atom involved in the collision.  $I$  is defined as

$$\ln I = \frac{1}{Z} \sum_{n,l} f_{n,l} \ln A_{n,l} \quad (16)$$

where  $f_{n,l}$  is the sum of the oscillator strengths for all optical transitions of the electron in the  $n, l$  orbital and is on the order of unity for most atoms.  $A_{n,l}$  is the mean excitation energy of the  $n, l$  orbital and its value is fairly close to the ionization energy of the orbital electrons for the outer-shell electrons. However, theoretical values of  $I$  for atoms other than hydrogen are hardly ever used because they are usually incorrect. Therefore, the experimentally determined values of  $I$  are commonly used (Evans 1955:579).

Bethe modified equation (21) to account for the Lorentz contraction of the electric field of a relativistic incident particle. This general result is applicable to soft collisions where the energy of the ejected electron is between  $Q_{min}$  and  $H$ , where  $Q_{min}$  is the minimum ejected electron energy and  $H$  is the maximum ejected electron energy considered. This modification results in the equation

$$\frac{dT_s}{ds} = \frac{2\pi Z^2 e^4}{m_0 V^2} NZ \ln\left(\frac{2m_0 V^2 H}{I^2(1-\beta^2)} - \beta^2\right) \quad (17)$$

(Evans, 1955:582). Evans states that equation (23) can be extended to all electron impact ionization collisions by making  $H = Q_{max} = T/2$ . This only results in an error of a few percent from a more exact expression for energy lost per unit path length. Hence, equation (17) becomes

$$\frac{dT}{ds} = \frac{2\pi e^4}{m_0 V^2} NZ \ln\left(\frac{m_0 V^2 T}{I^2(1-\beta^2)} - \beta^2\right) \quad (18)$$

A cross section can then be obtained by

$$\sigma = \frac{1}{N \frac{dT}{d(Ionization)}} \frac{dT}{ds} = \frac{1}{N} \frac{d(Ionization)}{ds} \quad (19)$$

which results in

$$\sigma = \frac{2\pi e^4}{m_0 V^2} \frac{Z}{I_{avg}} \ln\left(\frac{m_0 V^2 T}{I^2(1-\beta^2)} - \beta^2\right) \quad (20)$$

where

$I_{avg}$  = average ionization energy of an atom or molecule

The following graph displays the total ionization cross section of molecular nitrogen obtained from equation (20) versus the incident electron energy

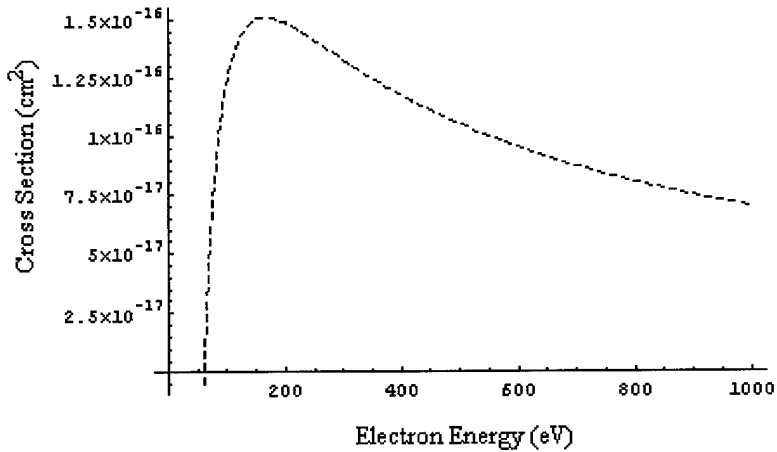


Figure 12. Total Ionization Cross Section from Bethe's Equation

#### Mott's Ionization Cross Section

Mott also obtained an electron impact ionization cross section for a fast electron impacting an electron bound by a generalized coulomb potential. Using the First Born Approximation, the differential cross section of a free electron colliding with a bound electron is obtained. The differential cross section of that collision is given by the expression

$$I_{mk}(\theta)dk d\omega = \frac{4\pi^2 m^2}{h^4} \frac{k_{mk}}{k} \left| \iint V \exp[i(k_{mk}\vec{n}_1 - k\vec{n}_0) \cdot \vec{R}] \psi_m^* \psi_m d\vec{r} d\vec{R} \right|^2 dk d\omega \quad (21)$$

where

$V$  = coulomb interaction energy between the incident and atomic

electrons  $e^2 / |\vec{r} - \vec{R}|$

$k$  = incident electron wave number

$\kappa$  = wave number of the continuous spectrum state

$m$  = initial primary quantum number of the bound electron

$k_{mk}$  = the wave number of the incident electron after ionization

$\psi_m$  = bound electron wave function

$\psi_\kappa$  = electron wave function in the continuous spectrum

$\vec{r} = \vec{r}_1 - \vec{r}_2$  = distance between the atomic and incident electron

$\bar{R} = \frac{1}{2}(\vec{r}_1 + \vec{r}_2)$  = coordinate of the center of mass of the electrons

Mott solved this equation using a wave function, developed by Sommerfeld, for an electron in the continuous spectrum,  $\kappa$ , moving in a direction corresponding with polar angles  $(\chi, \psi)$ . The Sommerfeld wave equation is given by

$$\psi_\kappa^* = \psi_\kappa(r, \pi - \Theta) = (2\pi)^{-\frac{3}{2}} \kappa \exp(i\kappa r + \frac{1}{2}n\pi) \int_0^\infty u^{-in} e^{-u} J_0 \left\{ 2\sqrt{i\kappa u \xi} \right\} du \quad (22)$$

where

$$\xi = r(1 + \cos \Theta)$$

$$\cos \Theta = \cos \theta \cos \chi + \sin \theta \sin \chi (\cos \phi \cos \psi + \sin \phi \sin \psi)$$

$$n = Z / \kappa a_0$$

(Mott, 1965:489). Mott obtained an ionization TDCS for a fast incident electron colliding with an atomic or molecular electron with a particular binding energy by assuming that the effects of interference between the ejected and incident electrons is small and hence negligible. Using this form of the wave equation (21), Mott obtained the differential cross section

$$I_\kappa(\theta) d\sigma d\omega dk = \frac{2^8 \mu^6 k_e}{\pi a_0^2 \Delta k^2} \frac{k_s}{k} \frac{\exp[-(2\mu/k_e) \tan^{-1} \{2\mu k_e / (\mu^2 + \Delta k^2 - k_e^2)\}] \times}{(1 - e^{-2\pi\mu/k_e})(\mu^2 + \Delta k^2 + k_e^2 - 2\Delta k k_e \cos \delta)^4} \times \frac{(\Delta k - k_e \cos \delta)^2 + \mu^2 \cos^2 \delta}{(\mu^2 + \Delta k^2 - k_e^2)^2 + 4\mu^2 k_e^2} d\sigma d\omega dk \quad (23)$$

where

$$\mu = Z_{\text{eff}} / a_0$$

$$\Delta k = \left| \vec{k}_s \hat{\vec{k}}_s - \vec{k} \hat{\vec{k}} \right| = \sqrt{(\vec{k}_s^2 + \vec{k}^2 - 2\vec{k}\vec{k}_s \cos\theta)}$$

$\delta$  = the angle between  $\vec{k}_s \hat{\vec{k}}_s - \vec{k} \hat{\vec{k}}$  and the direction described by  $(\chi, \psi)$

$(\chi, \psi)$  = electron ejection angles relative to the incident electron direction

$d\sigma$  = differential solid angle in which the electron is ejected

$(\theta, \phi)$  = electron scattering angle relative to the incident electron direction

$d\omega$  = differential solid angle in which the incident electron is scattered

$k_e$  = ejected electron wave number

$k_s$  = scattered electron wave number

$a_0$  = Bohr radius

Figure 13 summarizes the relationships between the wave vectors in this equation.

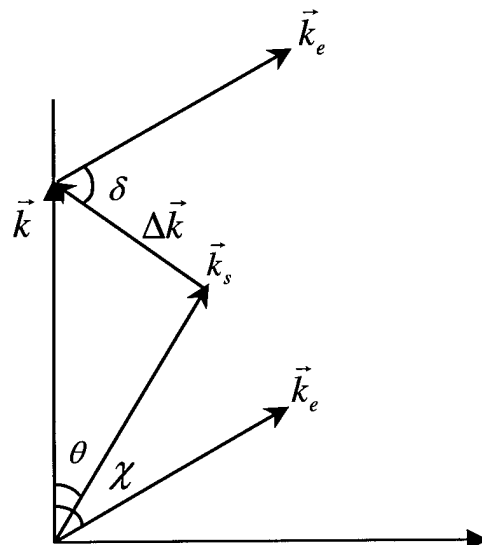


Figure 13. Mott's Wave Vector Relationships

The differential cross section, Equation (23), obtains its maximum value when  $\delta = 0$ , which corresponds to momentum being conserved among the electrons. The maximum of equation (23) is given by the conservation of momentum condition

$$k^2 + k_e^2 - 2kk_e \cos \chi = k_e^2 \quad (24)$$

(Mott, 1965:490). Mott's equation assumes that the velocity of the incident electron is much larger than the velocity of the bound electron, thus making the kinetic energy of the bound electron negligible. Therefore, the energy conservation condition can be written as

$$T = W + T_s + B \quad (25)$$

where

$T$  = incident electron energy

$W$  = ejected electron energy

$T_s$  = scattered electron energy

$B$  = binding energy of the atomic electron

and

$$T = \frac{\hbar^2 k^2}{2m_e} \quad (26)$$

Therefore,

$$k^2 = k_e^2 + k_s^2 + k_0^2 \quad (27)$$

From equation (23), the angular distribution of the scattered electron can be found by integrating over all angles of ejection. This can be accomplished by obtaining an expression for  $\cos \delta$  from the scalar product of  $\vec{k}_e$  and  $\Delta\vec{k}$  which results in the expression;

$$\vec{k}_e \cdot \Delta \vec{k} = |\vec{k}_e| |\Delta \vec{k}| \cos \delta \quad (28)$$

Solving equation (28) for  $\cos \delta$  in spherical coordinates yields

$$\cos \delta = \cos \theta \cos \chi + \cos \phi \sin \theta \cos \psi \sin \chi + \sin \psi \sin \chi \sin \theta \sin \phi - \cos \chi \quad (29)$$

The resulting analytic equation after integration is

$$I_\kappa(\theta) d\omega d\kappa = \frac{2^{10} \mu^6 k_e}{a_0^2 \Delta k^2} \frac{k_s}{k} \frac{\exp[-(2\mu/k_e) \tan^{-1}\{2\mu k_e / (\mu^2 + \Delta k^2 - k_e^2)\}]}{(1 - e^{-2\pi\mu/k_e})} \times \\ \frac{\Delta k^2 + \frac{1}{3}(k_e^2 + \mu^2)}{\{\mu^4 + 2\mu^2(\Delta k^2 + k_e^2) + (\Delta k^2 - k_e^2)^2\}^{\frac{3}{2}}} d\omega d\kappa \quad (30)$$

(Mott, 1965:490). Using equation (30) and (23), the scattering angle distribution of the incident electron and the angular and ejection energy distribution of the ejected electron can be determined for the collision of a free electron with an electron in a generalized coulomb field. It should be noted that equations (23) and (30) indicate that the ejected and scattered angle distributions are isotropic in  $\psi$  and  $\phi$  respectively. Figures 14 and 15 give an example of an ejected and scattered electron angular distribution for an electron in the  $3\sigma_g$  orbital of molecular nitrogen.

As the incident electron energy increases, small scattering angles become very favored, such that the scattering angle distribution peaks near  $\theta = 0$ . This indicates that at high electron energies, forward scattering of the incident electrons is highly favored. As a result of higher incident electron energies, the ejection angle distribution in Figure 14.b spikes at the angle corresponding to the conservation of momentum.

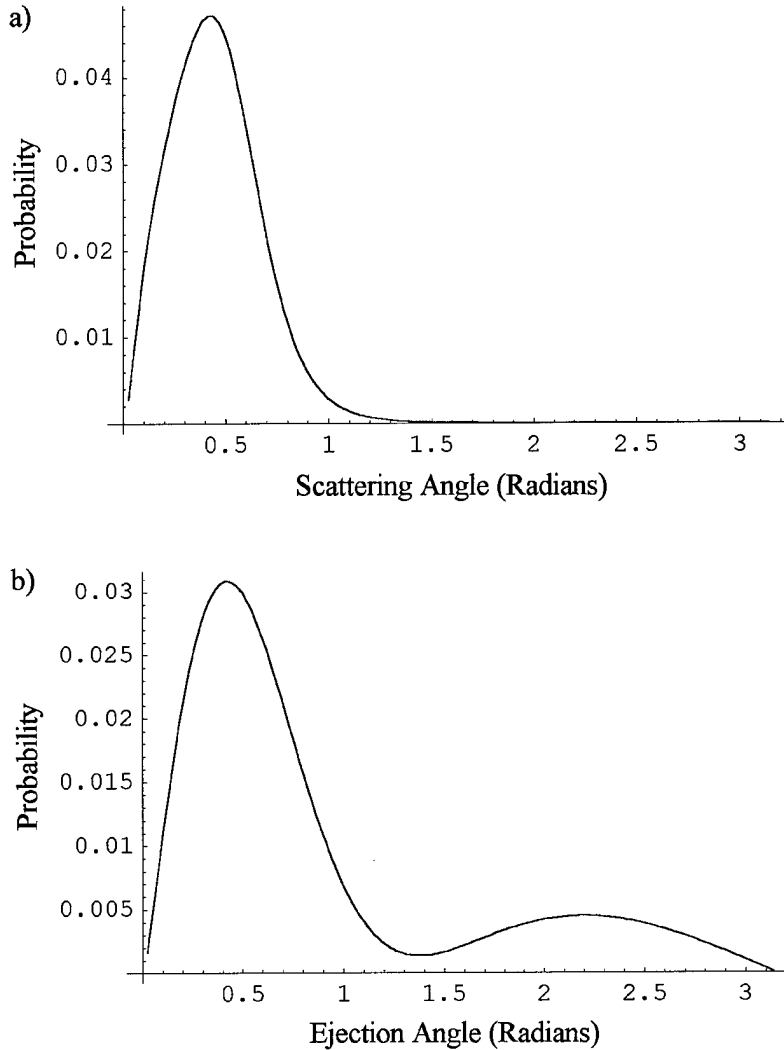


Figure 14. Mott's Angular Distributions for Molecular Nitrogen  
for an Incident Electron of 100 eV and Ejected Electron of 20 eV  
a) Scattering Angle b) Ejection Angle

The ejected electron energy distribution is calculated by integrating equation (30) over all ejection angles. This integration must be done numerically and results in an ejection energy distribution seen in Figure 15.

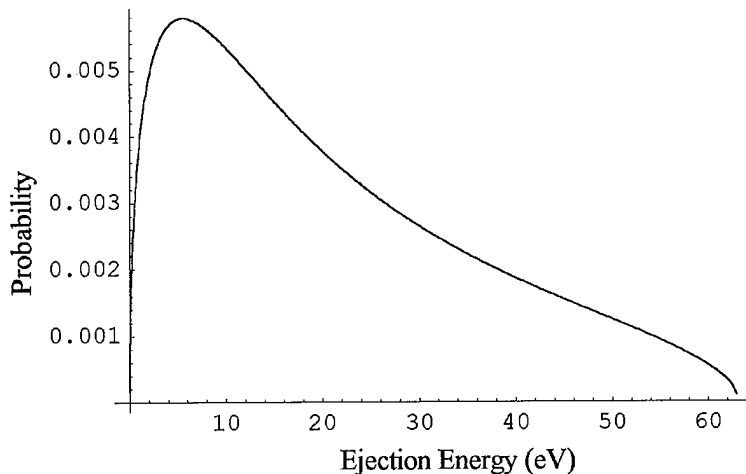


Figure 15. Mott's Ejection Energy Distribution for Molecular Nitrogen at an Incident Electron Energy of 80 eV

It should be noted that upon integrating Mott's TDCS (equation (13)) three times that the total cross section for a single electron in a particular orbital can be calculated. To obtain the total ionization cross section for the entire molecule, the cross section for each electron in each molecular orbital must be summed together. This method of calculating the total cross section of ionization is very computationally intense (considering that the simulation will need to calculate this quantity several million times to determine if an electron experiences an elastic or ionization collision), therefore an analytic equation is needed to obtain the total ionization cross section of a molecule.

#### Binary Encounter Bethe Ionization Cross Section

Kim and Rudd of NIST developed a SDCS, which they called the Binary-Encounter-Dipole model (Kim, 2000:052710-1). It uses a modified form of the Mott cross section for the collision of two electrons in the presence of a generalized coulomb potential

$$\left( \frac{d\sigma}{dW} \right)_{Mott} = \frac{4\pi a_0^2 R^2 N}{T} \left[ \frac{1}{(W+B)^2} - \frac{1}{(W+B)(T-W)} + \frac{1}{(T-W)^2} \right] \quad (31)$$

where

$R$  = the Rydberg energy

$N$  = orbital occupation number

This equation does not take into account dipole interactions, which are soft collisions that result in a small transfer of momentum to bound electrons. Therefore, the modified Mott cross section is combined with the Bethe cross section for soft collisions to obtain the BED equation. Kim and Rudd required that the combined Mott and Bethe formula satisfy asymptotic forms for both the ionization and stopping cross sections of Mott and Bethe. This requirement succeeded in eliminating empirical parameters that had been used in previous attempts to combine the two equations. The SDCS form of the BED is given as

$$\left( \frac{d\sigma}{dW} \right)_{BED} = \frac{S}{B(t+u+1)} \left[ \frac{\frac{N_i/N-2}{t+1} \left( \frac{1}{w+1} + \frac{1}{t-w} \right) + [2-(N_i/N) \times]}{\left[ \frac{1}{(w+1)^2} + \frac{1}{(t-w)^2} \right] + \frac{\ln t}{N(w+1)} \frac{df}{dw}} \right] \quad (32)$$

where

$$S = 4\pi a_0^2 N (R/B)^2 \quad (33)$$

$$t = T/B \quad (34)$$

$$u = U/B \quad (35)$$

$$w = W/B \quad (36)$$

$$N_i = \int_0^\infty \left( \frac{df}{dw} \right) dw \quad (37)$$

$$\frac{df}{dw} = \text{differential dipole oscillator strength}$$

$U$  = orbital energy of the bound electron

To obtain the relativistic BED equation, Kim and Rudd convert the nonrelativistic electron velocities and energies into their relativistic counterparts:

$$\beta_t = \frac{v_t}{c} \quad \beta_t^2 = 1 - \frac{1}{1+t'^2} \quad t' = T/mc^2 \quad (38)$$

$$\beta_b = \frac{v_b}{c} \quad \beta_b^2 = 1 - \frac{1}{1+b'^2} \quad b' = B/mc^2 \quad (39)$$

$$\beta_u = \frac{v_u}{c} \quad \beta_u^2 = 1 - \frac{1}{1+u'^2} \quad u' = U/mc^2 \quad (40)$$

where

$v_t$  = the relativistic speed of an electron with energy T

$v_b$  = the relativistic speed of an electron with energy B

$v_u$  = the relativistic speed of an electron with energy U

Substituting relationships (38) to (40) into equation (32) we obtain the following equation:

$$\left( \frac{d\sigma}{dw} \right) = \frac{4\pi a_0^2 \alpha^4 N}{2b'(\beta_t^2 + \beta_u^2 + \beta_b^2)} \left[ \begin{aligned} & \frac{N_i/N - 2 \left( \frac{1}{w+1} + \frac{1}{t-w} \right) \frac{1+2t'}{(1+t'/2)^2}}{t+1} \\ & + [2 - (N_i/N)] \left[ \frac{1}{(w+1)^2} + \frac{1}{(t-w)^2} + \frac{b'^2}{(1+t'/2)^2} \right] \\ & + \frac{1}{N(w+1)} \frac{df}{dw} \left[ \ln \left( \frac{\beta_t^2}{1-\beta_t^2} \right) - \beta_t^2 - \ln(2b') \right] \end{aligned} \right] \quad (41)$$

By integrating equation (41) over w from 0 to  $(t-1)/2$ , we obtain an expression for the total ionization cross section. The limit  $(t-1)/2$  is the maximum amount of energy that

is given to the ejected electron due to the assumption that the electron leaving the collision volume with the most energy is the incident electron. Since the differential dipole oscillator strength term,  $\frac{df}{dw}$ , is not always known for a molecule it is approximated by Kim and Rudd using a simple function that simulates the shape of  $\frac{df}{dw}$  in the ionization of the hydrogen atom. In the case when no data is available for the dipole constant, Kim and Rudd set the dipole constant of the molecule equal to one (Kim, 2000:0527103). This approximation results in the relativistic Binary-Encounter-Bethe model, given by the expression

$$\sigma_{RBEB} = \frac{4\pi a_0^2 \alpha^4 N}{2b'(\beta_t^2 + \beta_u^2 + \beta_b^2)} \left[ \frac{1}{2} \left[ \ln \left( \frac{\beta_t^2}{1 - \beta_t^2} \right) - \beta_t^2 - \ln(2b') \right] \left( 1 - \frac{1}{t^2} \right) + 1 - \frac{1}{t} - \frac{\ln t}{t+1} \frac{1+2t'}{(1+t'/2)^2} + \frac{b'^2}{(1+t'/2)^2} \frac{t-1}{2} \right] \quad (42)$$

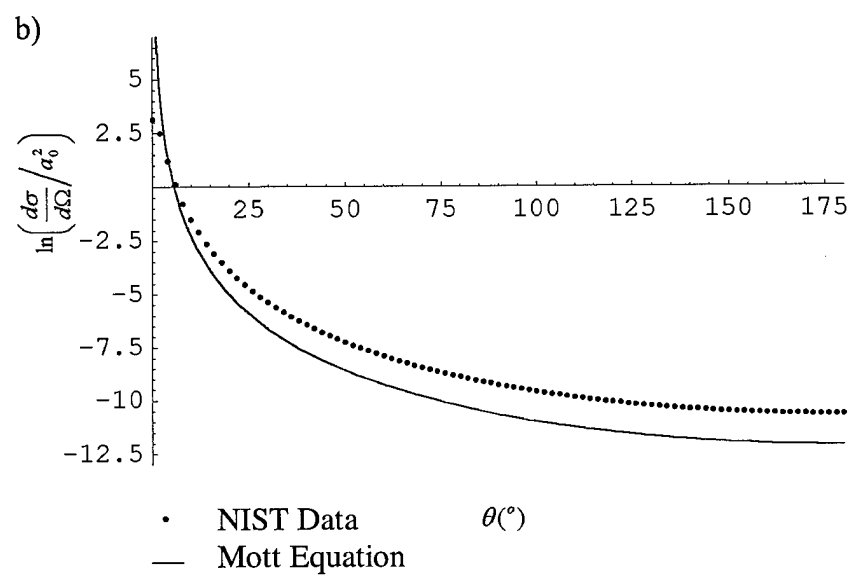
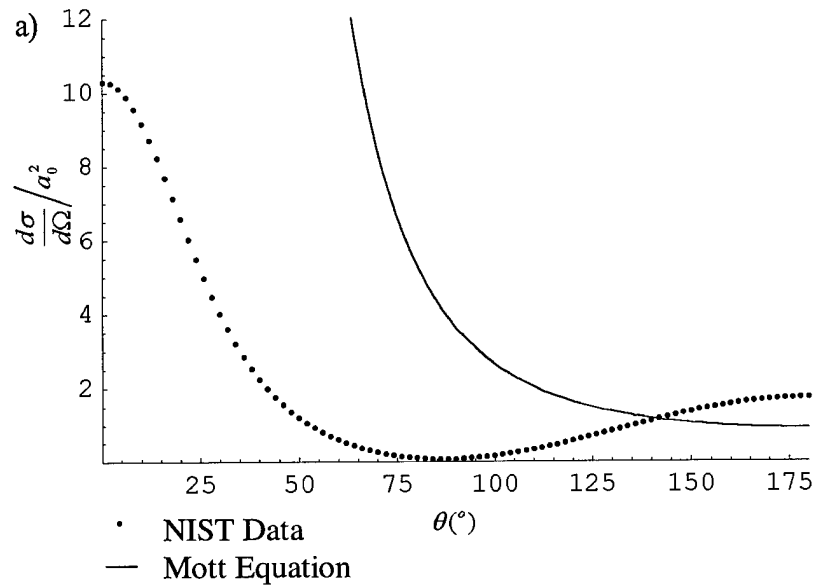
The relativistic form of this equation is required for electron energies greater than 20 keV, however this formula reduces to the non-relativistic BEB equation in the low energy limit (Kim 2000:0527101). This equation describes the ionization cross section for atomic or molecular electrons in a given orbital, and thus allows us to be specific about which molecular electron that the incident electron ionizes. To obtain the total ionization cross section for a molecule, the cross sections for each shell are added together.

The reason that three ionization cross sections are reviewed in this section is because they all have their strengths and weaknesses for being used in the electron beam model. Bethe's cross section requires minimal information and computation (average ionization energy, I, from equation (16), and Z) to provide a total ionization cross section for a molecule. Mott's equation (23), however, provides the ability to calculate the

scattering angle distribution of the incident electron as well as the ejected angle and energy distributions of the liberated electron. Mott's equation (23) allows us to develop a sophisticated model of the electrons propagating through the air. Mott's equation needs to be numerically integrated three times in order to obtain a total ionization cross section, which is overly computationally intense for a Monte Carlo simulation. Therefore, the RBEB model is a good complement to Mott's equation because it provides an analytic solution for the total ionization cross section of an orbital shell and has been extensively validated with experimental data. Therefore, a combination of the two models was used in the Monte Carlo simulation that is described in Chapter IV. In the simulation, Mott's elastic cross section model and the RBEB model calculate the total elastic and ionization cross sections respectively, which enables the Monte Carlo simulation to determine if the electron experiences an elastic or ionization collision. If the electron undergoes an ionization collision, then Mott's ionization equation provides the scattering and ejected angle distribution as well as the ejection energy distribution, which determines the energy and direction of the scattered and ejected electrons after the collision with the air molecule.

#### Comparison of Cross Section Results

A comparison of Mott's differential elastic cross section, equation (12), with data from NIST's elastic scattering data base was performed at incident electron energies of 50, 10,000, and 20,000 eV for atomic nitrogen. Since no data has been found comparing Mott's equation (12) to experimental data and NIST has extensively validated their model with experimental results, it is appropriate that we compare the more simplistic model of Mott to the NIST model developed by Jablonski, *et. al.*



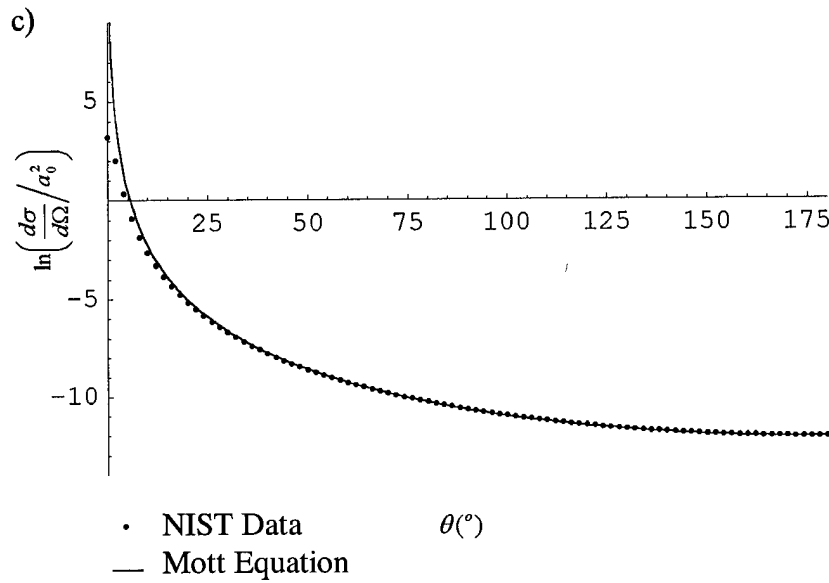


Figure 16. Comparison of Mott and NIST differential cross sections  
a) 50 eV b) 10,000 eV and c) 20,000 eV

From Figure 16.a, we see a large difference between the Mott and NIST differential cross sections. This is due to the first Born approximation no longer being valid when a slow electron (50 eV) interacts with a small nucleus. However, Figure 11.b and 11.c show that at greater incident electron energy, the first Born approximation becomes valid. Hence, the NIST and Mott differential cross sections are very similar at high incident electron energies. Since, the electrons we are concerned with are in the greater than 10 keV range (electrons with energies less than 10 keV do not travel very far through the air (<1 cm)), therefore, Mott's differential cross section equation is adequate for describing the scattering angle distribution of the electrons at these higher energies.

A comparison between NIST ionization cross section data and the relativistic Bethe, Mott, and RBEB total ionization cross section of nitrogen was also performed. For the Mott and RBEB ionization cross sections only the first four orbital shells were

used in the computation. This is because the inner shells do not contribute significantly to the ionization cross section and also RBEB and Mott's equations do not accurately model the ionization of inner shell electrons (Kim, 2000:052710-10). The molecular orbital constants for nitrogen are given in Table 4. To calculate Mott's ionization cross section, an effective Z must be obtained for the variable  $\mu$ . Since an effective Z is due to the shielded coulomb field that is acting on the electrons in their molecular orbital, the measured binding energies were used to calculate an effective Z using the equation

$$Z = \sqrt{\frac{2Ba_0}{e^2}} \quad (43)$$

$B$  = binding/ionization energy of the electron

Table 4. Molecular Orbital Constants of Nitrogen

Molecular Orbital	Binding Energy (eV)	Average Kinetic Energy (eV)	Electron Occupation Number	Dipole Constant
$1\sigma_g$	427.41	601.38	2	1
$1\sigma_u$	427.30	602.40	2	1
$2\sigma_g$	41.72	71.13	2	1
$2\sigma_u$	21.00	63.18	2	1
$1\pi_u$	17.07	44.30	4	1
$3\sigma_g$	15.58	54.91	2	1

Remarks: Data was obtained from (Kim, 2000)  
Binding energy from experimental vertical ionization energy

For Bethe's equation an average ionization energy of 36.6 eV (Evans, 1955:659) and  $I$  value of 86 eV (Evans, 1955:583) were used in the calculation. It was unclear what the

appropriate value for Z should be for molecular nitrogen, therefore the two extreme values of 7 and 14 were used to determine the possible range of Bethe's total ionization cross section. This determination of the extreme values for Bethe's total ionization cross section is shown in Figure 17.a.

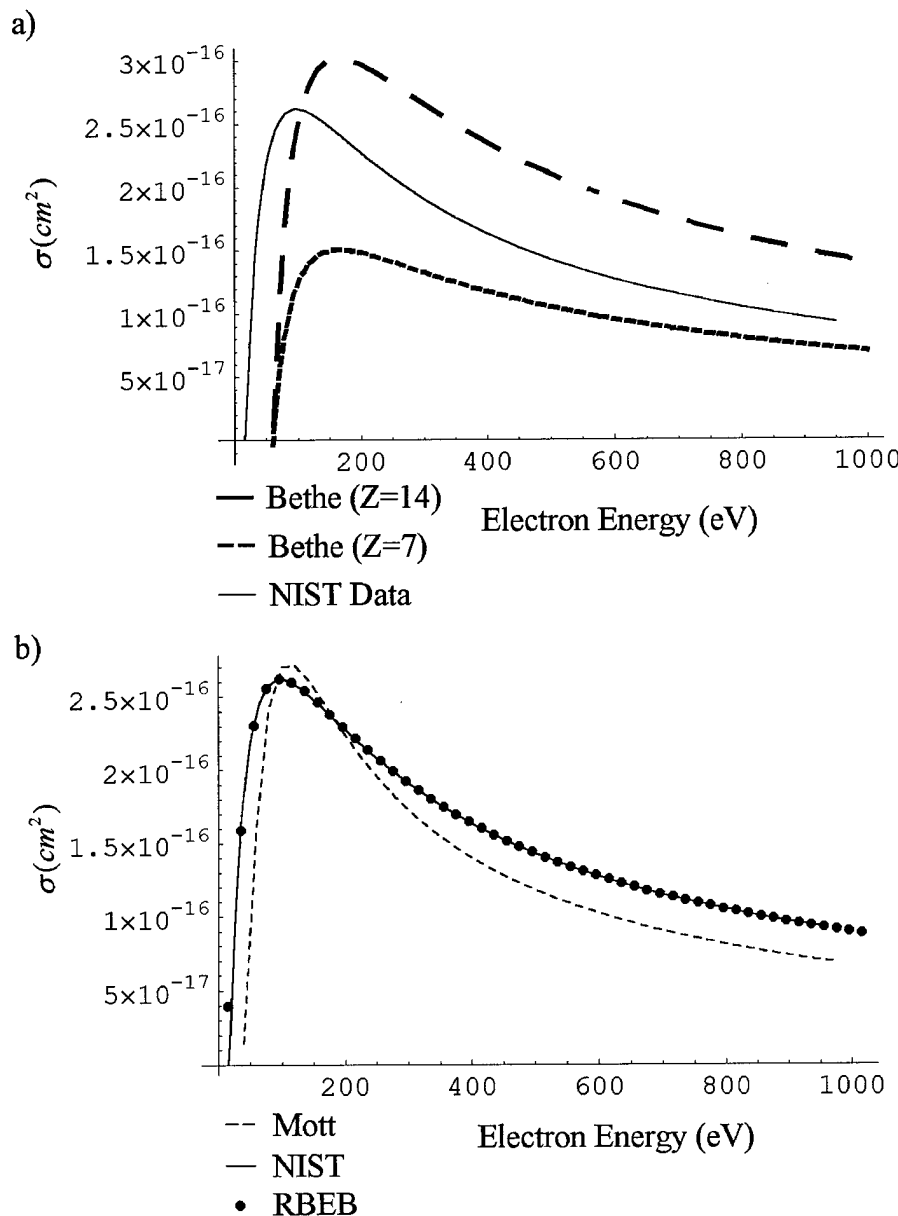


Figure 17. Comparison of Bethe, RBEB, Mott, and NIST Ionization Cross Sections  
a) Comparison of RBEB and Bethe's Total Ionization Cross Sections b)  
Comparison of NIST, Mott's, and RBEB's Total Ionization Cross Sections

RBEB, Mott's and NIST cross sections appear to be in very good agreement at lower energies with a very small difference between their values. Whereas Bethe's cross section marginally agrees with the NIST/RBEB model depending on the value of Z used in the calculation and the energy range over which the cross section is compared. At higher incident electron energies, Bethe's cross section provides a fairly close estimate to the total ionization cross section.

In this chapter, theories on electron elastic and ionization collisions were reviewed. The mathematical collision cross section models resulting from the theories of Mott, Bethe, and Kim were discussed to gain insight into their capabilities and limitations. The resulting cross sections from each model were compared to cross section values that have been established by NIST. The next chapter will show how these cross section models are utilized in a Monte Carlo model that will determine the plasma density distribution created by an electron beam.

#### IV. Electron Beam Propagation

##### Simple Electron Beam Propagation Model (SEBPM)

The primary emphasis of the SEBPM is to develop a lower and upper bound to the longitudinal extent of the plasma generated by an electron beam. The SEBPM is limited to a scenario where the electron travels through the air, but experiences no angular deflection in a collision. Two limiting, energy partitions associated with ionization are considered: the ejected electron is stationary and the incident electron energy is reduced by the ionization energy or the scattered and ejected electrons share the incident electron energy, reduced by the ionization energy, equally. The electrons are then propagated through the air until all the electrons have energies less than the average ionization energy of the air molecules. These ultimate electrons are considered thermal electrons. The limited scenarios described above were addressed to provide a bound on the spatial distribution of the plasma and relate these results to those derived from the more complex Monte Carlo simulation.

##### Axial Density Profile with No Angular Scattering

The scenarios described previously were named 1) Ejected Electrons Receive No Energy (RNE) scenario and 2) Ejected and Scattered Electrons Equally Share Energy (ESE) scenario. In an ionizing collision, the incident electron identifies the electron before the collision, the scattered electron is the incident electron after the collision, and the ejected electron is the electron that is liberated from the target molecule or atom. In the RNE scenario, the incident electron has a relativistic velocity and collides with a bound electron, which results in an ionization event where one of the electrons (either

incident or ejected) leaves the collision volume (defined by the collision parameter b) with the incident energy minus the binding energy of the molecular electron. The ejected electron leaves the collision volume as a thermal electron. It is assumed that all ionization events in the RNE scenario result in only the loss of the average ionization energy from the incident electron. The RNE scenario establishes the maximum longitudinal extent, because the incident electron is neither scattered nor is any energy given to the ejected electron.

The ESE scenario is similar, but it assumes that the ejected and scattered electrons both emerge from the collision volume with an equal amount of energy. This type of ionization event is termed by Evans as a “Hard Collision” and they are infrequent and therefore, contribute very little to the most probable energy loss of an electron. The ESE scenario is the other bound of the possible length of the electron beam generated plasma, because the electrons reduce in energy by half after every collision they do not travel very far through the air.

### Model Theory

The following differential equation describes the decay of a beam of particles due to single collisions experienced by the particles as the beam propagates in the x direction

$$\frac{d\rho}{dx} = -\frac{\rho}{\lambda} \quad (1)$$

The solution to this equation represents an exponential loss in the intensity of the beam over a distance x

$$\rho = \rho_{initial} e^{-\frac{x}{\lambda}} \quad (2)$$

where

$$\rho = \text{number density of the beam of particles (\#/cm}^3\text{)}$$

However, if a single collision does not stop the particle, but rather lowers the energy of the particle, we may use a similar differential equation to describe the loss of the electrons from that energy state.

$$\frac{d\rho_0}{dx} = -\frac{\rho_0}{\lambda_0} \quad (3)$$

where

$\rho_0$  = density of the beam of particles at the initial energy

$\lambda_0$  = mean free path (MFP) of particles at the initial energy of the beam

If we make the assumption that the particle losses the average ionization energy of the gas every time it undergoes an ionizing collision, then we can discretize the energy states such that we have energy states 0, 1, 2 ... n. Where the  $n^{th}$  energy state is defined as the energy of an electron after it has experienced  $n$  ionizing collisions. Therefore, the energy of the  $n^{th}$  energy state,  $E_n$ , is given by

$$E_n = E_0 - n\Delta E$$

where

$E_0$  = initial energy of the electron

$\Delta E$  = average ionization energy of the gas

From this assumption we can write the equations for the change in density of particles in the lower energy states as

$$\frac{d\rho_1}{dx} = \frac{\rho_0}{\lambda_0} - \frac{\rho_1}{\lambda_1} \quad (4)$$

$$\frac{d\rho_2}{dx} = \frac{\rho_1}{\lambda_1} - \frac{\rho_2}{\lambda_2} \quad (5)$$

to

$$\frac{d\rho_n}{dx} = \frac{\rho_{n-1}}{\lambda_{n-1}} - \frac{\rho_n}{\lambda_n} \quad (6)$$

where

$$\lambda_n = \frac{1}{N\sigma(E_n)} \quad (7)$$

$N$  = number density of the air molecules

$\sigma(E_n)$  = ionization cross section as a function of the incident electron energy

Here,  $\sigma(E_n)$  is calculated from the Bethe, Mott, or BEB ionization cross section equation. However, this results in an enormous number of equations for the RNE scenario. As an example, a beam of 1 MeV electrons would result in 27,322 energy states above thermal energy and hence would result in 27,322 differential equations to solve!

Therefore, it was necessary to develop a general analytic solution for the system of first order differential equations (4)-(6). For the RNE scenario the general solution to the system of equations described by equations (4) through (6) is

$$\rho_n = \sum_{k=0}^n \frac{(-1)^n N_e \lambda_k^{n-1} \lambda_n e^{-\frac{x}{\lambda_k}}}{\prod_{\substack{j=0 \\ j \neq k}}^n \lambda_j - \lambda_k} \quad (8)$$

$N_e$  = initial number of electrons in the electron beam

For the ESE scenario, equations (4) to (6) are modified by a factor of  $2^n$  because two electrons of the same energy are created in each collision therefore

$$\frac{d\rho_n}{dx} = \frac{2\rho_{n-1}}{\lambda_{n-1}} - \frac{\rho_n}{\lambda_n} \quad (9)$$

which results in a general solution

$$\rho_n = \sum_{k=0}^n \frac{(-1)^n 2^n N_e \lambda_k^{n-1} \lambda_n e^{-\frac{x}{\lambda_k}}}{\prod_{\substack{j=0 \\ j \neq k}}^n \lambda_j - \lambda_k} \quad (10)$$

For the RNE scenario a stationary, thermal electron is created in every ionization collision, as a result the number of electrons created is determined by summing the electron densities in all  $\rho_n$  states. The result of the summation will yield the over all axial electron density profile of the electron beam. For the ESE scenario, each electron emerged from the collision volume with equal energy, therefore the initial energy of the electron is roughly halved after every collision resulting in a minimal number of electron energy states (for a 1 MeV electron there would be 14 energy states). Therefore, the general solution (10) can be used to calculate the electron number profile for the ESE scenario fairly easily.

However, there is a numerical problem associated with the RNE scenario and the use of equation (8). When  $\lambda_j$  and  $\lambda_k$  are very close in value there is a loss in numerical precision, which increases with each state due to the product term in the denominator of equation (8). This loss in precision eventually leads to completely inaccurate results. Therefore, a numerical method that replicates the physics of equation (8) was developed to estimate the electron number profile of the electron beam.

### Numeric Model Theory

The numeric method for the SEBPM is implemented by treating each energy state as a separate beam of electrons passing through the medium. In the RNE scenario an ionization event results in the same loss of energy each time, therefore the number of electrons in each beam decays exponentially with distance. Equation (2) represents the number of electrons that do not experience a collision in a distance  $x$ . Therefore:

$$\rho = \rho_{initial} (1 - e^{-\frac{x}{\lambda}}) \quad (11)$$

describes the number of electrons that experience a collision in a distance  $x$ . The numeric method or cascading method works by demoting the electrons that underwent a collision to a lower energy state each time a collision occurs. Those electrons that do not undergo a collision stay in the same energy state. This process is repeated until each electron experiences enough ionizing collisions that its energy is less than the average ionization energy of the gas. Figure 18 illustrates how the electrons decay from one energy state to another as the electron beam travels through a distance,  $\Delta x$ . The electrons that decay from a higher energy state provide a source to the electron beam in the next lower energy state (see Figure 18 for a pictorial description of this process). This numeric approximation is very similar to the analytic form, but does not suffer from the loss in numeric precision. The cascading method, however, is very computational intense when the electrons have a large initial energies because of the large number of energy states that must be tracked and the large number of  $\Delta x$  intervals. For the cascading method of SEBPM, the value of  $\Delta x$  must be approximately the same or less than the mean free path of the electrons at that particular energy state. If the  $\Delta x$  value was set much larger than the MFP of the electrons, then all the electrons decayed to the lower energy state in one

$\Delta x$  step. This resulted in an overestimation of the longitudinal extent of the electron profile, because the electrons may have experienced multiple collisions within the large  $\Delta x$  step, but the model only allowed one ionization collision to occur. If  $\Delta x$  was set to small, then the numerical cascade model took a very long time to execute because it had to perform many steps to calculate the longitudinal propagation distance of the electron beam. Therefore, the  $\Delta x$  step had to be reasonably close to the smallest electron MFP value in the simulation to obtain a reasonable estimate of the longitudinal extent of the plasma.

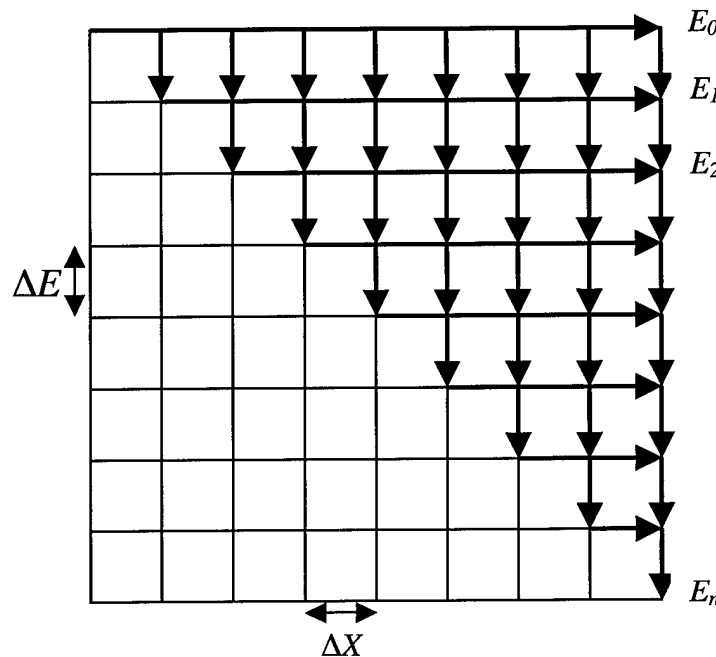


Figure 18. Diagram of Energy States in the SEBPM Numerical Method

#### Results of Simple Electron Beam Propagation Model

For the SEBPM additional simplifying assumptions were introduced to make calculations easier. First, the air is assumed to be 100% molecular nitrogen and second, an average energy of 36.6 eV is assumed to be lost per ionization event (Evans,

1955:698). Bethe's total ionization cross section, Chapter III, equation (20), was used in all calculations with an average ionization energy of 36.6 eV, an I of 86 eV, and a Z of 14.

### Results of the RNE Scenario

In Table 5, the results of the Cascading Method for the RNE scenario at various initial electron energies are shown. The power of the electron beam is fixed at 500 kW and the electron beam is operated for 1 second. Hence, as the initial electron energy increases, the initial number of electrons decreases proportionally. The  $\Delta x$  for the model was set at 0.01 cm which is close in magnitude to the minimum mean free path, at the lowest energy state in the model. Table 5 shows the results of running the model with initial electron energies of 1 MeV, 2 MeV and 5 MeV at a constant power of 500 kW. The relationship between the power of the electron beam, P, and the number of electrons in the electron beam,  $N_e$ , is

$$P = \frac{E}{t} = \frac{E_0 N_e}{t}$$

$$N_e = \frac{Pt}{E_0}$$

where

$E_0$  = energy of the electrons in the electron beam

Table 5. Results of Cascade Model for a RNE Scenario

Electron Energy	Starting # of Electrons	Total # of Electrons after Ionization	Range of Electron Profile
1 MeV	$3.121 \times 10^{18}$	$8.529 \times 10^{22}$	1639 cm
2 MeV	$1.561 \times 10^{18}$	$8.528 \times 10^{22}$	3579 cm
5 MeV	$6.242 \times 10^{17}$	$8.530 \times 10^{22}$	9100 cm

The resulting longitudinal density profile for an electron beam at 1 and 2 MeV is shown in Figure 19. The peak values in the longitudinal density profiles corresponds to the peak value of the ionization cross section for the lower energy electrons (see Figure 17.a).

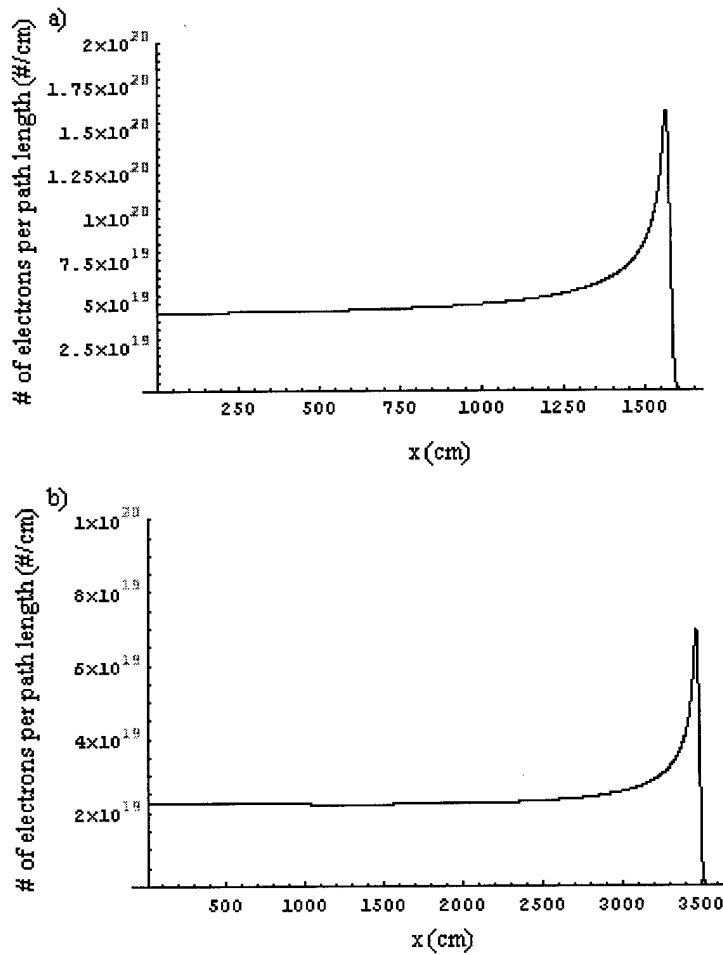


Figure 19. Electron Longitudinal Density Profile from the RNE Scenario for an Electron Beam of a) 1 MeV b) 2 MeV

#### Results of the ESE Scenario

The following table shows the results from equation (10) at various initial electron energies. The power of the electron beam is fixed at 500 kW and the pulse length of electron beam is 1 second. For this scenario  $\Delta x$  is set at 0.01 cm, which is close to the

magnitude of the mean free path of the lowest energy state. An assumption was made that the ionization cross section for ESE scenario was the same as the RNE scenario for an equivalent energy of the incident electron. This assumption is not true, but it did present the extreme limiting case for the distance that the electron beam would travel. The final electron distribution is not found the same way as in the RNE scenario, because the ejected electrons have the same energy as the scattered electrons. Therefore, the electron distribution profile is the electron number of the  $n^{\text{th}}$  or last energy state. From equation (6), we obtain the relationship between the  $\rho_n$  and  $\rho_{n-1}$  which is

$$\rho_n = \int_0^x \frac{\rho(x')}{\lambda_{n-1}} dx' \quad (12)$$

The term  $\lambda_{n-1}$  has a large range of possible values depending on the final energy state in the calculation. This is due to the cross section peaking as the incident electron energy nears the binding energy of the molecule or atom. After peaking the ionization cross section decreases rapidly in value (see Figure 17). The value of  $\rho_n$  is very dependent on the value of  $\lambda_{n-1}$ , and since  $\lambda_{n-1}$  has such a large range of possibilities; we must insure that we obtain a reasonable value for  $\lambda_{n-1}$ . Therefore, two methods were implemented of determining  $\lambda_{n-1}$  for the ESE scenario. In the first method, the mean free paths of the last five energy states ( $\lambda_{n-1}, \lambda_{n-2}, \lambda_{n-3} \dots$ ) are averaged over an energy bin. Since, the difference in energy between the  $E_{n-1}$ ,  $E_{n-2}$ , and  $E_{n-3}$ , corresponding to  $\lambda_{n-1}, \lambda_{n-2}, \lambda_{n-3}$  for the ESE case is not constant, therefore the energy bin is defined as the energy half way between the next highest and lowest energy states.

$$\Delta E_{n-1} = \frac{(E_n - E_{n-1})}{2} + \frac{(E_{n-1} - E_{n-2})}{2} \quad (13)$$

For the second method, no averaging is done for the  $\lambda_{n-1}$ . The results of the electron distribution for both methods and the length of the electron beam profile are given in Table 6 and the resulting electron number density profiles are shown in Figures 20, 21, and 22.

Table 6. Results of ESE Scenario for Initial Energies of 1 MeV, 2 MeV, and 5 MeV

Electron Energy	Starting # of Electrons	# Electrons Ionized with $\lambda$ averaged	Electrons Ionized with $\lambda$ not averaged	Range of Electron Profile
1 MeV	$3.121 \times 10^{18}$	$5.111 \times 10^{22}$	$6.184 \times 10^{22}$	0.7 cm
2 MeV	$1.561 \times 10^{18}$	$5.1136 \times 10^{22}$	$6.187 \times 10^{22}$	0.8 cm
5 MeV	$6.242 \times 10^{17}$	$4.0909 \times 10^{22}$	$4.267 \times 10^{22}$	1.2 cm

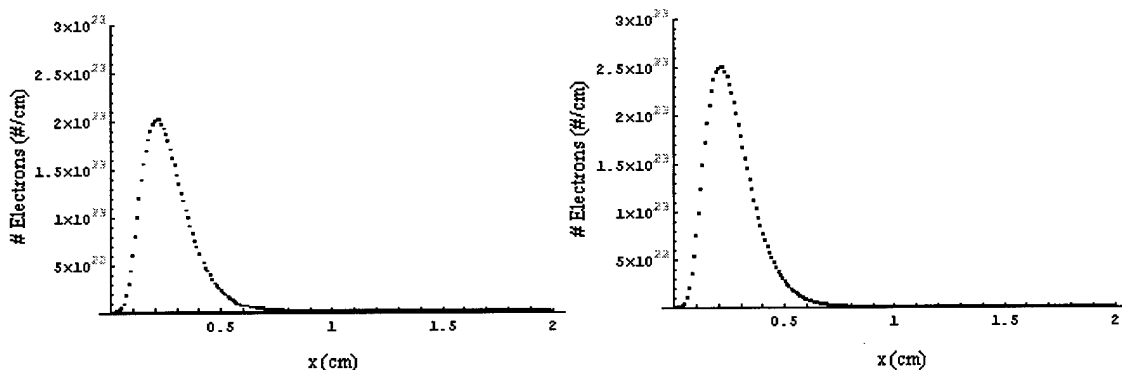


Figure 20. Axial Profile of 1 MeV Electrons in ESE scenario  
 (a) Averaged MFP (b) Non-Averaged MFP

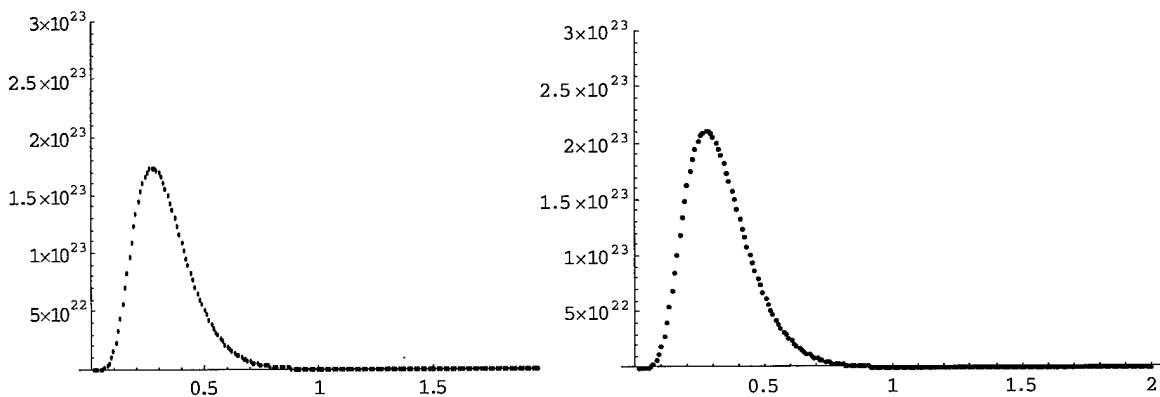


Figure 21. Axial Profile of 2 MeV Electrons in ESE scenario  
 (a) Averaged MFP (b) Non-Averaged MFP

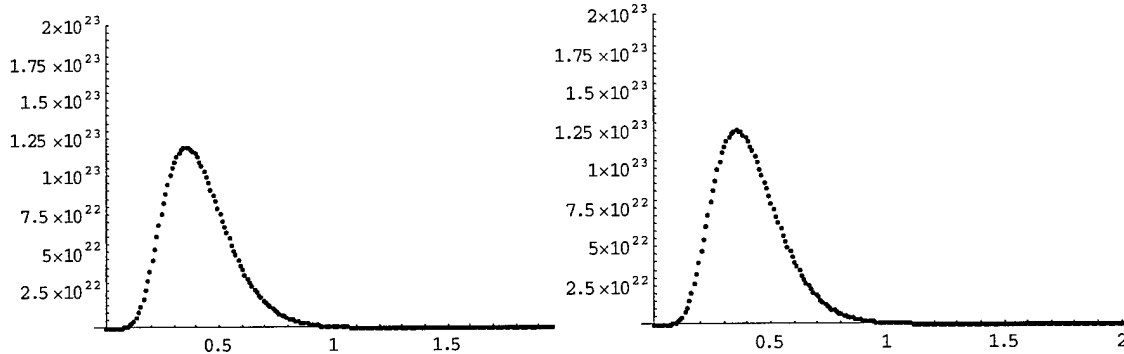


Figure 22. Axial Profile of 5 MeV Electrons in ESE scenario  
 (a) Averaged MFP (b) Non-Averaged MFP

Determining if the electrons conserve energy provides a simple check to the validity of the models. The total ending energy is calculated by multiplying the total number of electrons made by the average ionization energy for the RNE scenario. Comparing the total ending energy with the total starting energy of the electron beam we obtain Table 7.

Table 7. Test for Energy Conservation for the RNE scenario

Electron Energy	Total Starting Energy (J)	Total Ending Energy (J)
1 MeV	$5 \times 10^5$ J	500,086 J
2 MeV	$5 \times 10^5$ J	500,040 J
5 MeV	$5 \times 10^5$ J	500,134 J

Table 7 indicates that the model conserves energy almost perfectly. For the ESE scenario the total ending energy is calculated by multiplying the total number of electrons made by the energy in the last energy state. Comparing the total ending energy with the total starting energy of the electron beam we obtain Table 8, which indicates that the ESE model conserves energy almost perfectly as well.

Table 8. Test for Energy Conservation for the ESE scenario

Electron Energy	Total Starting Energy (J)	Last Energy State	Total Ending Energy (J)
1 MeV	$5 \times 10^5$ J	61 eV	$4.99 \times 10^5$ J
2 MeV	$5 \times 10^5$ J	61 eV	$4.99 \times 10^5$ J
5 MeV	$5 \times 10^5$ J	76 eV	$4.98 \times 10^5$ J

The SEBPM bounded the electron beam longitudinal extent for various initial electron energies (See Table 9.). Because the power attenuation of the wave is equal to  $e^{-2k_i r}$ , we need the plasma to have both large spatial extent and density (because  $k_i$  increases with plasma density, Chapter II, equation (4)). The maximum electron beam longitudinal extent is approximately proportional to the initial electron energies of the electron beam, if we assume that the transverse extent of the plasma stays the same with increasing electron energy, then the density of the plasma will reduce linearly with increasing electron energy. If we assume that the transverse extent of the electron beam will also increase linearly with the initial electron energy (which is shown to be the case in Chapter V), then the decrease in plasma density will be proportional to  $1/T^3$ , where  $T$  is the initial energy of the electrons in the electron beam. Therefore, the initial electron energies of the electron beam will most likely be at 1 MeV or below.

Table 9. SEBPM Minimum and Maximum Beam Length Results

Electron Energy	Min Electron Beam Penetration	Max Electron Beam Penetration	Total Power
1 MeV	0.7 cm	1639 cm	500 kW
2 MeV	0.8 cm	3579 cm	500 kW
5 MeV	1.2 cm	9100 cm	500 kW

The SEBPM has bounded the length and the number density of the plasma, but we still have no estimate on the transverse extent of the electron beam due to electron scattering. To obtain an estimate of the width and distribution of the electron beam generated plasma, a Monte Carlo method will be used. The Monte Carlo method described in the next section of this chapter should give a more accurate result as to the length, width, and density distribution of the plasma created by the electron beam.

### Monte Carlo Method

The purpose of this section is to describe the Monte Carlo method and show how it can be utilized to develop a more detailed model than was used in the previous section. The last subsections of this section are devoted to describing the program that was developed to simulate the electron beam propagating through the air using the Monte Carlo method.

The Monte Carlo Method models random processes such as particle diffusion and transport by tracing the histories of sample particles as they travel through the medium. All collision events between particles are assigned a probability of occurring and a pseudo-random number is picked to determine which event took place. The results of the randomly selected collision events result in a unique trajectory for each particle. After calculating the histories of many particles, we can treat the results of the simulation as a statistical sample of how all the particles in a system may behave. Therefore, a correlation must be established between statistical and physical results of the Monte Carlo Simulation.

### Monte Carlo Techniques

The purpose of this section is to provide a brief overview of the basics of the Monte Carlo method. For a more detailed discussion of the Monte Carlo Method the reader should consult the Computational Methods of Neutron Transport (Lewis 1984:296-356). In the case of the relativistic electron beam traversing the air, the focus will be exclusively on the interactions between electrons and air molecules. In Chapter III, several relationships between the energy of an electron and its collision cross section with a molecule were developed. If we were to introduce an electron with mass  $m_e$ , velocity  $v_e$ , charge  $e$  into a gas of molecules of number density  $N_m$  with velocity  $\ll v_e$ , in which the collision cross section of the electron with the molecules is  $\sigma$ , we could describe the frequency of the electron's collisions with the air molecules by the relationship

$$v = N_m \sigma |v_e| \quad (13)$$

If we consider many electrons in the gas following the same path, we can describe the rate at which the electrons experience a collision by the differential equation

$$\frac{d\rho}{dt} = -\rho v \quad (14)$$

which results in a solution that represents the number of electrons that experience a collision

$$\rho = \rho_0 \exp[-\int v dt] \quad (15)$$

where

$\rho$  = density or intensity of the electrons in the beam ( $e^-/cm^3$  or  $g/cm^3$ )

The collision frequency is constant with respect to  $t$  since there are no forces acting on the electrons, therefore

$$\rho = \rho_0 \exp[-\nu t] \quad (16)$$

The exponential term represents the probability density function,  $f(t)$ , that the electron will experience a collision between time,  $t$  and  $t + dt$ . The cumulative probability distribution function is defined by

$$F(t) = P\{t' \leq t\} \quad (17)$$

and is the probability that the random variable,  $t'$ , is less than or equal to  $t$ . The relationship between the probability density function and the cumulative probability distribution,  $F(t)$ , is

$$f(t) = \frac{dF(t)}{dt} \quad (18)$$

Therefore, the number of electrons that collide in the time interval  $0 \leq t \leq T$  can be represented by the equation

$$\rho = \rho_0 F(T) = \rho_0 (1 - P) = \rho_0 (1 - \exp[-\nu t]) \quad (19)$$

Using equation (18), we can also introduce the rules for transformation of random variables. We begin by letting

$$x = x(t) \quad (20)$$

where  $t$  is a random variable. If  $g(x)dx$  is the probability that  $x$  is between  $x$  and  $x + dx$ , and  $f(t)dt$  is the probability that  $t$  is between  $t$  and  $dt$  and if these probabilities are equal then we can write the relationship

$$|g(x)dx| = |f(t)dt| \quad (21)$$

Since the probability distribution functions must be positive, we obtain the expression

$$g(x) = f(t) \left| \frac{dt}{dx} \right| \quad (22)$$

If we consider  $x$  being the particular function,  $x = F(t)$  of the random variable  $t$ , where  $F(t)$  is the cumulative probability distribution. As a result equation (22) becomes

$$g(F(t)) = f(t) \left| \frac{dt}{dF(t)} \right| \quad (23)$$

Using equation (18) to determine the derivative in equation (23), we obtain for the transformation,  $x = F(t)$ , the equation

$$g(F(t)) = 1 \quad (24)$$

where

$$g(F(t))dF(t) = dF(t) \quad (25)$$

$$0 \leq F(t) \leq 1 \quad (26)$$

Thus the probability of the random variable,  $F(t)$ , taking on a value between  $F$  and  $F + dF$  is equal to  $dF$ . This shows that  $F$  is uniformly distributed between zero and one.

A Pseudo-Random Number (PRN) from a computer is also evenly distributed between 0 and 1 and is unbiased. By setting the cumulative probability distribution equal to the PRN generated by a computer

$$F(T) = \zeta \quad (27)$$

where  $\zeta$  is a random variant from a PRN generator, we are able to obtain an unbiased distribution of the  $F(T)$  values from the computer's PRN generator. However, we are interested in the distribution of  $t$  values, therefore we must invert the cumulative distribution function:

$$t = F^{-1}(\zeta) \quad (28)$$

For the simple case of no external forces on the electron this is not complicated, but for cases when there is an external force on the electron this process maybe difficult. The associated cumulative distribution function for the probability density function described by equation (16) is

$$F(t) = \zeta = 1 - \exp[-vt_i] \quad (29)$$

The result of the inversion for equation (29) is

$$t_i = -\frac{1}{v} \ln(1 - \zeta) \quad (30)$$

From equation (30), we obtain a distribution of the time between collisions for the electrons. With the time distribution and the electron's energy, the history of the electron can be followed. In two dimensions, the trajectory of the electron between collisions will be simply

$$x = |v_e| t \cos \theta \quad (31)$$

$$y = |v_e| t \sin \theta \quad (32)$$

where  $\theta$  will change after each collision. If we start with a simplifying assumption that after a collision all electrons are scattered isotropically, then we will have all the equations we need to write a simple Monte Carlo simulation (Lewis, 1990:299-303).

If a joint probability density function is separable such that

$$f(x, y) = f_1(x)f_2(y) \quad (33)$$

then  $x$  and  $y$  are said to be independent. For an isotropic angular distribution, the joint angular probability density function is separable as well.

$$f(\theta, \phi) \frac{\sin \theta d\theta d\phi}{4\pi} = C \frac{\sin \theta d\theta d\phi}{4\pi} \quad (34)$$

where  $C$  is a constant. Since

$$\int \frac{\sin \theta d\theta d\phi}{4\pi} = 1 \quad (35)$$

then the following equation is true

$$f(\theta, \phi) = C = 1 \quad (36)$$

then

$$\frac{\sin \theta d\theta d\phi}{4\pi} = \left( \frac{dA}{2} \right) \left( \frac{dB}{2\pi} \right) \quad (37)$$

where  $A = \cos \theta$  and  $B = \phi$ . Hence, the cumulative distribution simply becomes

$$F(A, B) = F(A)F(B) = \left( \frac{1-A}{2} \right) \left( \frac{B}{2\pi} \right) \quad (38)$$

And an isotropic scattering angle is determined from the equations using the random variates

$$F(A) = \zeta_1$$

$$F(B) = \zeta_2$$

which results in the  $i^{\text{th}}$  scattering angle being

$$\theta_i = \cos^{-1}(2\zeta_1 - 1) \quad (39)$$

$$\phi_i = 2\pi\zeta_2 \quad (40)$$

Using this angular distribution, we can then follow the electron as it travels through the air. For the two-dimensional case these equations will enable us to trace the electron between collisions using the following equations

$$x_i = x_{i-1} + |v_e| t_i \cos \theta_{i-1} \quad (41)$$

$$y_i = y_{i-1} + |v_e| t_i \sin \theta_{i-1} \quad (42)$$

where

$x_i, y_i$  = the position of the electron at the  $i^{\text{th}}$  collision

$t_i$  = time between the  $i$  and  $i - 1$  Collisions

and  $\theta_{i-1}$  = the scattering angle in laboratory frame after the  $i - 1$  collision

(Ramos, 1990:46-47). For the case of a relativistic electron scattering after an ionization or elastic collision, an isotropic approximation to the scattering angle distribution is not valid. Therefore, the scattering angle distribution developed by Mott, Chapter III, equation (30), should be used for the Monte Carlo simulation.

When there are multiple types of collisions being modeled by the Monte Carlo simulation the cross section can be interpreted as the probability of having a collision of a given type. The total cross section,  $\sigma_{\text{total}}$ , is equal to the sum of all possible collision cross sections.

$$\sigma_{\text{total}} = \sum_i \sigma_i \quad (43)$$

where

$\sigma_i$  = cross section for a collision of type  $i$

Because the collisions are mutually exclusive events, the probability that a particular type of collision will occur is

$$P_i = \frac{\sigma_i}{\sigma_{\text{total}}} \quad (44)$$

If we select a random number,  $\zeta$ , that is uniformly distributed between zero and one, we can determine which type of collision occurs. Hence, we can determine if an electron incident on a molecule experiences an elastic or ionization collision with either an oxygen or nitrogen molecule based on their cross sections and relative concentrations.

For further discussions on the Monte Carlo Method the reader should consult Computational Methods of Neutron Transport (Lewis, 1984:296-303).

Using the equations presented in this section and the theoretical cross sections developed in Chapter III, we can develop a computer program that tracks the trajectory of the electron until it no longer has enough energy to ionize another molecule. We also note that each ionization event results in another electron whose trajectory must be tracked as well. The coordinates of the thermalized electrons, electrons that have energy less than the minimum ionization energy, are recorded. The thermalized electrons coordinates are then used to determine the density distribution of the plasma using descriptive statistics, which are presented in the next section.

### Descriptive Statistics

Because there will be a large number of ionization events per high energy electron, even if we start the Monte Carlo simulation with a modest number of initial electrons we could end up with millions of ejected electrons. If a 1 Mev electron loses all its energy in ionization collisions, the electron will have liberated 27,322 molecular electrons (given an average energy loss of 36.6 eV per ionization). If we start the Monte Carlo simulation with 1000 electrons then we will end up with over 27 million electrons. Tracking and performing statistics on several million individual electrons requires an exceptional amount of computer resources. Therefore, thermalized electron coordinates were binned in a two-dimensional grid and group statistics were used to determine the distribution characteristics -of the plasma. Group statistics are used when the data has been put into bins and individual data points are not known. The following equation gives the sample mean,  $\bar{x}$ , of a distribution of binned data

$$\bar{x} \approx \frac{\sum_{i=1}^k f_i M_i}{n} \quad (45)$$

where

$k$  = number of bins in the frequency distribution

$M_i$  = midpoint of the  $i^{\text{th}}$  bin

$f_i$  = frequency of the  $i^{\text{th}}$  bin

$n$  = total sample size

and the sample variance is estimated by the equation

$$s^2 \approx \frac{\sum_{i=1}^k f_i (M_i - \bar{x})^2}{n-1} \quad (46)$$

(Kiemele, 1997:75-76). The Monte Carlo simulation estimates the mean and standard deviation of the electron distribution, transverse to the axis of the beam, using these equations.

#### Electron Beam Simulation (EBS) (Monte Carlo) Description

The EBS uses a Monte Carlo methodology to determine the electron distribution resulting from a relativistic beam of electrons propagating through the atmosphere. The simulation was written in Fortran 90 using Digital Visual Fortran Professional Edition 5.0A and Microsoft Developer Studio 97. It uses NAMELIST I/O for input from the user and produces ASCII text files that describe the distribution of the plasma. From the input files the user can turn on or off certain types of collisions, customize the output of the program, change the energy, power, and other electron beam characteristics, change

altitude and velocity, and much more. Output files provide descriptive statistics of the electron distribution as well as a two dimensional map of the electron distribution.

### Design Philosophy

The core of the EBS program is the Monte Carlo method. EBS follows the trajectory of one electron at a time as it propagates through the air. Total cross sections from the theoretical models in Chapter III, are used to determine if the electron experiences an elastic or ionization collision. If an ionization collision occurs then a new electron is created with a certain energy and direction depending on the probability distribution function. As a result of the ionization collision, the incident electron is deflected and losses energy from the collision. If an elastic collision occurs then the electron is deflected according to the probability distribution function given by Chapter III, equation (12). The process of the electron colliding with a neutral molecule, scattering, losing energy, and moving to the next collision is repeated until the initial electron's energy is less than the minimum ionization energy of oxygen (which is 12.3 eV) at which time the coordinates of the end electron are recorded and a new electron is introduced into the scenario. The electron termination coordinates and energies are then processed and reported to the user via descriptive statistics. For a flow diagram of the EBS program see Figure 23 and 24.

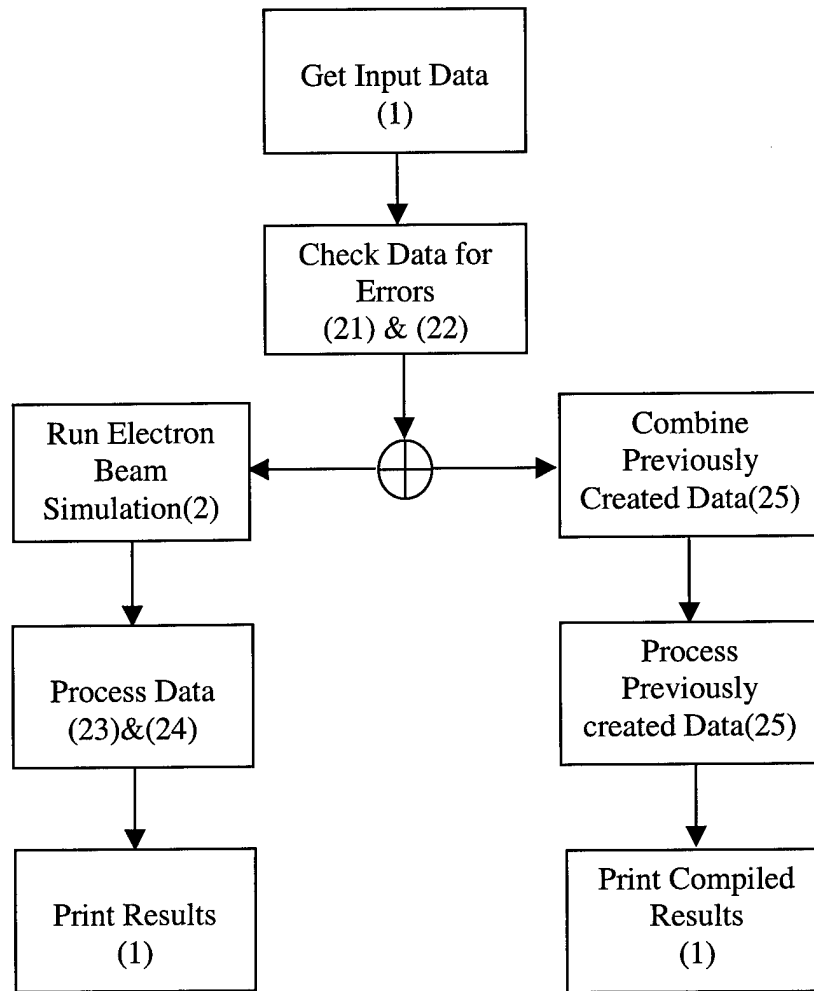


Figure 23. Flow Diagram of Main Program.  
 Numbers represent the subroutines found in  
 Table 12 that perform the task in the block

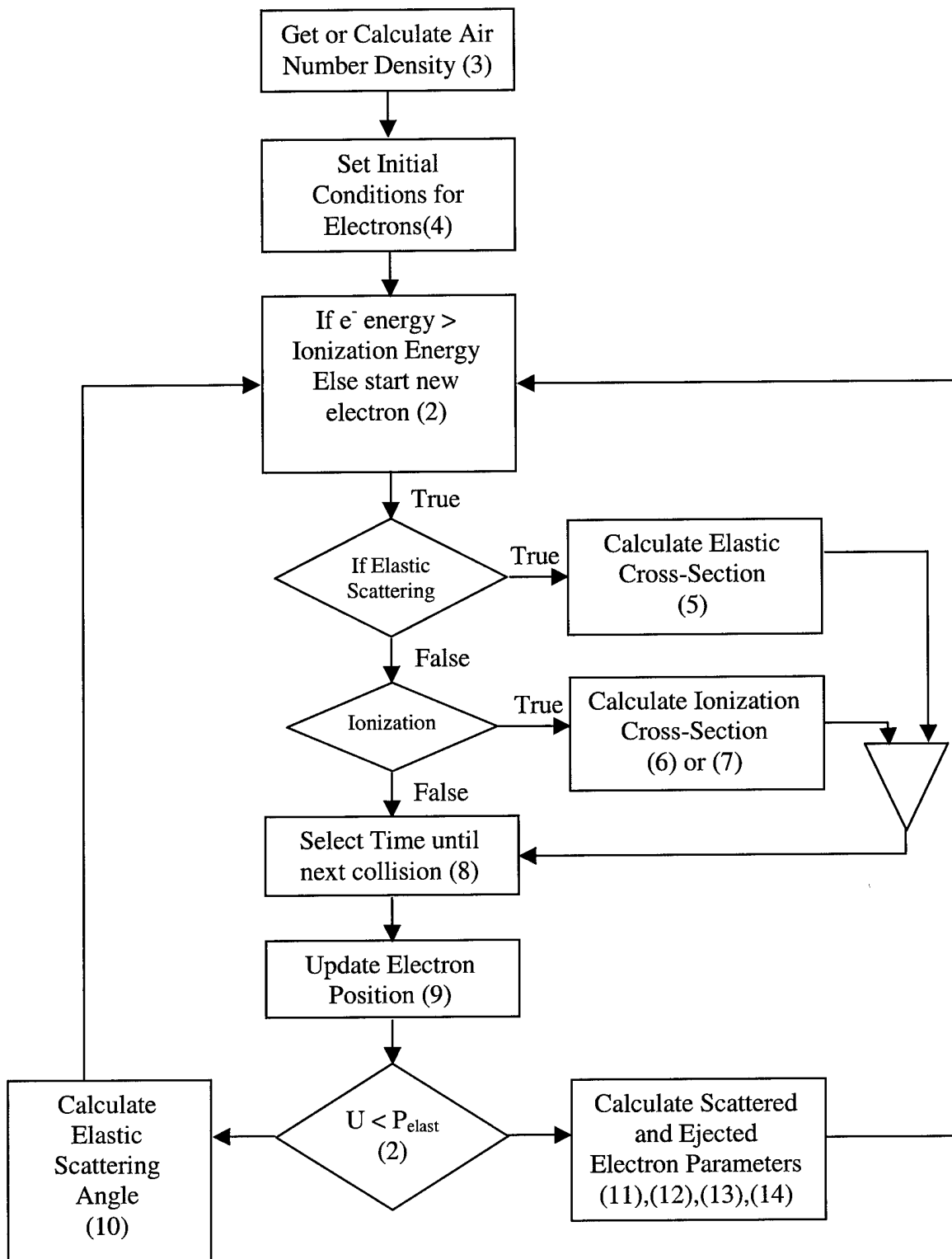


Figure 24. Flow Diagram of SimControl.  
Numbers Represent the Subroutines Found in  
Table 12 that Perform the Task in the Block

## Inputs

EBS is a data driven simulation with three main data files that are used to supply input to the simulation. These files are formatted for use with the Fortran 90 NAMELIST I/O function (see Appendix B). The main data file is the Ebeam.inp file, which is modified by the user to provide parameters for the simulation. The second data file is the Default.dat file, which provides the default parameters for the simulation if none are specified in the Ebeam.inp file. The third data file contains data on the molecules in the simulation. Other input files contain the ejected electron momentum transfer probability distribution that is used by the simulation to determine how much momentum and energy is transferred from an incident electron to the ejected or ionized electron.

The execution of the Electron Beam Simulation is accomplished by first modifying the parameters of the EBeam.inp file and then executing the EbeamScattering.exe file. See Appendix B, Table 13 for a listing of all the input variables to the EBS program and their function. Due to the flexibility of the NAMELIST I/O format, data does not have to be entered in a specific order. If a number of different simulations are going to be run, the user can modify the default values in the default\_file.dat to reduce the number of parameters that need to be supplied in the EBeam.inp file. The Molecule\_Data\_File.dat can be modified to incorporate additional gas species into the EBS program. The data required to add a molecule to the simulation includes binding energies of the electrons, orbital energies of the electrons, and shell occupation number. Experimental as well as calculated data on the binding and orbital energies of electrons in various light molecules and atoms can be found on the NIST web site (Kim, 2000).

## Outputs

There are two main output files for the EBS simulation. The output files include the descriptive statistics file, named by the user, which provides a summary of all the input parameters, the axial beam profile, the sample mean of the transverse electron distribution, and the standard deviation of the transverse electron distribution. The second file produced, \*.PROCESSED, contains a two dimensional map of the frequency distribution of the coordinates of the end electrons. Figure 25 provides a diagram of the coordinate system and the two dimensional map in which the end electron frequency data is stored. The size and number of cells is determined by the user and should be based on the initial energy of the electron such that it provides adequate resolution for the electron distribution. Additional files contain a compilation of the data from many simulation runs and are created if the appropriate options are selected. This was done because many of the simulations that were executed required too much computer resources; therefore large simulations were divided into smaller simulations. The results of the smaller simulations are combined into the \*.COMPILED and \*.RES. The form of the data from these files is the same as the main output file and the \*.PROCESSED file.

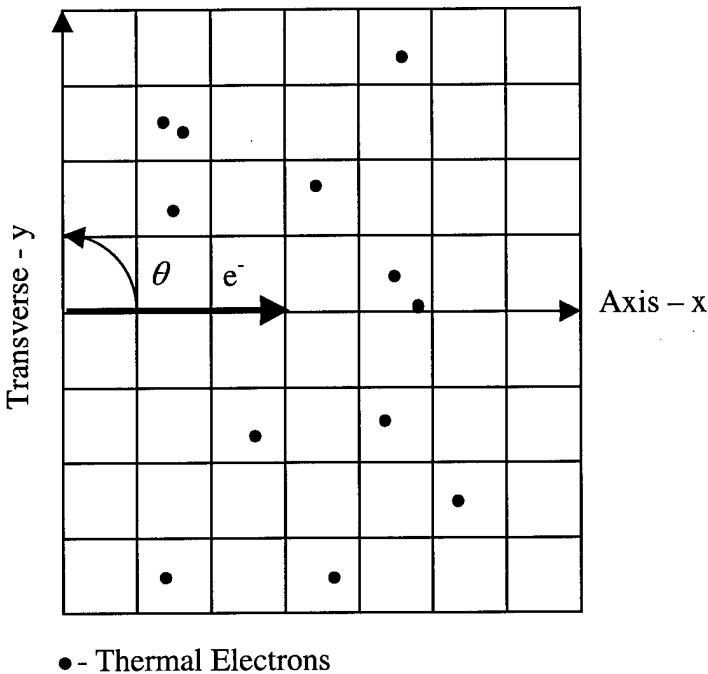


Figure 25. EBS Setup, Electron Beam Propagation Direction, and Coordinate System

#### Description of Functions and Subroutines

In Table 10, there is a brief synopsis of the functions and subroutines found in the EBS program. The first column provides the number that is referenced in Figures 23 and 24. The second column provides the name of the subroutine or function. The third column indicates the main output of the function or subroutine and provides a brief description. A more detailed documentation on the EBS program is provided in the code itself.

Table 10. Description of Subroutines for the EBS Program

Sub #	Subroutine Name	Brief Description
1	ebeamprog	<p><b>Main Program</b></p> <p>The ebeamprog performs four major functions. First it reads the NAMELIST input files supplied by the user. It then checks the input data for errors and starts the Monte Carlo simulation by calling the simcontrol function if there are no errors. When the simcontrol function completes, ebeamprog outputs the results of the simulation to a file. Ebeamprog also calls the functions that compile the results of multiple simulations with the appropriate input.</p>
	EBeamSimControl	Module
2	SimControl	<p><b>Monte Carlo Simulation</b></p> <p>The controlling function for the Monte Carlo simulation. It calls all the functions responsible for setting the initial energy and position of the electrons, calculating collision cross sections, calculating the electron trajectory, determining the number of ionized electrons and processing the results of the simulation.</p>
	EBeamFuncModule	Module
3	AirDensity	<p><b>Calculate <math>N_m</math></b></p> <p>Calculates the density of the air at the altitude given by the user. AirDensity assumes the atmosphere is exponential and uses a scale height of 8180 m (Al'pert, 1960:84)</p>
4	CreateEData	<p><b>Set electron initial conditions</b></p> <p>Assigns initial energies and positions to electrons. If the logical variable InitDist is FALSE then the electrons are all given the same energy and initial angle. If the InitDist is TRUE then the electrons are given a Gaussian energy distribution and initial angle distribution.</p>
5	GetElasticCrossSect	<p><b>Calculate <math>\sigma_{elastic}</math></b></p> <p>Uses Chapter III, equation (12) to determine the total elastic cross section of the electron colliding with either nitrogen or oxygen molecules.</p>

6	GetIonCrossSect	<u>Calculate <math>\sigma_{ion}</math></u> Uses the relativistic Bethe equation, Chapter III, equation (20), to determine the total ionization cross section of an air molecule based on the user supplied average ionization energy.
7	GetBEBCrossSect	<u>Calculate <math>\sigma_{ion}</math></u> Calls the BEBModel function and passes it the appropriate electron orbital data to calculate the ionization cross section of the orbital shells of an atom or molecule. The orbital shell cross sections are then put into an array and passed to simcontrol.
8	SelectTime	<u>Calculates time between collisions</u> Uses equation (30) to calculate the time between collisions for the electron.
9	EMotion	<u>Calculate <math>e^-</math> trajectory</u> Calculates the trajectory of the electron after it undergoes a collision using the electron scattering angle and the time between collisions calculation.
10	ElasticScatteringAngle	<u>Calculates elastic scattering angle</u> Determines the angle at which the electron is scattered after experiencing an elastic collision. This is done by calling the function IntegratedElasticCrossSect, which uses the integrated form of the Mott elastic cross section to determine the cross section of an electron being scattered into a particular angular range. Sixty increments from thetamin to pi (thetamin is determined by Chapter III, equation (13)) are added up and divided by the total elastic scattering cross section to determine the probability of the electron being scattered in that angular range. Once the angular range is determined the actual angle of scattering is determined by linearly interpolating between the two end values of the range of angles.
11	EjectedElectronEnergy	<u>Calculate W</u> Determines the electron ejection energy by using a previously calculated electron ejection energy probability distribution table. The probability distribution table was calculated by integrating Chapter III, equation (30) over all ejection angles and ejection energies. The results of the integration were stored in several files that are imported into EBS upon execution of the program.

12	EVelosity	<u>Calculate <math>v_e</math></u> Determines the relativistic electron velocity based on the electron energy
13	IonScatteringAngle	<u>Calculate <math>e^-</math> scattering angle</u> Determines the angle at which the electron is scattered after experiencing an ionization collision. This is done by numerically integrating the function EjectionEquation, which contains Chapter III, equation (30), to determine the cross section of an electron being scattered into a particular angular range. Sixty increments from 0 to thetamax (thetamax is set such that the probability of the electron being scattered at an angle larger than thetamax is $10^{-7}$ ) are added up and divided by the total scattering cross section to determine the probability of the electron being scattered in a particular angular range. Once the angular range is determined the actual angle of scattering is determined by linearly interpolating between the two end values of the range of angles.
14	EjectedElectronAngle	<u>Calculate <math>e^-</math> scattering angle</u> Same as IonScatteringAngle, except the MottEquation function is used which contains Chapter III, equation (23).
15	AngleCleanUp	<u>Keeps angles between 180 and -180 degrees</u> Alters the scattering angle of the electron if it is greater than 180 degrees or less than -180 degrees such that it is in the appropriate quadrant and has a value of 180 to -180 degrees.
16	MaxE	<u>Determines maximum number <math>e^-</math> simulated</u> Determines the maximum number of electrons that will be modeled by the Monte Carlo simulation by dividing initial electron energy by the minimum ionization energy
	FunctionModule	Module
17	ScatteringAngleDist	<u>Equation</u> Contains Chapter III, equation (12) which describes the elastic scattering angle distribution of an electron after colliding with a nucleus
18	IntegratedElastic CrossSect	<u>Equation</u> Contains Chapter III, equation (14) which describes the elastic scattering angle distribution of an electron after colliding with a nucleus

19	EjectionEquation	<u>Equation</u> Contains Chapter III, equation (23) which is Mott's ionization TDCS
20	MottEquation	<u>Equation</u> contains Chapter III, equation (36) which is Mott's ionization DDCS
21	BEBModel	<u>Equation</u> Contains Chapter III, equation (48) which is the RBEB total ionization cross section
	IntegrationModule	Module
22	Integrate	<u>Integrates equations</u> Integrates functions using, Simpson's, Trapezoid, or Gaussian Quadrature method.
	EBeamInput	Module
23	GetCrossSectData	<u>Imports cross section data</u> Imports normalized ejection energy probability distribution data
24	CheckData1	<u>Checks data for errors</u> Checks data for errors and sets error flag if error in input data is found
25	CheckData2	<u>Create error message</u> Generates appropriate error message if error in input data is found
	EBeamOutput	Module
26	ProcessOutput2	<u>Process Monte Carlo results</u> Takes the analog electron distribution calculated by the Monte Carlo simulation and places it in a two dimensional grid of the electron beam based on the end x and y coordinates of the electrons. ProcessOutput2 then determines the axial profile, the mean transverse electron position, and the transverse electron distribution.
27	ProcessCompiledOutput	<u>Process Monte Carlo results</u> Same as ProcessOutput2 except used to compile results from multiple simulations
28	ReCompileOutput	<u>Process Results</u> Combines archived data

A validation of the Electron Beam Scattering (EBS) simulation was performed to insure that the Monte Carlo method was implemented correctly in the EBS program. The EBS simulation was compared with the results of the SEBPM. For the purposes of this comparison the electrons in the EBS simulation were limited to the same restrictions

applied to the RNE scenario of the SEBPM model; that is the electrons did not experience any angular scattering and the ejected electrons received no energy. In Figure 26, a comparison between the electron distribution profile of the SEBPM and EBS programs is shown. The results of the simulations showed excellent correlation indicating that the cross section, time, and trajectory calculations in the Monte Carlo simulation had been implemented correctly. The results also indicated that the SEBPM calculations were indeed the bounding conditions for the electron beam longitudinal extent and electron number profile.

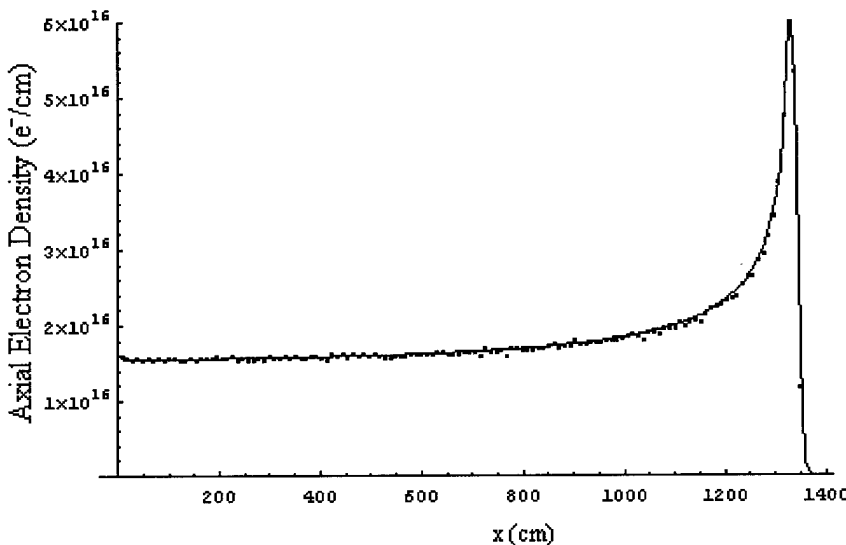


Figure 26. Comparison between the SEBPM and EBS Simulations Axial Electron Density Profile for the RNE scenario

The EBS program can provide a relatively accurate estimate of the plasma density distribution and the dimensions of the electron beam generated plasma. By importing the results of the EBS program in to the EMWPM program, we can obtain power attenuation due to a plasma that has achieved a steady state in density. However, the EBS simulation completely excludes any volumetric loss mechanisms introduced by reactions between the electrons, ions, and neutral molecules present in the plasma. The next section

provides an estimate as to the plasma density variations due to attachment, detachment, and recombination processes.

### Plasma Density Loss Mechanisms

Now that we have the means to calculate the source term for the electrons being injected into the plasma, we must consider the plasma chemistry that results from having a highly reactive ion and electron mix. The following section describes the major loss and gain mechanisms in a nitrogen-oxygen plasma and the resulting temporal evolution in the concentration of the electrons, ions, and neutral atoms. The chemical rate coefficients associated with the relevant kinetic mechanisms are assembled into a set of differential equations that describe the rate of change in the density of the constituents of the plasma. From these differential equations, we obtain an estimate of the variation in the density of the plasma as a function of time. For simplification a large number of insignificant reaction processes were excluded from the model. Also atoms or molecules in an excited state after a reaction were assumed to de-excite and join the ground state population of atoms or molecules immediately.

As the electrons decrease in energy, collisions other than ionization and elastic scattering become relevant to our calculation of the plasma density. For electrons the loss and gain mechanisms other than ionization are attachment, recombination, and detachment. Attachment occurs when a free electron becomes bound to a neutral atom or molecule, forming a negative ion. The following equation describes an electron attaching to an oxygen molecule in a two-body attachment process.



At higher pressures of  $O_2$ , another attachment process, a three-body attachment process, may dominate:



Recombination describes the process of an electron colliding with a positive ion and forming a neutral atom or molecule



Detachment describes the process of an electron, atom or molecule colliding with a negative ion and stripping the attached electron.



The dominant loss mechanisms for the plasma based on their large rate constants and the density of the reactants are the attachment processes. The following attachment processes are the most dominant of all the attachment processes



The first reaction is a dissociative attachment and the second reaction is three-body molecular attachment. Dissociative attachment is most prevalent at electron energies between 4 to 12 eV, which is right below the primary ionization energy of molecular oxygen. The three-body molecular attachment, Equation (48), is most prevalent at electron energies of 0.1 to 1 eV. Molecular and atomic nitrogen do not form stable negative ions, therefore nitrogen attachment rates are negligible and not considered in the calculations. Recombination reactions occur predominantly at electron energies of less than 0.1 eV or temperatures of less than 910 K (See Appendix C). Some molecular

detachment reactions are very temperature dependent (such as reactions 14 and 15 in Appendix C), hence the rate coefficient of the reaction increases dramatically with increased temperature. The electron affinity between the attached electron and atomic and molecular oxygen is 1.465 eV and 0.44 eV respectively. As a result the electron detachment processes only occurs if the incident electron energy is greater than the attached electron affinity to atomic or molecular oxygen. Since the concentration of both positive and negative ions is very important for determining the recombination and detachment rates in the plasma, the ion-ion and ion-neutral reactions must be considered as well. Most of the reactions in the calculations are not described in this section for the sake of brevity, but a complete listing of all the reactions used in the plasma chemistry calculations can be found in Appendix C.

The reactions in Appendix C were selected to be in the model because they would have a significant impact on the density of the constituents of the plasma. In general, any reaction between molecular oxygen or nitrogen and an ion or electron was selected to be a reaction in the model because of the high density of molecular oxygen and nitrogen. Atom-ion and ion-ion reactions were included if the rate constant of the reaction was sufficiently large that the reaction may have a noticeable effect on the concentrations in the plasma.

From the reactions in Appendix C, 17 single order differential equations were generated to calculate the change in the concentrations of the ions and electrons in the plasma. To better model the electron attachment and detachment processes that occur in certain energy ranges, the electrons were divided into three energy groups of high,

medium, and low energies. Where the low energy is below 0.1 eV, medium is between 0.1 and 4 eV, and high is between 4 eV and 12.3 eV (see Table 11 for more details).

Table 11. Electron Energy Ranges

Classification	Energy Range	Reactions
High	4 to 12.3 eV	$e^{**} + O_2 \rightarrow O + O^-$ $e^{**} + O_2^- \rightarrow O_2 + 2e$ $e^{**} + O^- \rightarrow O + 2e$
Medium	0.1 to 4 eV	$e^* + 2O_2 \rightarrow O_2 + O_2^-$ $e^* + O_2 + N_2 \rightarrow N_2 + O_2^-$ $e^* + O_2^- \rightarrow O_2 + 2e$
Low	< 0.1 eV	See Appendix C

The rate equations were developed from the reactions in Table 11 by treating the electrons in different energy ranges as different elements. This was done so that the population of electrons in a particular energy range could only react with the dominant processes of that energy range. The high and medium energy ranges consist of the dominant attachment and detachment process for that energy range. If a high energy electron detaches an electron from an ion, then the ejected and scattered electrons have a probability of being in any of the three energy ranges based on Mott's ejection energy probability distribution (Chapter III, equation (30)). If a medium energy electron detaches an electron from an ion, then the ejected and scattered electrons have a probability of being in either the medium or the low energy range based on Mott's ejection energy distribution.

The method of dividing the electron energies into different categories was required to obtain a better estimate of the electron densities in the plasma. This is because

reaction 1 in Appendix C is only significant if the electrons have a high energy (greater than 4 eV). Since, only a few percent of the electrons have sufficient energy to react in reaction 1, electrons at higher energies were separated from electrons at lower energies so that only they would be involved in reaction 1. The rate constants for reactions 3 and 4 are very different for electrons at low energies versus electrons at higher energies. Therefore, reactions 3 and 4 were included in both the medium and low energy ranges with a rate constant that was appropriate for the electron energy range.

If we assume that the production rate of thermal electrons into any point in the plasma density is constant, then the electron beam can be treated as a constant source of new electrons into the reaction. The electron beam also provides a source term for the positive oxygen and nitrogen ion rate equations because an equal number of positive ions and electrons must be made (assuming that single ionization dominates). However, it was unknown how many of the thermal electrons will fall within the energy ranges in Table 11. To approximate the thermal electron distribution, the Monte Carlo simulation was run to obtain an approximate end electron energy distribution. The resulting electron energy distribution was exponential and when integrated indicated that approximately 1/3 of the electrons fell within each energy range listed in Table 11. Therefore, the constant source term for each of the electron rate equations is given by the following expression

$$\gamma_{1,2,3} = \frac{\gamma_0}{3\Delta t} \quad (53)$$

where

$\gamma_{1,2,3}$  = electron density source term for a particular energy range

$\gamma_0$  = rate of electron density flow into a volume

$$\Delta t = \text{pulse time length}$$

No cross section data was available for the electron detachment processes described in Table 11, therefore a modified BEB model was used to estimate the detachment cross section for  $O_2^-$  and  $O^-$ . According to Kim, better agreement between the BEB model and experimental data on the ionization of ions was obtained when the *ad hoc* term in the denominator of Chapter III, equation (42) was changed from  $(T + B + U)$  to  $T + (B + U)/2$  at non-relativistic T (Kim, 2000:052710-5). The BEB model yielded the detachment cross section of  $O^-$  and  $O_2^-$  depicted in Figure 27.a and 27.b respectively. By obtaining the electron detachment cross section, a rate coefficient for the electron detachment process can be calculated using the relationship

$$k = \sigma v \quad (54)$$

where

$k$  = reaction rate constant

$v$  = the velocity of the electrons

the average rate constant over the energy ranges of interest was determined for the reactions in Table 11.

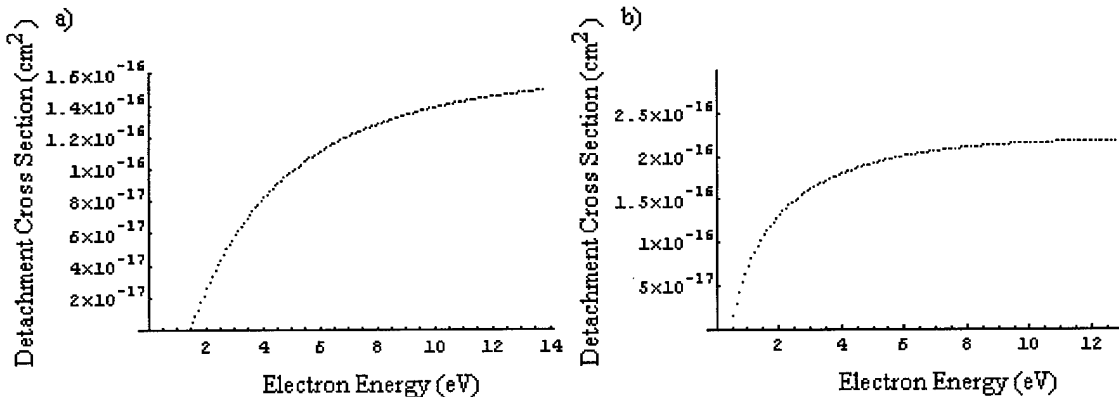


Figure 27. Detachment Cross Sections  
for a)  $O^-$  b)  $O_2^-$

The rate equations developed from Table 11 were combined with the rate equations developed from the chemical reactions in Appendix C to model the temporal evolution of the plasma. Due to the enormous number of reactions that are modeled, a Mathematica code was developed that converted the chemical reactions in Appendix C into the 17 single order differential rate equations that are used to model the plasma chemistry. The resulting rate equations were solved using NDSolve, the numerical differential equation solver in the software package Mathematica.

#### Results of Plasma Chemical Reaction Calculations

The results of the plasma chemistry model, which was developed in the previous section for various electron and ion density source terms, are shown in Appendix D. In Figure 39, the resulting electron and ion densities due to the electron beam being on for 5 ms and then shutting off are shown. The results of these calculations were used to modify the plasma density obtained from the EBS program. This is done so that a better estimate can be obtained for the attenuation and refraction due to a plasma made by an electron beam with a certain power and initial electron energies.

From the figures in Appendix D, we see that the electron density reaches an approximate steady state in a few microseconds regardless of the magnitude of the electron density source terms. The steady state is due mostly to a balance between the three-body attachment reactions 3 and 4 and the electrons generated by the electron beam. From Figures 40.a, 40.b, and 40.c, we see that the steady state density of the electrons is directly proportional to the magnitude of the source term of electrons from the electron beam into the reaction. This relationship can easily be seen if we consider that the loss of electron density due to attachment is much greater than any other loss

mechanisms in the plasma and that the electron density reaches a steady state. From these assumptions, we can approximate the time rate of change of the electron density as

$$\frac{dN_e}{dt} = -k_{a2} N_e N_{o2}^2 - k_{a2} N_e N_{o2} N_{N2} + \gamma_1 = 0 \quad (55)$$

$$N_e = \frac{\gamma_1}{N_{o2}^2 k_3 + N_{o2} N_{N2} k_4} \equiv \frac{\gamma_1}{R_{attached}} \quad (56)$$

where

$N_e$  = electron density

$N_{o2}$  = molecular oxygen density

$N_{N2}$  = molecular nitrogen density

$\gamma_1$  = electron source term due to the electron beam

$k_3$  = rate constant for reaction 3

$k_4$  = rate constant for reaction 4

$R_{attached}$  = rate electrons attach to molecular oxygen

The terms in the denominator of equation (56) are all constant; therefore the electron density is directly proportional to the electron beam source term, which is consistent with the data presented in Figure 39 and Figure 28. This relationship holds for  $\gamma_1$  values from  $10^{11}$  to  $10^{22}$  ( $e^- / s \cdot cm^3$ ).

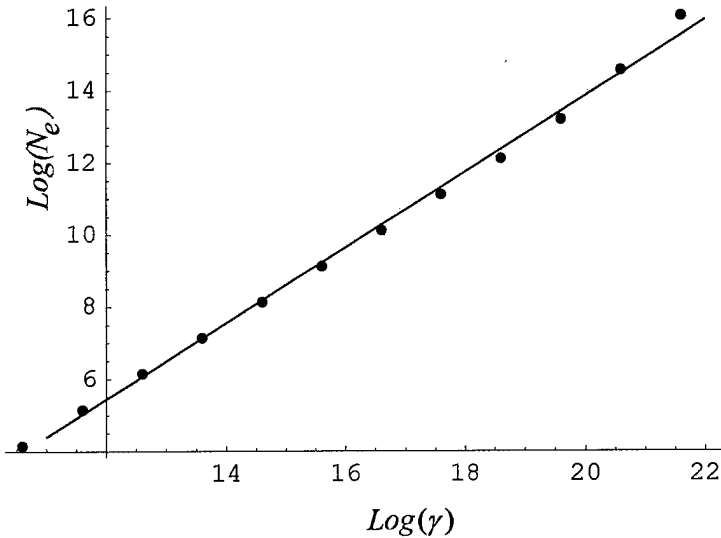


Figure 28. Log of Steady State Electron Density Versus Log of Electron Beam Source Term  $\gamma$

Calculations for electron densities at various pulse durations were used to determine an exact relation between the rate at which the electron beam injects electrons and ions into the plasma and the steady state electron density. In Figure 29, the y-axis is the log of the ratio of the steady state electron density,  $N_e$ , with plasma chemistry losses to the plasma density achieved by pulsing the electron beam for a period of  $\tau_p$ , resulting in an electron density of  $\gamma\tau_p$  for the case of no loss mechanisms. The reason for this analysis is to provide a simple way of translating the electron beam density distribution without losses into a density distribution, which includes losses due to plasma chemistry. This treatment is only appropriate because the electron density with losses achieves a near steady state in a few microseconds; therefore the electron density with losses is approximately constant for the duration of the pulse.

The results of those calculations over the range of pulse lengths between 0.0001 s and 0.005 s are shown in Figure 29. We see that the shorter the pulse duration (therefore,

a higher rate of electrons being inserted into the plasma), the lower the steady state electron density losses due to attachment and recombination. From Figure 29, we see that the percent loss of electron density is approximately the same for all electron and ion injection rates from the electron beam, therefore, we can approximate the plasma loss mechanisms as having a constant percent loss for all electron densities in the plasma. As a result, a constant Plasma Density Loss Factor (PDLF) can be applied to the plasma density without losses to approximate a plasma density with losses.

It should be noted that there is a very large overall reduction in the electron density of the plasma due to the attachment and recombination reactions. For the particular electron and ion density source terms shown in Figure 29.a, the ratio of the steady state plasma density with and without losses is

$$\frac{N_e}{N_0} = \frac{N_e}{\gamma_1 \tau_p} \approx 3 \times 10^{-5} \quad (57)$$

where

$N_0$  = the plasma density without losses after a time  $\tau_p$

$\tau_p$  = pulse width

If we assume again that all other loss or gain mechanisms are negligible compared to the three body attachment processes then, then we may substitute equation (56) into equation (57) to obtain the expression

$$\frac{N_e}{N_0} = \frac{\gamma_1}{(N_{O2}^2 k_3 + N_{O2} N_{N2} k_4) \tau_p} \equiv \frac{\gamma_1}{R_{attached} \tau_p} \quad (58)$$

Since,  $R_{attached}$  is approximately constant then the ratio of the electron densities with and without losses scales as the inverse of the pulse time. From Figure 29, we can tell that

this relationship holds exactly for lower electron injection. The large loss in electron densities is due to molecular oxygen and nitrogen being in very plentiful supply. As a result the majority of electrons become attached to molecular oxygen, hence reducing the electron density by several orders of magnitude through out the plasma. Also as a result of the rapid attachment rate, the plasma becomes a positive and negative oxygen ion plasma, which may result in the negative and positive oxygen ions becoming the dominant term in determining the plasma frequency.

In Figure 29, the slight decrease in the ratio of electron densities,  $N_e/N_0$ , at medium injection rates is due to recombination reactions 7, 10, and 46, which contribute to the electron losses due to the higher densities of positive ions. The ratio  $N_e/N_0$  increases rapidly at the highest electron injection rates because the electron densities increase fast enough that the detachment processes can free a significant portion of the electrons bound to the negative oxygen ions.

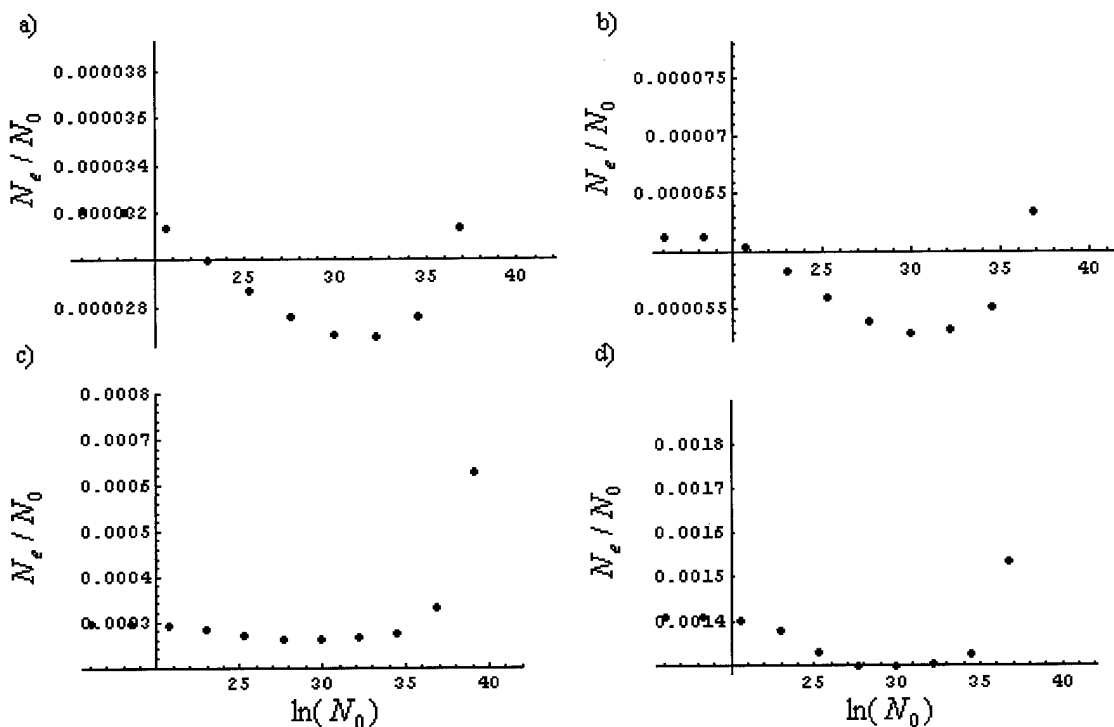


Figure 29. Ratio of Electron Densities with and without Loss Mechanisms versus the Log of the Initial Electron Density at Different Pulse Lengths of  
 a) 0.005 s b) 0.0025 s c) 0.0005 s d) 0.0001 s

It should also be noted from the figures in Appendix D that the electron densities diminish very rapidly when the electron beam is turned off. However, from Figure 39, we see that the negative molecular oxygen ion density remains fairly constant after the electron beam is shut off. Since the electron densities are negligible, the plasma frequency will be a function of the negative oxygen ion density whose plasma frequency is approximately two orders of magnitude less than the plasma frequency for an equivalent electron-positive ion plasma. To achieve a negative molecular oxygen ion plasma frequency near a GHz, and hence a significant degree of attenuation of an EM wave in the GHz range, after the electron beam has been turned off requires an extraordinarily high negative ion density ( $10^{13}$ - $10^{14}$  e<sup>-</sup>/cm<sup>3</sup>). Therefore, when the electron

beam is off, the plasma density will not be sufficient to attenuate or refract an EM wave in the range of frequencies presented in this study.

The calculations of the last section were a rough estimate of the reactions that would occur in the plasma. The air molecules are assumed to be unheated and have a temperature of 300 K, however this assumption may not hold if the electron beam is operated for a long period of time at a higher power setting. The change in electron energies was also modeled very coarsely with the high, medium, and low energy ranges and should be examined rigorously with a Boltzmann transport calculation to obtain a better estimate of the temporal evolution of the plasma density.

In this last section, we have developed a means to gauge the loss of plasma density due to attachment and recombination mechanisms. The ratio of the electron densities of the plasma with and without losses was shown to be constant over the entire density range of the plasma, therefore an attenuation factor can be applied uniformly to the plasma density without losses to estimate the effects of the loss mechanisms on the plasma density.

## V. Results and Conclusions

This chapter presents results derived from the computer programs Electro-Magnetic Wave Propagation Model (EMWPM) and the Electron Beam Scattering (EBS) simulation and the plasma chemistry model described in the previous section. The primary purpose of this chapter is to demonstrate the capability of the computer models developed in the previous chapters to quantify the plasma density distribution resulting from the injection of a relativistic electron beam into air. The data presented in this chapter is limited, because the parameter space for the scenario is quite extensive and very dependent on the environment in which the electron beam will be utilized.

### Plasma Density and Spatial Distribution

This section presents the results obtained from the EBS computer program described in Chapter IV. The results of the density distribution of the plasma without losses mechanisms as predicted by the EBS simulation are shown. The results of the EBS simulation, which describes the spatial extent of the plasma when using the electron beam at various initial electron energies and altitudes is also reported. Finally, the section concludes with a summary of how the descriptive statistics of the plasma reported by EBS are used to generate a plasma density distribution.

### Static Plasma Distribution

In Table 12, the run matrix for the EBS program at different altitudes and at different initial electron energies is shown. This run matrix was executed in order to explore the parameter space of longitudinal extent, transverse extent, and densities of the electron beam generated plasma. The main output of EBS includes the number of

electrons per cm in the axial direction, mean and standard deviation of the transverse distribution, and a file containing a two dimensional map of the plasma electron densities. A sample of the results from two different EBS simulations at 500 keV and 300 keV initial electron energies are shown in Figure 30. The simulation parameters for all the runs performed in this section can be found in Table 13.

Table 12. Run Matrix

Electron Energy	Altitudes	Air Number Density
100 keV	0 m	$2.69 \times 10^{19} \text{ cm}^{-3}$
300 keV	2500 m	$1.98 \times 10^{19} \text{ cm}^{-3}$
500 keV	5000 m	$1.46 \times 10^{19} \text{ cm}^{-3}$
750 keV	7500 m	$1.07 \times 10^{19} \text{ cm}^{-3}$
1 MeV	10000 m	$7.91 \times 10^{18} \text{ cm}^{-3}$

Table 13. EBS Parameters for all Simulation Runs

Parameter	Value	Parameter	Value
Power	10,000 W	Use Exponential Atmosphere	True
Pulse Length	0.5 ms	Elastic Collisions	True
Num Simulated Electrons	1500	Inelastic Collisions	True
Move Created Electrons	False		

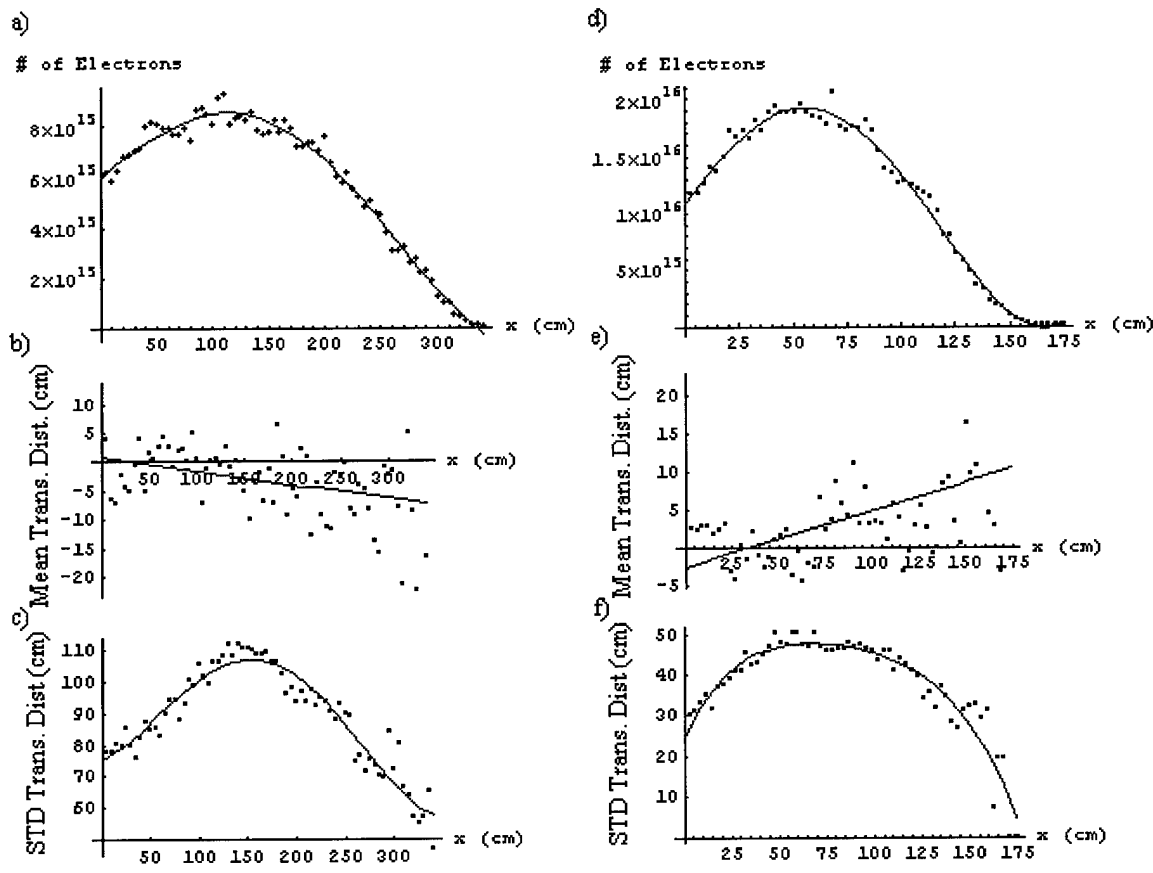


Figure 30. Plasma Distribution Results from the EBS simulation

a) Axial Density Profile for 500 keV  $e^-$  b) Mean of Transverse Distribution for 500 keV  $e^-$  c) STD of Transverse Distribution for 500 keV  $e^-$  d) Axial Density Profile for 300 keV  $e^-$  e) Mean of Transverse Distribution for 300 keV  $e^-$  f) Mean of Transverse for 300 keV  $e^-$

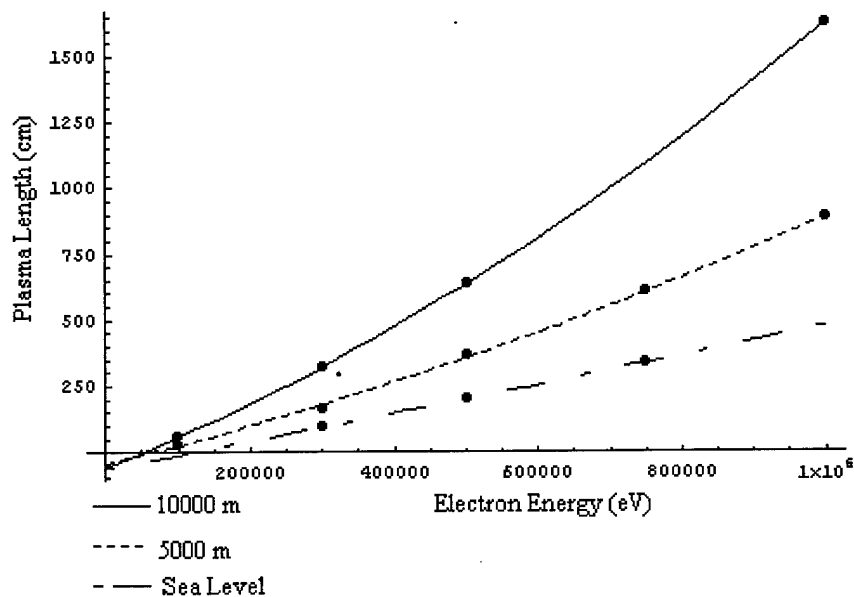
In Figure 30, the axial and transverse distribution plots are both fit with a fourth order polynomial and the mean transverse distribution plot was fit with a linear function. (Which was the case for all the results from the EBS simulation). The axial density profile predicted by the EBS simulation is shown in Figure 30.a and Figure 30.d. The results of the EBS simulation with lateral scattering of electrons indicate that the maximum in the axial density will be located near the center of the profile, whereas the results without lateral scattering show that the maximum electron density is located near the end of the profile, which are shown in Figure 26. The peak value in the non-lateral

scattering case was due to the ionization cross section achieving a maximum value at low electron energy levels. For the lateral scattering case, the few electrons that travel the farthest in the x direction are those electrons that have experienced the least deflection and hence least energy loss due to inelastic collisions. However, the majority of the electrons experience a larger degree of deflection at an earlier time in their propagation. This results in the electrons traveling in the transverse direction to the beam. Even though the distance traveled through the air is the same for the scattered electrons, they do not travel as far in the axial direction. This behavior results in a maximum in the center rather than at the end of the axial electron density profile.

In Figure 30.c and 30.f, a standard deviation (STD) is used to measure the transverse extent of the plasma because the transverse distribution of the plasma is Gaussian. The STD describes the radial position at which the Gaussian distribution is at half its maximum value, hence it is related to the transverse extent of the plasma. The reason that the transverse distribution is Gaussian is described later on in this section. From Figure 30.a and 30.d, we notice that the length of the 500 keV profile is nearly twice the length of 300 keV profile. As a result, the number of electrons per cm doubles from Figures 30.a to 30.d for the fixed power condition. We also notice that the transverse standard deviation of the 500 keV electron beam is roughly twice the transverse standard deviation of the 300 keV electron beam. The reason for the doubling of the transverse and longitudinal extent of plasma is because the electrons with 500 keV energy can experience nearly twice as many collisions as the 300 keV electrons before becoming thermal electrons, hence allowing the 500 keV electrons to travel nearly twice as far. Also the higher energy electrons have a smaller collision cross section, hence they

have a longer mean free path, resulting in an overall larger longitudinal and transverse extent to the plasma density distribution. Therefore, at the same power settings and pulse duration the density of the 300 keV plasma will be roughly 8 times greater than the 500 keV plasma, potentially resulting in a huge difference in the attenuation and refraction resulting from the two plasmas. It should also be noted that the shape of the longitudinal and transverse electron density profile is only a function of the initial energy of the electrons in the electron beam. Therefore, if the initial electron energy is kept the same, then the electron density is linearly proportional to the electron beam power.

The results of the run matrix in Table 12 are shown in Figure 31. The fit to the data in Figure 31 is a quadratic function, because the ionization cross section decreases slightly with increased electron energy. This slight decrease in cross section results in a slightly longer mean free path for higher energy electrons, hence the higher energy beam's longitudinal extent is not linearly proportional to the energy of the electrons.



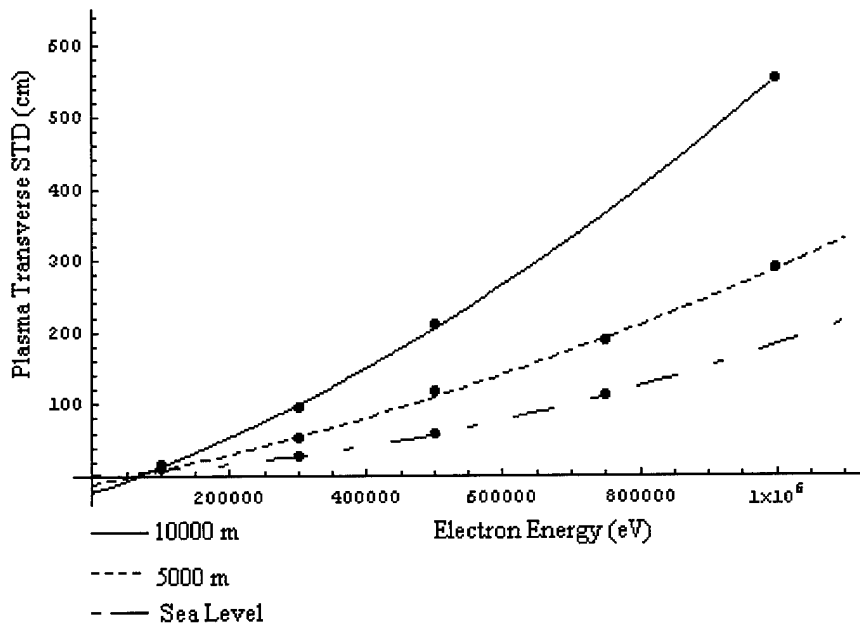


Figure 31. Maximum Length and Displacement of Plasma versus Electron Energy at Various Altitudes  
a) Plasma Length b) Plasma Transverse STD

It should be noted that Figure 31.b represents one standard deviation (STD) in the transverse plasma distribution (i.e. 68% of the electrons are within that radius, 98% of the electrons are within twice the radius), therefore there is still a non-zero plasma density at transverse distances exceeding the values given in Figure 31.b. If the plasma density and hence the plasma frequency is high, then the plasma density out to the second standard deviation may be adequate to attenuate an EM wave.

Figure 32 shows how the standard deviation and length of the plasma vary with altitude. The function used to fit the data presented in Figure 32 is the inverse of the function used to determine the number density of the air at various altitudes ( $\exp(y/H)$ ), where  $y$  is the altitude and  $H$  is the scale height of the atmosphere. From this result, we conclude that the longitudinal extent and STD in the transverse direction are inversely proportional to the number density of the atmosphere. This is not surprising because the

function controlling the time that the electron travels between collisions (Chapter IV, equation (30)) is inversely proportional to the number density of the plasma.

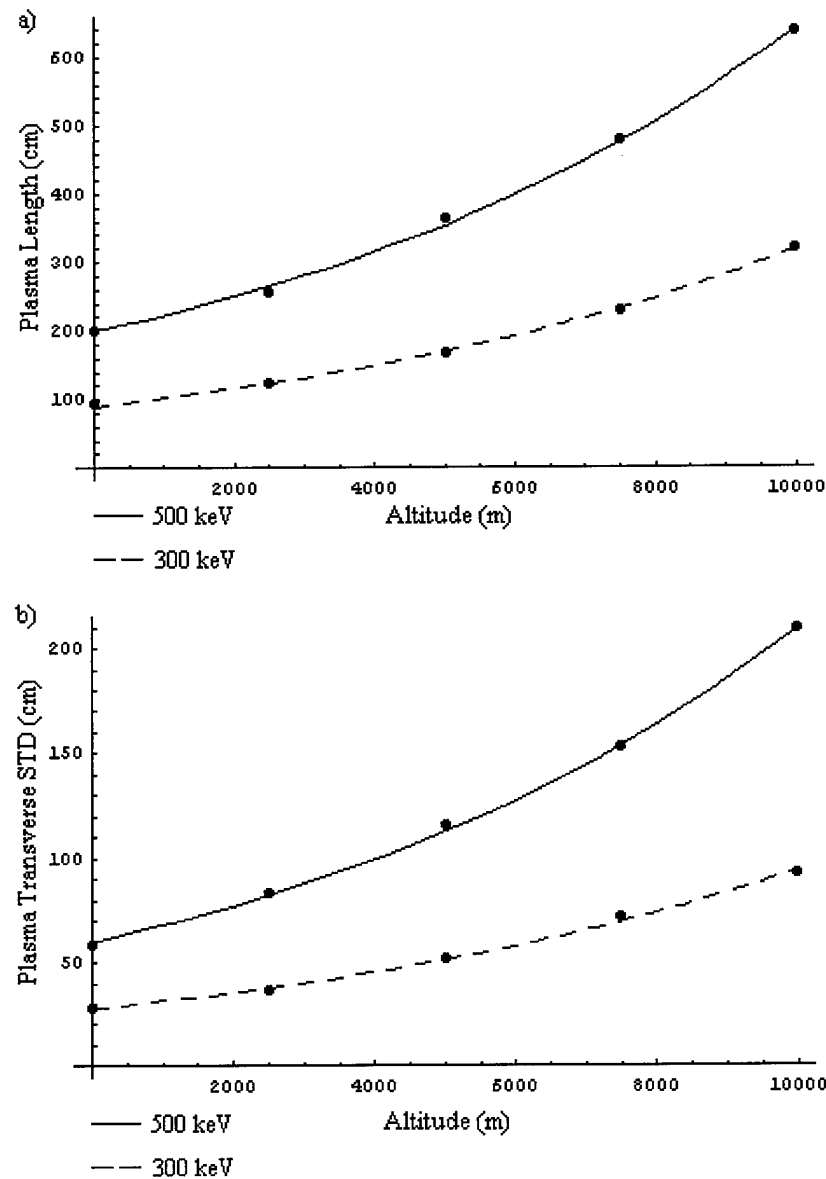


Figure 32. Plasma Profile versus Altitude  
a) Plasma Length b) Plasma Transverse STD

The functions obtained by fitting the data in Figure 30 were used to develop a density map of the plasma. The reason for using the fit of the data rather than the data itself is that the spikes in the EBS data create problems in the propagation model. Fermi

and Bethe both predicted that the transverse distribution of a beam of electrons undergoing multiple collisions would be Gaussian (Orear, 1950:36). In Figure 33, samples of the transverse distribution predicted by EBS are shown.

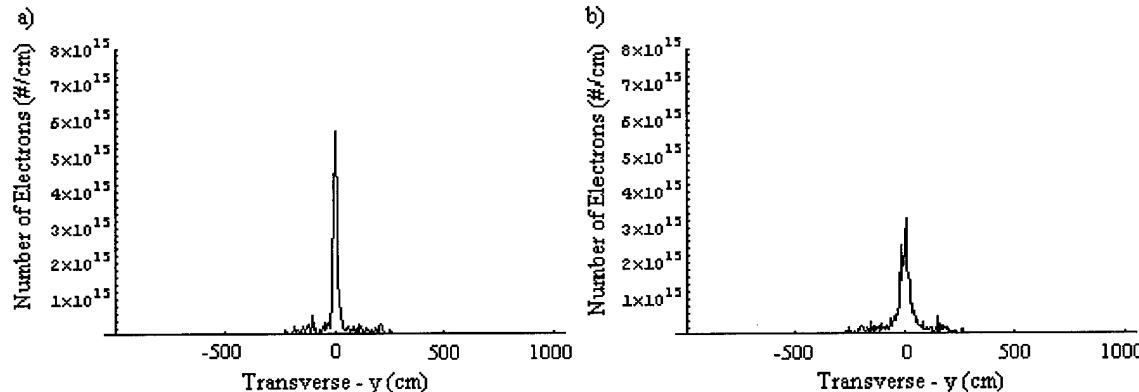


Figure 33. Transverse Distribution of the Electron Beam Generated Plasma for Electron Energies of 500 keV at Axial Distances of a) 35 cm b) 55 cm

From this information and the functions fit to the data in Figure 30, the following empirical model describing the number of electrons in the plasma at a point was developed

$$N(x, y) = \frac{f(x)}{\sqrt{2\pi g(x)^2}} \exp\left[\frac{-y^2}{2\pi g(x)^2}\right] \quad (1)$$

where

$N(x, y)$  = number of electrons at coordinate  $(x, y)$

$f(x)$  = fit of the axial electron number data

$g(x)$  = fit of the transverse standard deviation data

The EBS simulation was limited to two-dimensions, therefore to calculate the density of the electron beam we will now consider the third dimension. To do this we will use a cylindrical coordinate system in which the Cartesian coordinates  $(x, y, z)$  are transformed to cylindrical coordinates  $(z, r, \theta)$ . Since, Mott's elastic scattering and ionization cross

sections were isotropic in the scattering and ejection angle distribution of the angles  $\phi$  and  $\psi$  respectively (see Chapter III, Mott's Ionization Cross Section), the electron beam will be isotropic in the angle  $\theta$  as well. To obtain the plasma density for a cell in the plasma, the following equation was used

$$\rho = \frac{\int_{z1}^{z2} \int_{r1}^{r2} \frac{f(z)}{\sqrt{2\pi g(z)^2}} \exp\left[\frac{-r^2}{2\pi g(z)^2}\right] dr dz}{\frac{1}{2} \int_{z1}^{z2} \int_{r1}^{r2} 2\pi r dr dz} \quad (2)$$

where

$r1$  = inner radius of cell

$r2$  = outer radius of cell

$z1$  = shorter axial distance

$z2$  = longer axial distance

Analytically integrating with respect to  $r$  we obtain the expression

$$\rho = \frac{\int_{z1}^{z2} \frac{f(z)}{2} \left( \Gamma\left(\frac{r2}{\sqrt{2g(z)}}\right) - \Gamma\left(\frac{r1}{\sqrt{2g(z)}}\right) \right) dz}{\frac{\pi}{2} (r2^2 - r1^2) (z2 - z1)} \quad (3)$$

where

$\Gamma(x)$  = the gamma function

Numerically integrating equation (3) using a step integration method we obtain the expression

$$\rho = \frac{\frac{f(z1)}{2} \left( \Gamma\left(\frac{r2}{\sqrt{2g(z1)}}\right) - \Gamma\left(\frac{r1}{\sqrt{2g(z1)}}\right) \right)}{\frac{\pi}{2} (r2^2 - r1^2)} \quad (4)$$

for the plasma density in a cell with length ( $z2 - z1$ ) and width ( $r2 - r1$ ). Equation (4) is used to generate the plasma density tables used by the EWMPM program, which in turn allows the EMWPM program to determine the refraction and attenuation of an EM wave as a result of the plasma distribution calculated by the EBS program. A contour plot of the plasma density resulting from equation (4) is shown in Figure 34. The contour plot represents a two dimensional slice of the plasma density generated by the electron beam generator. The Gaussian shape of the electron distribution in the radial direction and the natural dispersion due to electrons at larger radial distances from the center of the electron beam being distributed over a larger volume, results in a plasma that is very dense near the center of the beam and decreases in density very rapidly in the radial direction. The shape of the density contour plot is a function of the electron energy and not the electron beam current, however, the number of electrons and hence the electron density is a function of the electron beam current. Therefore, the plasma density scales linearly with electron beam power for electrons at a constant energy. Also note that the STD of the electron beam achieves a maximum value at an intermediate range. Similarly, the longitudinal profile achieves a maximum in the vicinity of this same range.

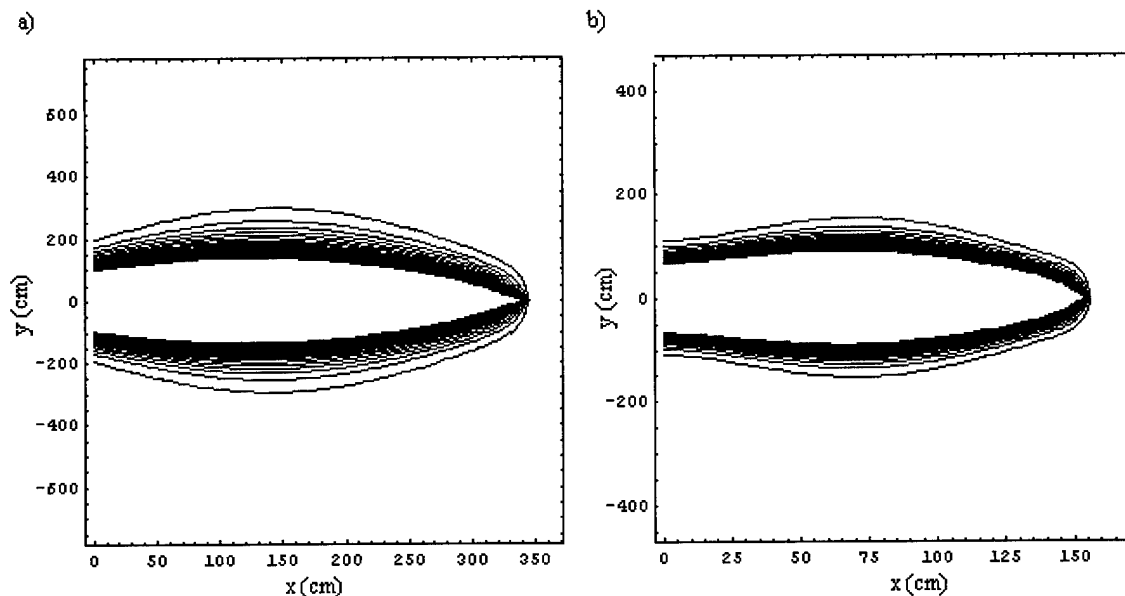


Figure 34. Contour Plot of Electron Beam Generated Plasma  
a) 500 keV Electron Beam b) 300 keV Electron Beam

#### EM Wave Attenuation and Refraction due to the Plasma Density Distribution

This section presents the results obtained from the EMWPM program on the refraction and attenuation of an EM wave by an electron beam generated plasma with and without plasma chemistry losses. The refraction of an EM wave by an electron beam generated plasma is presented in the first subsection. The last two subsections contained in this section summarize the average attenuation achieved by the plasma with or without losses over a range of EM wave frequencies.

#### Distortion of the Electromagnetic Wave Front

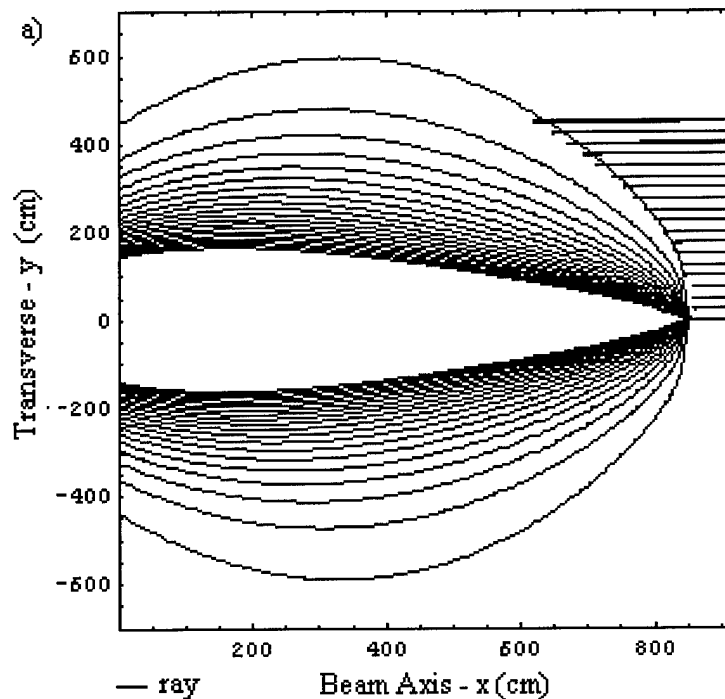
The purpose of this section is to demonstrate the capability of the EMWPM program to determine the refraction of an EM wave with finite spatial extent as it traverses an electron beam generated plasma. The analysis is limited to a plasma generated by a single electron beam at 1 MeV electron energy and an air density corresponding to an altitude of 5 km.

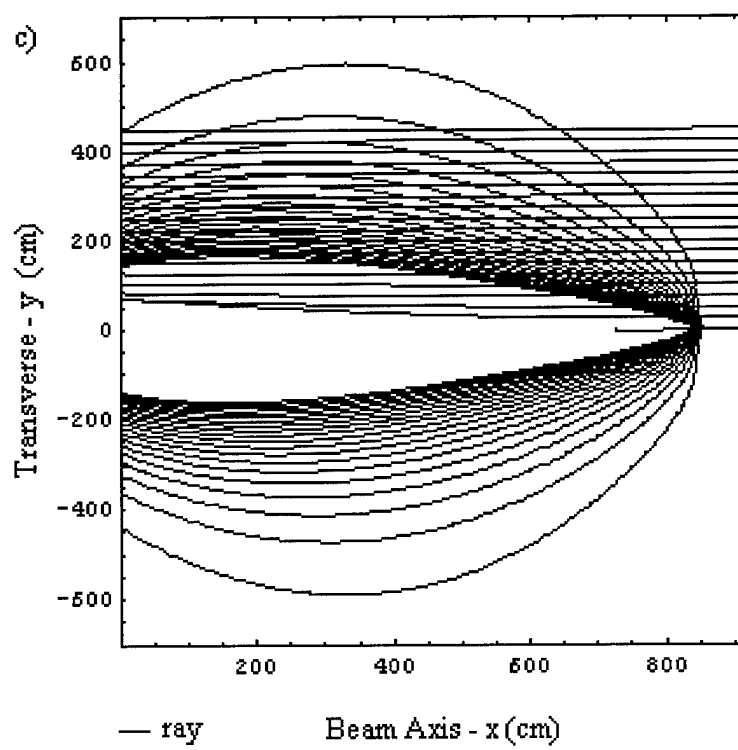
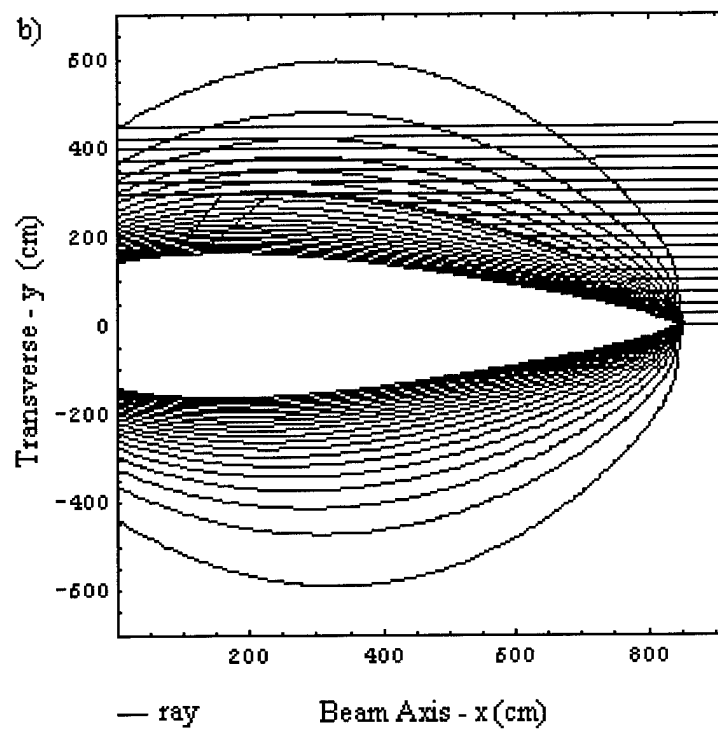
The main purpose of refraction in the EMWPM model is to assure the path of the ray through the plasma is accurate allowing for accurate calculations of the plasma frequency. The higher accuracy of the plasma frequency along the path EM wave, results in a higher accuracy in the attenuation calculations for the plasma. The analysis provided below is a qualitative assessment of the results of the EMWPM program.

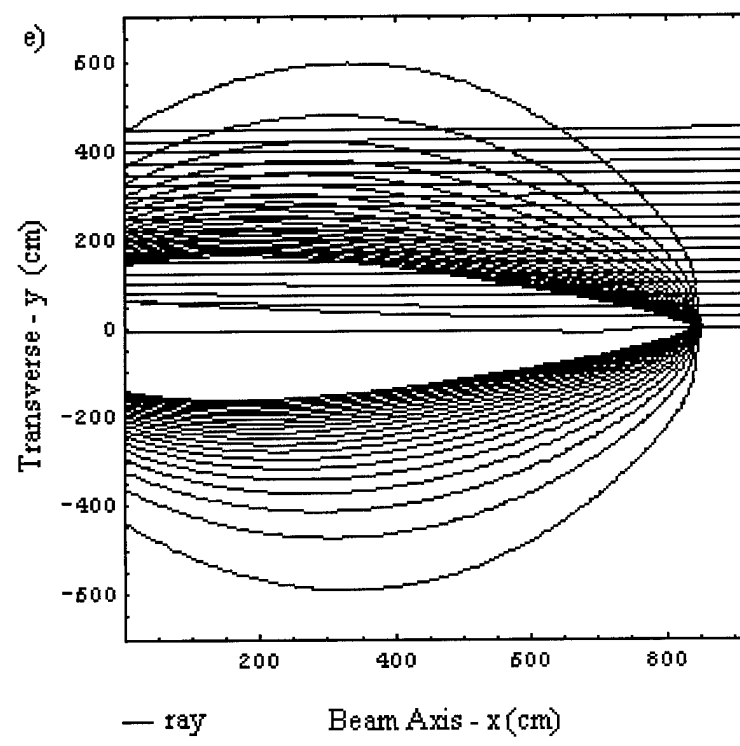
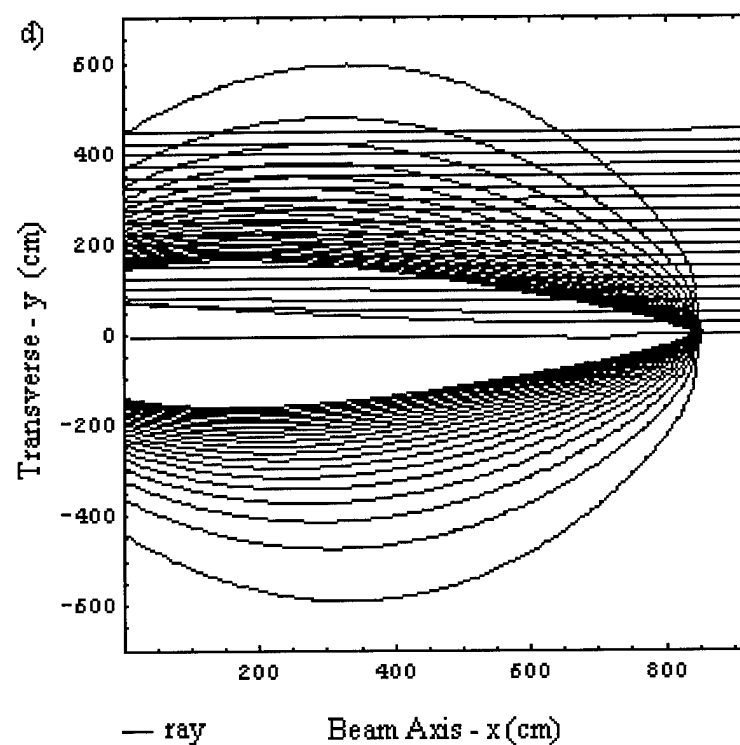
The index of refraction of the plasma is highly dependent on the EM wave and plasma frequencies, and to some degree the collision frequency of the plasma (Chapter I, equation (11)). In general, the closer the plasma frequency is to the EM wave frequency, the lower the index of refraction of the plasma. The lower the index of refraction and/or the larger  $\vec{\nabla}n$ , the more that the wave will be refracted in the direction of the gradient of the plasma density (see Chapter II, equation (1)), which in general is pointing away from the electron beam source for the case of the electron beam generated plasma. This happens because the radius of curvature of the EM wave is proportional to  $\vec{\nabla}n$  and inversely proportional to  $n$ . If the EM wave frequency is less than the plasma frequency then the EM wave will be reflected. If the EM wave is reflected then the plasma will not attenuate the EM wave because it does not propagate through the plasma.

In Figure 36, the attenuation of an EM wave over the radial range of 0 to 5 m at various frequencies is shown. The refraction analysis is only done over half the plasma, because the plasma distribution is symmetric about the x axis. In Figure 37.a, an EM wave at a frequency of 300 MHz traverses a plasma predicted by the EBS program. The plasma frequency varies between 400 MHz to 7 GHz in the radial range between 0 and 5 m, therefore, the 300 MHz EM wave reflects off the plasma. For the 1 GHz frequency shown in Figure 36.b, the EM wave propagates through edges of the plasma unrefracted

where the plasma frequency is lower. As the plasma frequency increases towards the center of the plasma, the refraction of the EM wave is greater. At the center of the plasma, the EM wave is reflected because the plasma frequency is greater than the EM wave frequency. At 5 GHz, the EM wave penetrates the majority of the plasma, but is noticeably refracted. As the frequency of the wave becomes larger than 5 GHz, the EM wave is refracted even less resulting in very little distortion of the EM wave front.







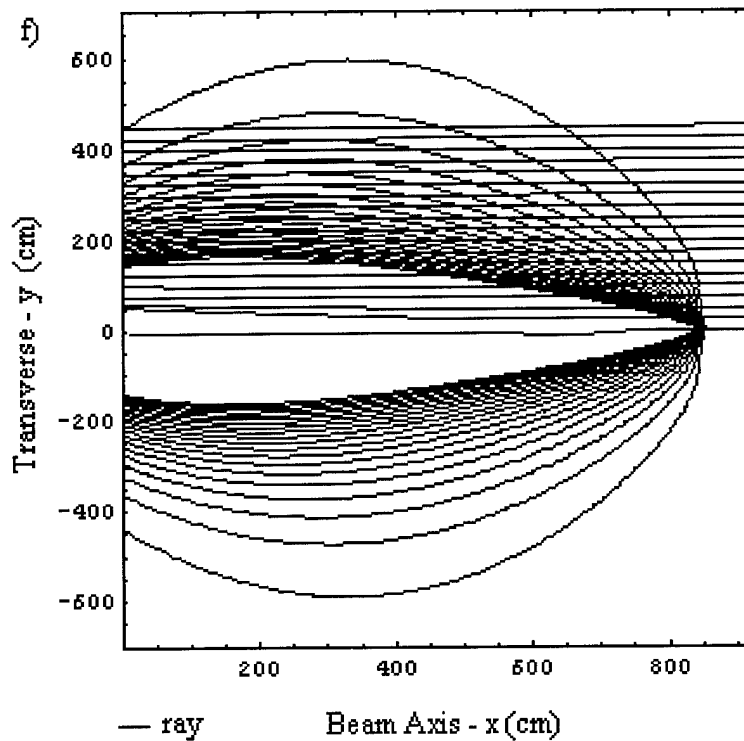


Figure 35. Refraction in the Electron Beam Plasma at 5 km Altitude 100 kW, and Electron Energy of 1 MeV for Frequencies of a) 300 MHz b) 1 GHz c) 5 GHz d) 10 GHz e) 20 GHz f) 30 GHz

#### Spatial Variations in Attenuation

The purpose of this section is to demonstrate the capability of the EMWPM program to quantify the power attenuation that occurs over the width of the incident wave. The analysis is limited to a plasma generated by a single electron beam with energies between 300 keV and 1 MeV at 5 km altitude. A more in depth study should be performed to better characterize the attenuation properties of the plasma in different environments.

The plasma density of the electron beam generated plasma decreases as  $e^{-r^2/c}$  in the radial direction, which results in a large variation in the plasma density over a short

radial distance. The amount of power attenuation over the width of the incident wave front at various frequencies is shown in Figure 37. The graphs in Figures 35 and 37 give the complete picture of the refraction and attenuation resulting from a 1 MeV electron beam. In Figure 37.a, the attenuation for a wave frequency of 300 MHz is shown. The amount of attenuation is quite low because the EM wave was reflected due to the frequency being lower than the plasma frequency. In Figure 37.b, low attenuation is observed within a 100 cm of the center of the electron beam because the frequency was less than the plasma frequency in that range as well. However at 125 cm and greater radial distance, the rays are refracted rather than reflected, therefore they experience between -7 to -24 dB attenuation. The rays past 125 cm are refracted such that they propagate through a lower density region of the plasma and hence attenuate less. In Figure 37.c no rays are reflected immediately, therefore all rays attenuate. The center rays are attenuated the most because the plasma density is the highest near the center and falls off exponentially towards the edges of the plasma. The EM wave in Figure 37.c is attenuated more than any other frequency because it is closest to the plasma frequency. This relationship is clearly seen in Figure 36, where the complex index of refraction reaches a maximum value when the ratio of the EM wave frequency to the plasma frequency,  $\omega/\omega_p$ , is approximately equal to one. Also Figure 36 indicates that for the ratio of  $\omega/\omega_p$  greater than 1.5 the complex index of refraction asymptotically approaches zero, hence resulting in negligible attenuation at EM wave frequencies much greater than the plasma frequency.

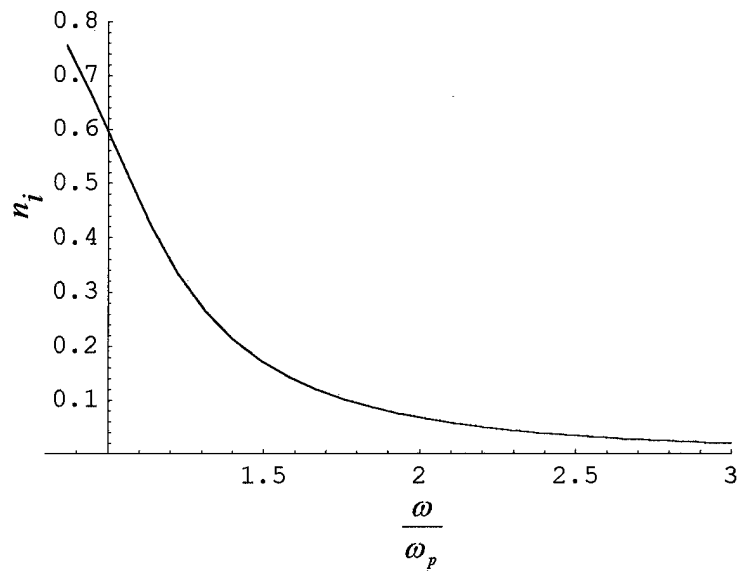
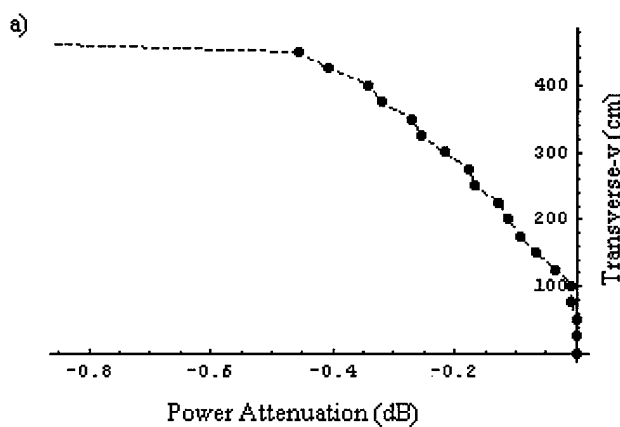
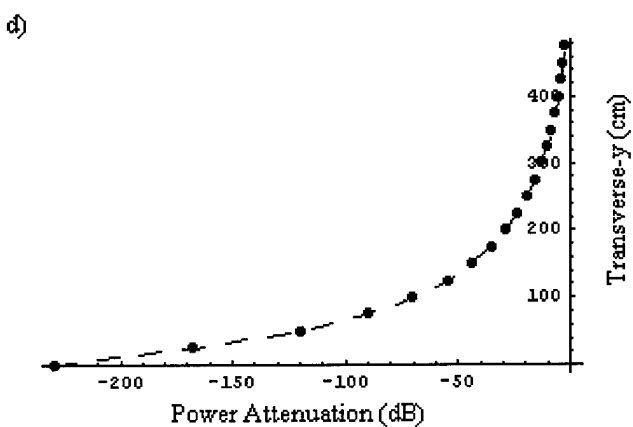
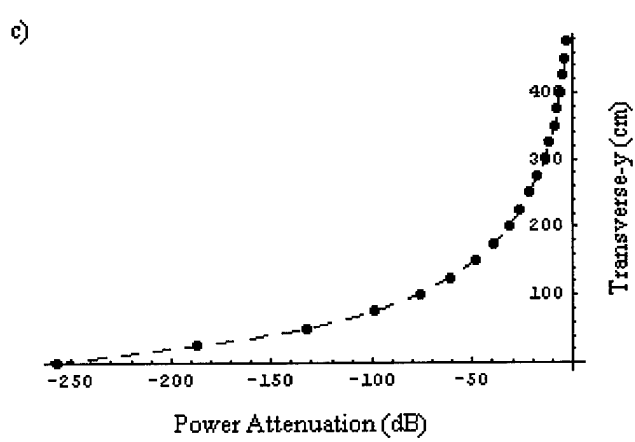
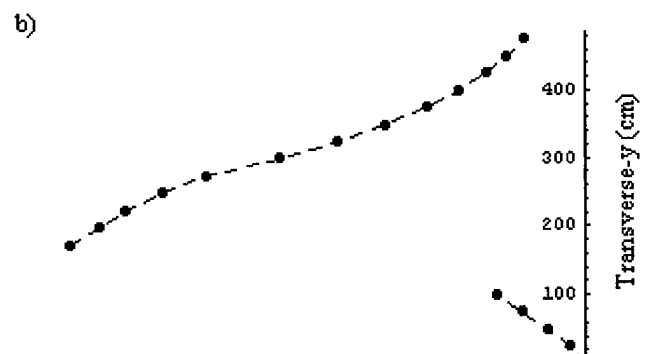


Figure 36. Plot of the Imaginary Index of Refraction,  $n_i$ , versus  $\omega/\omega_p$  with a  $v/\omega_p$  of 0.5

For frequencies in excess of 5 GHz, the attenuation decreases steadily as the EM wave frequency becomes much larger than the plasma frequency, which corresponds with the behavior of the imaginary index of refraction shown in Figure 36.





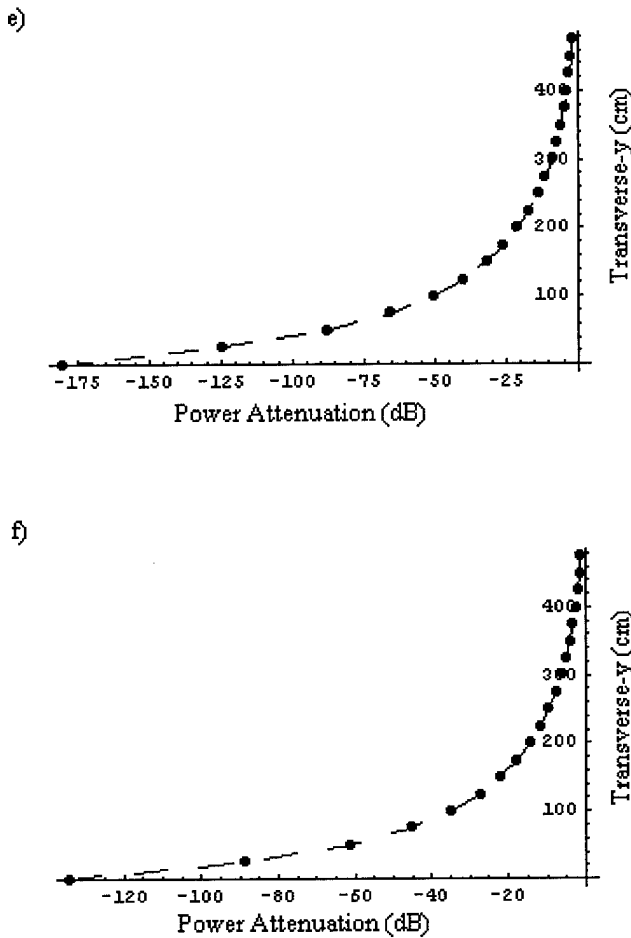
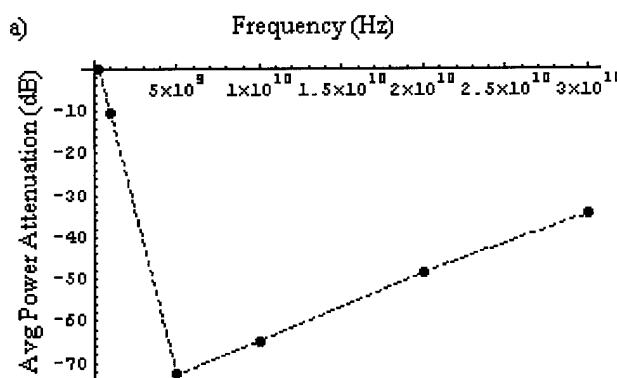


Figure 37. Spatial Attenuation at 5 km Altitude  
for Wave Frequencies of a) 300 MHz b) 1GHz c) 5 GHz  
d) 10 GHz e) 20 GHz f) 30 GHz

The analysis of the spatial attenuation of the EM wave was performed for the initial electron energies between 300 keV and 1 MeV, at a fixed electron beam power, to gain some insight into the attenuation resulting from different density profiles of the plasma. For the EM wave frequency analysis, the spatial attenuation of the plasma was averaged over a radius of 5 m to obtain an average attenuation factor. The attenuation factor was then plotted versus frequency for several electron beam energies. Figure 38 indicates that attenuation is larger at lower EM wave frequencies when the electron beam

has higher electron energies because the plasma density is lower. For higher frequencies, lower electron energies are needed for greater attenuation, because plasma density increases due to the smaller plasma volume, hence the plasma frequencies are nearer to the higher EM wave frequencies. However, there is a point where lower electron energies result in a beam with a restrictive radial extent. If attenuation at higher frequencies is desired then the electron beam generator may be operated at lower electron energies, resulting in only a portion of the EM wave near the centerline being attenuated and as a result any attenuation in the radial wings is negligible. This solution results in larger attenuation of the EM wave over a broader band of frequencies. Whereas the higher electron energies provide a broader spatial coverage, but the range of highly attenuated frequencies is limited.



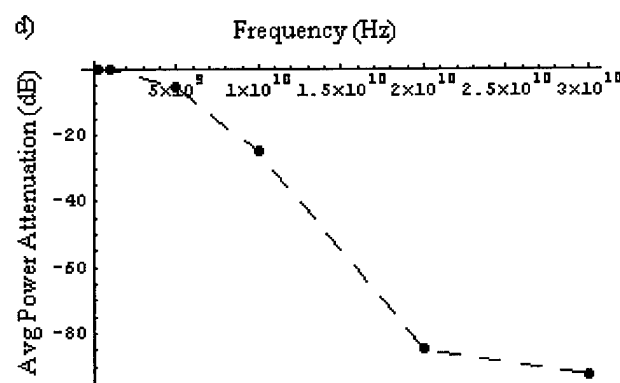
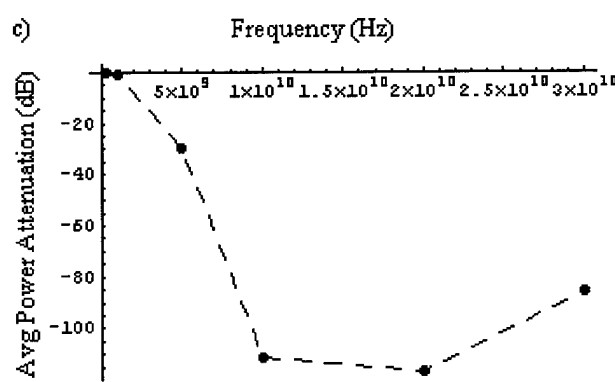
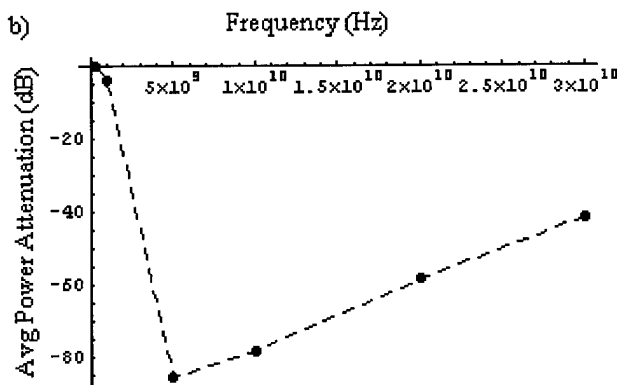


Figure 38. Attenuation versus Frequency at 5 km Altitude  
for Initial Electron Energies of a) 1 MeV b) 750 keV  
c) 500 keV d) 300 keV

### Spatial Variations in Attenuation Considering Plasma Loss Mechanisms

In the Plasma Density Loss Mechanisms section of Chapter IV, it was shown that the plasma reached an approximate steady state in a few microseconds at all electron and ion density injection rates of interest. As a result, the effects of electron attachment, detachment, and recombination on the plasma density were approximated as a constant loss factor to the plasma density referred to as the Plasma Density Loss Factor (PDLF). Therefore, to determine the plasma density distribution with loss mechanisms, we can simply multiply the plasma density without loss mechanisms by the PDLF. From Figure 29, we see that the lowest PDLF is achieved by operating the electron beam for 0.1 ms, which results in a PDLF of 0.00134. Since in the previous section the electron beam was operated for 0.0005 s at 100 kW, we must increase the power by a factor of 5 to maintain the same pulse energy resulting in an electron beam power of 500 kW. The plasma density distribution resulting from the application of the attenuation factor results in a negligible amount of attenuation (less than 10 dB for all frequencies).

### Summary and Conclusions

The objective of this study was to develop a suite of computational tools to analyze the propagation of an electromagnetic wave in a plasma generated by injecting a relativistic electron beam into the air. The suite had three major physical components: electron beam propagation and plasma generation, evolution of the plasma densities due to plasma chemistry, and EM wave propagation. These components were translated into three separate computer programs. Data generated in the programs were post-processed

using Mathematica, which provided analytic fits to source terms, particle densities, and a graphical interpretation of system characteristics.

The spatial extent and density distribution of the thermal plasma source generated by injecting a relativistic electron beam into the air were investigated using a stochastic approach based on an axisymmetric Monte Carlo model. Establishing a reliable set of cross sections for this simulation was crucial. A thorough review of the literature resulted in an experimentally consistent set appropriate for this analysis: species specific and relativistically correct. The differential and total cross sections for scattering and ionization of Mott, Bethe, and Kim were analyzed and incorporated into the Monte Carlo simulation. The Monte Carlo calculation was validated using a limited case in which electrons only experienced forward scattering and were limited to losing an average ionization energy per ionization process. The results of a limited study were consistent with independent analytic and numerical implementations. Once the Monte Carlo simulation was validated, the data associated with the general solution was analyzed and the parametric dependence of the source footprint explored. A limited exploration of the dependence of the plasma distribution on neutral densities and the initial electron energies provided scaling relations. The longitudinal extent of the plasma varied linearly with respect to the energy of the electron beam, as did the transverse extent. Both the longitudinal and transverse extent varied inversely with respect to the neutral density, which translates into an altitude dependence if an exponential atmosphere model is employed. For a density associated with an altitude of 5 km, the plasma longitudinal extent ranged from 52 to 868 cm and the standard deviation of the transverse radial extent ranged from 18 to 292 cm for initial electron energies between 100 keV and 1 MeV.

The plasma source distribution from the Monte Carlo model was used in the second code, a spatial and temporal solution of the plasma evolution based on a time dependent analysis of the plasma rate equations in air. Only volumetric processes were considered. A set of relevant kinetic rate coefficients and species rate equations were assembled and a time-dependent, spatially resolved solution of the plasma densities was achieved using a numerical integration of the coupled equations. For the conditions examined, a pseudo-steady state of the electron density is achieved. The resulting plasma is a three component plasma consisting of electrons, positive ions and negative ions. The negative ions of molecular oxygen are the majority negative species due to the rapid three-body attachment process at the neutral densities considered. The rate equation results were interpreted by employing a simplified, steady state analysis. The values of the electron and negative ion density were established analytically and the scaling with respect to electron beam current explored and explained. For the range of electron beam pulse lengths between 5 ms and 0.1 ms, the density of the electrons in an air plasma produced by an electron beam will be reduced by a factor between  $3 \times 10^{-5}$  to  $2 \times 10^{-3}$  respectively, due to attachment and recombination processes.

The third code developed evaluates the attenuation and refraction of an EM wave in a plasma of arbitrary spatial distribution. A ray tracing method based on the eikonal approach of Sommerfeld was implemented numerically and validated against analytic solutions relating to radio wave propagation in the ionosphere. This approach enabled evaluation of both wave refraction and absorption. Neglecting attachment, the resulting plasma was also found to significantly refract and attenuate the EM waves at reasonable electron beam power settings and pulse lengths. The amount of refraction was very

dependent on the proximity of the plasma and the EM wave frequencies. If the plasma frequency over the transverse extent of the plasma was much larger or smaller than the EM wave frequency then very little refraction occurred. However, if the values of the plasma and EM wave frequencies were close, then the EM wave was refracted by a significant amount.

In summary, this study successfully integrated plasma generation, plasma evolution and wave propagation analyses to permit a quantitative evaluation of the effects of an electron beam generated plasma on an EM wave. The EBS simulation was capable of characterizing the plasma density distribution resulting from a relativistic electron beam. The EMWPM program was also capable of determining refraction and attenuation of an electromagnetic wave traversing an arbitrary, collisional plasma. The plasma chemistry model also demonstrated its ability to analyze the temporal evolution of the plasma due to the chemical processes in the plasma and translate those results into a reduction of the plasma density distribution over time. These models are very flexible and should be used to further examine the parameter space.

#### Limitations of the Study and Recommendations

For the plasma chemistry calculation the change in energy of the thermal electrons from high to low energies due to inelastic collisions with molecules and ions was modeled very coarsely and a more refined calculation should be used such as a Boltzmann transport calculation. The electron temperature calculations are important because the rate constants for attachment and detachment processes are very dependent on the temperature of the electrons (such as attachment reactions 3 and 4 in Appendix C). Given the importance of attachment loss mechanisms and the dependence of these

processes on the energy distribution of the thermal electrons, a refined treatment of thermal electrons is appropriate. Spatial variations in the electron temperature throughout the plasma were also not considered in the study. Spatial variations in the electron temperature will result in different collision frequencies and hence a different amount of attenuation of the EM wave. Any heating of the air by the electron beam was also considered negligible. However, this may not be true if the electron beam is operated at a higher power and for a longer duration than was considered in this study. Also, the only constituent's of the air considered in the rate calculations of the plasma density were oxygen and nitrogen. Other molecules, even though they are found in small concentrations, may have a significant impact on the densities of the plasma constituents.

Experiments to determine the density, spatial distribution, and temporal evolution of the plasma should be performed to verify the results of the EBS and plasma chemistry programs. Measurements of the power attenuation due to a collisional plasma could also be performed to verify the EMWPM program and assess wave propagation in a general class of artificially generated plasmas.

Other recommendations for future work include: A thorough investigation of the parameter space of the electron beam densities and the resulting attenuation and refraction. Also the effects on the complex index of refraction due to a three-component plasma should be investigated due to the majority of the negatively charged species in the air plasma being molecular oxygen ions.

## Appendix A: Derivation of the Radius of Curvature

Starting with the scalar wave equation

$$\vec{\nabla}^2 u + k^2 u = 0 \quad (1)$$

and assuming that the solution to equation (1) is given by

$$u = A e^{ik_0 S} \quad (2)$$

$$k_0 = \sqrt{\epsilon_0 \mu_0} \omega \quad (3)$$

where

A = amplitude factor

S = the eikonal function

where we consider  $u$  to be a rapidly varying function of position and A and S as slowly varying functions of position (Sommerfeld, 1964:330). Substituting equation (2) into the wave equation we obtain

$$\begin{aligned} \frac{\partial u}{\partial x} &= ik_0 u \frac{\partial S}{\partial x} + u \frac{\partial \log A}{\partial x} \\ \frac{\partial^2 u}{\partial x^2} &= -k_0^2 u \left( \frac{\partial S}{\partial x} \right)^2 + 2ik_0 u \left( \frac{1}{2} \frac{\partial^2 S}{\partial x^2} + \frac{\partial \log A}{\partial x} \frac{\partial S}{\partial x} \right) + \\ &u \left( \frac{\partial \log A}{\partial x} \right)^2 + u \frac{\partial^2 \log A}{\partial x^2} \\ \vec{\nabla}^2 u + k^2 u &= -k_0^2 u \left[ \left( \frac{\partial S}{\partial x} \right)^2 + \left( \frac{\partial S}{\partial y} \right)^2 + \left( \frac{\partial S}{\partial z} \right)^2 - \frac{k^2}{k_0^2} \right] + \\ &2ik_0 u \left( \frac{1}{2} \vec{\nabla}^2 S + \vec{\nabla} \log A \cdot \vec{\nabla} S \right) + \dots \end{aligned}$$

where the terms indicated by ..... do not become infinite as  $k_0$  approaches infinity.

Equation (1) is satisfied if S and A satisfy the differential equations

$$\left(\frac{\partial S}{\partial x}\right)^2 + \left(\frac{\partial S}{\partial y}\right)^2 + \left(\frac{\partial S}{\partial z}\right)^2 - n^2 = 0, \quad n = \frac{k}{k_0} \quad (4)$$

$$\frac{1}{2} \vec{\nabla}^2 S + \vec{\nabla} \log A \cdot \vec{\nabla} S = 0 \quad (5)$$

$n$  = index of refraction

Equation (4) is referred to as the differential equation of the eikonal. Equation (5) does not require that the gradient of the logarithm of A be perpendicular to the gradient of S; therefore, it permits discontinuities of A in these directions. If S is equal to a constant value, such as  $x^2 + y^2 + z^2 = C^2$ , then the function  $u$  is at a constant phase, which results in a wave surface. The normal to the wave surface, the gradient of S, is the ray propagation direction. If the index of refraction varies in space then the rays will curve in accordance with equation (4).

In an optically homogenous medium the simplest solution to equation (4) is the linear function

$$S = n(\alpha x + \beta y + \gamma z) \quad (6)$$

where

$$1 = \alpha^2 + \beta^2 + \gamma^2 \quad (7)$$

This solution indicates the waves surfaces are planes, the propagation direction is perpendicular to the plane described by equation (6), and the rays are parallel which is in accordance with geometric optics. Other solutions for an optically, homogenous medium include spherical and cylindrical wave fronts.

The unit vector in the direction of the ray propagation is given by the expression

$$\vec{s} = \frac{\vec{\nabla}S}{|\vec{\nabla}S|} = \frac{1}{n} \vec{\nabla}S \quad (8)$$

The curl of the gradient of any function is defined as zero. This fact gives us the expression

$$\vec{\nabla} \times (\vec{\nabla}S) = \vec{\nabla} \times (n\vec{s}) = 0 \quad (9)$$

According to Sommerfeld, “This condition is equivalent to the existence of the eikonal. All ray bundles (straight or curvilinear) realized in geometrical optics are normals to surfaces and are distinguished from more general systems of curves in that they satisfy the condition (9).”

From Stokes’ theorem we obtain the integral form of equation (9)

$$\oint \vec{\nabla} \times (n\vec{s}) \cdot d\vec{a} = \oint (n\vec{s}) \cdot ds = 0 \quad (10)$$

which results in

$$\int_{P_1}^{P_2} n\vec{s} \cdot d\vec{s} = S_2 - S_1 \quad (11)$$

This indicates that the change in the eikonal is independent of the path of the ray.

From Figure 3, we have the incoming ray,  $\vec{s}$ , tangent to the circle at point P and we have the refracted ray,  $\vec{s}'$ , at  $P'$ . The curvature of the ray is defined as the angle between  $\vec{s}$  and  $\vec{s}'$  divided by the distance  $PP'$

$$|\vec{K}| = \frac{1}{R} = \frac{\theta}{PP'} \quad (12)$$

Since  $|\vec{s}| = 1$ , the angle,  $\theta$ , is equal to  $\vec{s} - \vec{s}'$  and for a very small change in direction, we can make the statement that  $PP' = ds$ . Therefore, we define curvature as

$$\vec{K} = \frac{d\vec{s}}{ds} \quad (13)$$

$d\vec{s}$  = direction of the curvature vector

Using the chain rule on equation (13) in Cartesian coordinates, we obtain

$$\frac{d\vec{s}}{ds} = \frac{\partial \vec{s}}{\partial x} \frac{dx}{ds} + \frac{\partial \vec{s}}{\partial y} \frac{dy}{ds} + \frac{\partial \vec{s}}{\partial z} \frac{dz}{ds} \quad (14)$$

where the full derivative  $\frac{dx}{ds}, \frac{dy}{ds}, \frac{dz}{ds}$  are the components of the  $\vec{s}$  vector. Therefore,

the chain rule can be written in the following form

$$\frac{d\vec{s}}{ds} = \frac{\partial \vec{s}}{\partial x} s_x + \frac{\partial \vec{s}}{\partial y} s_y + \frac{\partial \vec{s}}{\partial z} s_z \quad (15)$$

Since,  $|\vec{s}| = 1$ , then  $|\vec{s}|^2 = 1$  and by taking the gradient of both sides of the equation

$$\frac{1}{2} \vec{\nabla} |\vec{s}|^2 = s_x \vec{\nabla} s_x + s_y \vec{\nabla} s_y + s_z \vec{\nabla} s_z = 0 \quad (16)$$

subtracting equations (15) and (16) results in

$$\frac{d\vec{s}}{ds} = s_x \left( \frac{\partial \vec{s}}{\partial x} - \vec{\nabla} s_x \right) + s_y \left( \frac{\partial \vec{s}}{\partial y} - \vec{\nabla} s_y \right) + s_z \left( \frac{\partial \vec{s}}{\partial z} - \vec{\nabla} s_z \right) \quad (17)$$

The x-component of this vector equation is given by

$$\frac{ds_x}{ds} = s_y \left( \frac{\partial s_x}{\partial y} - \frac{\partial s_y}{\partial x} \right) + s_z \left( \frac{\partial s_x}{\partial z} - \frac{\partial s_z}{\partial x} \right) \quad (18)$$

which using vector identities, it can be shown that

$$\frac{ds}{ds} = (\vec{\nabla} \times \vec{s}) \times \vec{s} \quad (19)$$

By using the identity

$$\vec{\nabla} \times (f \vec{A}) = f \vec{\nabla} \times \vec{A} - \vec{A} \times \vec{\nabla} f \quad (20)$$

with the fundamental equation (9) which characterizes the ray vector,  $\vec{s}$ , we obtain the expression

$$\vec{\nabla} \times \vec{s} = \frac{1}{n} \vec{s} \times \vec{\nabla} n \quad (21)$$

If we substitute equation (21) into (19), we obtain the equation

$$\vec{K} = \frac{1}{n} (\vec{s} \times \vec{\nabla} n) \times \vec{s} \quad (22)$$

Using the “BAC CAB” triple product rule we obtain the final expression for the curvature vector of a ray in an inhomogeneous medium

$$\vec{K} = \frac{1}{n} (\vec{\nabla} n - \vec{s} (\vec{s} \cdot \vec{\nabla} n)) \quad (23)$$

From this we see that the principle normal  $\vec{K}$ , the tangent  $\vec{s}$ , and the  $\vec{\nabla} n$  all lie in one plane (Sommerfeld, 1964:339).

## Appendix B: Input Parameters for the EBS Simulation

This appendix provides a description of the input variables and files used in the EBS simulation. The input file format for the EBS program is the standard Fortran 90 NAMELIST I/O format. The following is an example of the format of the EBeam.inp file

```
! Electron Beam Simulation Input
&start Runs = 1 ,
Power(1) = 30000.0, 30000.0 ,
EEnergy(1) = 100000.0, 1000000.0,
Altitude(1) = 10000.0, 10000.0,
MaxCells(1) = 200.0, 200.0, 200.0, 200.0, 200.0 ,
CellSize(1) = 7.5, 7.5,
SwapSize(1) = 20000, 20000,
MoveNewE(1) = .TRUE. , .TRUE. ,
OutputFile(1) = 'EBeamOutput1.dat' , 'EBeamOutput2.dat' ,
NumSimE(1) = 100, 100 /
```

where

! - Comment

& - start of the NAMELIST input

start – the name of the NAMELIST

Runs – variable, can be any type integer, real, logical, character, etc.

Power(1) – Array, can be an integer, real, logical, or character array. (1) indicates that data input starts in the first element of the array.

/ - end of the NAMELIST input

The input files, Default\_File.dat and Molecule\_Data\_File.dat for the EBS program are the same format, however, only the variables that can be used in the particular file are different. A list of all the variables used in the EBeam.inp file are shown in Table 14. The first column contains the name of the variable, the second column the units for the variable, a brief description of the variables is included in the third column, and the

fourth and fifth columns contain the minimum and maximum values that will be accepted by the EBS simulation.

Table 14. Input Variables to EBS program

Ebeam.inp Run Parameters				
Name	Units	Description	Min	Max
Power	W	Electron beam (Ebeam) power	0.0	10^9
EEnergy	eV	Initial energy of the electrons	0.0	10^6
AirNumDens	#/cm^3	Number density of the air	0.0	10^33
Altitude	m	Altitude of the EBeam	0.0	10^5
BeamRadius*	cm	Radius of electron beam nozzle	10^-3	10^4
PRI	s	Pulse Repetition Interval (PRI) of the electron beam	0.0	10
DutyCycle	#	Percent time that Ebeam is on during the pulse interval	0.0	1.0
Efficiency	#	The efficiency at which the electron gun converts power into electrons	0.0	1.0
NumSimE**	#	Number of initial electrons in the simulation	0	10^5
IonEnergy	eV	Average ionization energy of the atoms or molecules in the simulation	0.0	10^4
MaxCells**	#	Creates a grid that is MaxCells long in the axial direction (X) by 2*MaxCells in the Transverse Direction (Y)	0	1000
CellSize	cm	Size of one side of a cell in the grid	0.0	10^3
RunTime	s	Maximum amount of time that the simulation will run for each electron	0.0	0.01
NumSteps*	#	Number of intermediate parameter values between the min and max value when in analysis mode	0.0	100.0
NRGSTD*	eV	Standard deviation in the distribution of the electron's initial energy distribution	0.0	10^6
AngleSTD*	Radians	Standard deviation in the distribution of the electron's initial angle	0.0	Pi/2
Isotropic	Logical	If true all scattering events are Isotropic		
Ionize	Logical	If true simulates Ionizing events		
Elastic	Logical	If true simulates Elastic Scattering		
InitDist*	Logical	If false electron beam is Monoenergetic, and all electrons have an initial angle of 0.0 rad If true electron beam has a gaussian distribution using NRGSTD and AngleSTD		

NoEjectNRG	Logical	If true ejected electrons have no energy after being ionized from the molecule
ExpAtm	Logical	If true use the exponential atmosphere model to determine air number density If false use AirNumDens value for air number density

### Appendix C: Primary Chemical Reactions in the Plasma

Table 14 provides a list of all the chemical kinetic equations that were used in the plasma chemistry calculations. Column 1 is the reaction number. Column 2 is the reaction process itself. Columns 3 and 4 provide the minimum and maximum values of the rate constant for the molecular temperature or average electron energy range listed in column 5. Column 6 is the source of the data on the rate constant.

Table 15. List of Dominant Chemical Reactions for a Nitrogen-Oxygen Plasma

#	Reaction Process	Rate Constant or Cross-Section	Rate Constant or Cross-Section	Temp. or Avg e <sup>-</sup> Energy	Source
	Attachment – Two Body	Min	Max		
1	$e + O_2 \rightarrow O + O^-$	0	$1.25 \times 10^{-18}$ cm <sup>2</sup> at 6.7 eV	3.6 to 12 eV	McDaniel p 410
	$e + O_2 \rightarrow O_2^-$	$2 \times 10^{-19}$			Niles, Table V, React. 17
2	$e + O \rightarrow O^-$	$1 \times 10^{-15}$			Niles React. 15
	$e + N_2 \rightarrow N + N^-$	Nil	Nil		Alpert p 99
	$e + N \rightarrow N^-$	Nil	Nil		Alpert p 99
	Attachment – Three Body				
3	$e + 2O_2 \rightarrow O_2 + O_2^-$	$6 \times 10^{-31}$	$4 \times 10^{-30}$	100 to 600 K	McDaniel p 411
		$1.4 \times 10^{-29}$		195-600 K	Niles
4	$e + O_2 + N_2 \rightarrow N_2 + O_2^-$	$1 \times 10^{-31}$	$1 \times 10^{-32}$	0.1 to 1 eV	McDaniel p 409
		$1 \times 10^{-31}$		300K	Niles Table V,
5	$e + O_2 + O \rightarrow O^- + O_2$	$1 \times 10^{-31}$			Niles J. Chem Phys 52:408 (1970)

	$e + O_2 + O_2^* \rightarrow O_2 + O_2^-$	$1.9 \times 10^{-31}$			Dettmer p 207
	Electron Recombination - Two Body				
6	$2e + O_2^+ \rightarrow O_2 + e$	$1 \times 10^{-19}$			Niles, Table V, React. 11
7	$e + O_2^+ \rightarrow 2O$	$2.1 \times 10^{-7}$			Niles, Dettmer React. 19
8	$e + O^+ \rightarrow O$	$1.2 \times 10^{-12}$			Alpert p 99
9	$e + N_2^+ \rightarrow N_2$	$1 \times 10^{-12}$			Alpert p 99
46	$e + N_2^+ \rightarrow 2N$	$2.7 \times 10^{-7}$			Niles
	Electron Recombination - Three Body				
10	$e + O_2^+ + M \rightarrow O_2 + M$	$1 \times 10^{-26}$			Niles J. Chem Phys 52:408 (1970)
11	$e + O^+ + M \rightarrow O + M$	$1 \times 10^{-26}$			Niles J. Chem Phys 52:408 (1970)
	Electron Detachment - Two Body				
12	$O^- + O \rightarrow O_2 + e$	$1.9 \times 10^{-10}$			Dettmer p 263 React. 3
13	$O_2^- + O \rightarrow O_3 + e$	$3.3 \times 10^{-10}$			Dettmer p 264 16
43	$O^- + O_2 \rightarrow O_3 + e$	$5.0 \times 10^{-15}$			Niles React. 9
	$O^- + O_2^* \rightarrow O_3 + e$	$3 \times 10^{-10}$			Dettmer p 270 React. 117
	$O_2^- + O_2^* \rightarrow 2O_2 + e$	$2 \times 10^{-10}$			Dettmer p 270 React. 118

14	$O_2^- + O_2 \rightarrow 2O_2 + e$	$1.0 \times 10^{-16}$	$2 \times 10^{-14}$	400 to 600K	McDaniel p 411
		$2.7 \times 10^{-10}$		375 to 600 K	Niles, Table V., React. 21.
15	$O_2^- + N_2 \rightarrow O_2 + N_2 + e$	$1 \times 10^{-16}$	$2 \times 10^{-14}$	400 to 600K	McDaniel p. 411
		$1.9 \times 10^{-12}$		375-600 K	Niles, Table V., React. 20.
44	$O^- + N \rightarrow O_2 + NO + e$	$1 \times 10^{-10}$			Niles
45	$O^- + NO \rightarrow NO_2 + e$	$2.0 \times 10^{-10}$			Niles
34	$O^- + N_2 \rightarrow N_2O + e$	$2.0 \times 10^{-19}$			Niles React. 11
	Additional $O_2^+$ Losses				
16	$O_2^+ + O^- \rightarrow O + O_2$	$9.6 \times 10^{-8}$		69:81	Dettmer p. 263 React. 9
17	$O_2^+ + O^- + M \rightarrow O_3 + M$	$2 \times 10^{-25}$		69:82	Dettmer p. 263 React. 12
18	$O_2^+ + O_2^- \rightarrow O_2 + 2O$	$1 \times 10^{-7}$		70	Dettmer p. 264 React. 29
19	$O_2^+ + O_2^- \rightarrow 2O_2$	$4.2 \times 10^{-7}$		69:81	Dettmer p. 265 React. 43
31	$O_2^+ + N_2 \rightarrow NO^+ + NO$	$1.0 \times 10^{-16}$			Niles React. 119
32	$O_2^+ + N \rightarrow NO^+ + O$	$6.3 \times 10^{-10}$			Niles
	Additional $O_2^+$ Gains				
20	$O^+ + O + M \rightarrow O_2^+ + M$	$1.0 \times 10^{-29}$		70	Dettmer p 264 React. 30
21	$O^+ + O_2 \rightarrow O_2^+ + O$	$2.0 \times 10^{-11}$		69:44	Dettmer p 265 React. 39
	$O_2 + N_2^+ \rightarrow O_2^+ + N_2$	$2 \times 10^{-10}$			See Additional $N_2^+$ Losses

	Additional $O_2^-$ Losses				
	$O_2^+ + O_2^- \rightarrow O_2 + 2O$				See Additional $O_2^+$ Losses
22	$O^+ + O_2^- \rightarrow O_2 + O$	$1.0 \times 10^{-7}$		69:81	Dettmer p 264 React. 23
23	$O + O_2^- \rightarrow O_2 + O^-$	$3.3 \times 10^{-10}$		69:69	Dettmer p 264 React. 26
	$O_2^+ + O_2^- \rightarrow 2O_2$				See Additional $O_2^+$ Losses
	Additional $O_2^-$ Gains				
24	$O^- + O_2 \rightarrow O_2^- + O$			78:124 7	Dettmer p 270 React. 114
	Additional $O^+$ Losses				
25	$O^+ + O^- \rightarrow 2O$	$2.7 \times 10^{-7}$		69:82	Dettmer p 263 React. 8
26	$O^+ + O^- + O \rightarrow O_2 + O$	$2.0 \times 10^{-25}$		69:82	Dettmer p 263 React. 11
	$O^+ + O_2^- \rightarrow O + O_2$				See Additional $O_2^-$ Losses
	$O^+ + O + M \rightarrow O_2^+ + O$				See Additional $O_2^+$ Gains
	Additional $O^-$ Losses				
	$O^+ + O^- \rightarrow 2O$				See Additional $O^+$ Losses
	$O_2^+ + O^- \rightarrow O + O_2$				See Additional $O_2^+$ Losses

	$O^+ + O^- + O \rightarrow O_2 + O$				See Additional $O^+$ Losses
	$O_2^+ + O^- + M \rightarrow O_3 + M$				See Additional $O_2^+$ Losses
	$O^- + O_2 + M \rightarrow O_3 + M$				
	$O^- + O_2 + M \rightarrow O_2^- + O$				See Additional $O_2^-$ Gains
33	$O^- + N_2^+ \rightarrow N_2 + O$	$2.0 \times 10^{-7}$			Niles
35	$O^- + N_2^+ + N_2 \rightarrow 2N_2 + O$	$2.0 \times 10^{-25}$			Niles
	Additional $O^-$ Gains				
	$O + O_2^- \rightarrow O_2 + O^-$				See Additional $O_2^-$ Losses
	Additional $O$ Losses				
	$O + e \rightarrow O^+ + 2e$				See Additional $O^+$ Gains
27	$2O + O_2 \rightarrow 2O_2$	$7.4 \times 10^{-33}$		69:93	Dettmer p 264 React. 28
	$O^+ + O^- + O \rightarrow O_2 + O$				See Additional $O^+$ Losses
28	$2O + M \rightarrow O_2 + M$	$7.4 \times 10^{-33}$		69:93	Dettmer p 265 React. 31
29	$O + 2O_2 \rightarrow O_3 + O_2$	$6.0 \times 10^{-34}$		69:93	Dettmer p 265 React. 32
30	$2O + O_2 \rightarrow O_3 + O$	$6.0 \times 10^{-34}$		69:93	Dettmer p 265 React. 33

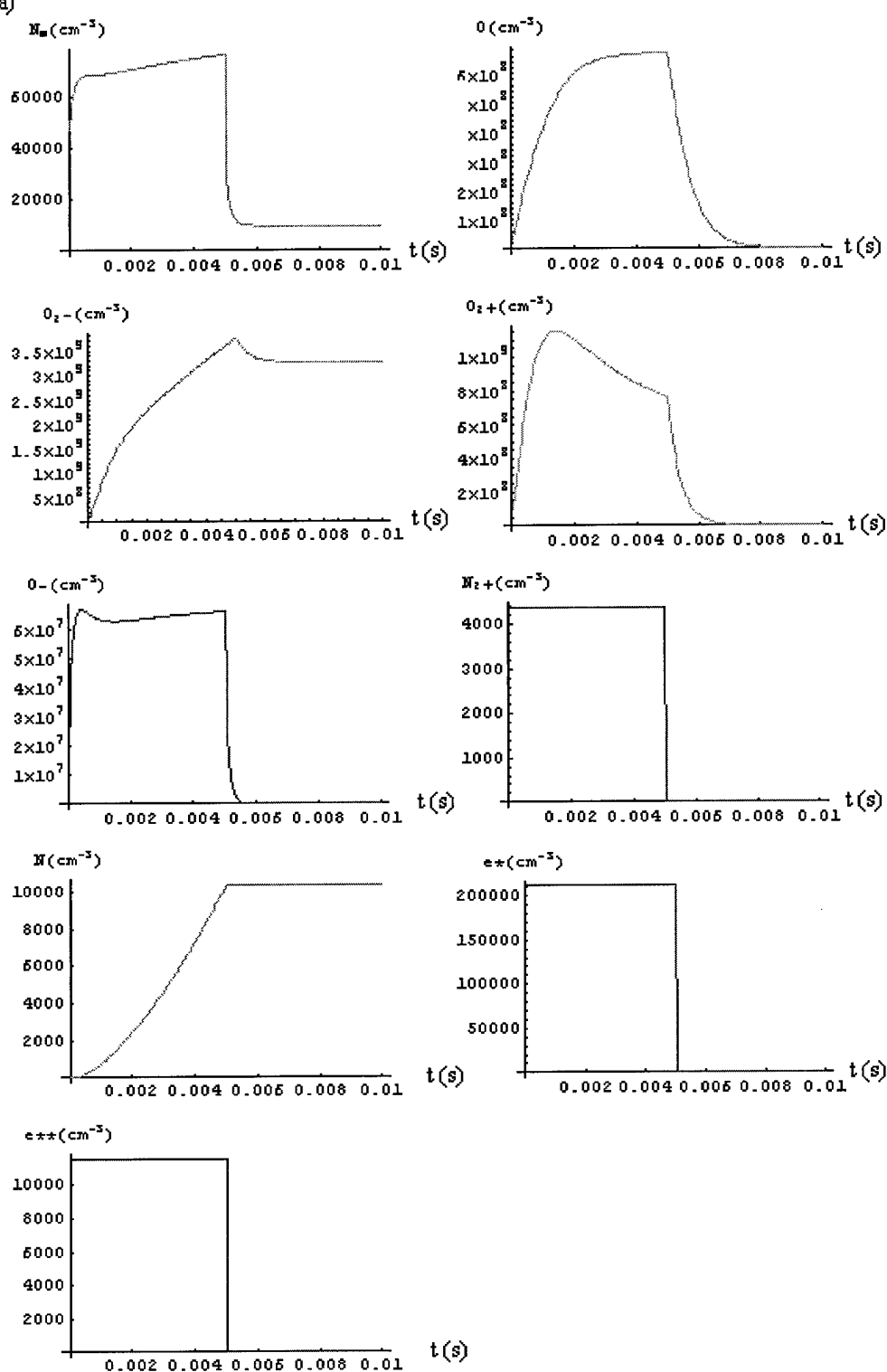
	Additional $O$ Gains				
	$O_2^+ + O^- \rightarrow O + O_2$				See Additional $O_2^+$ Losses
	$O_2^+ + O_2^- \rightarrow O_2 + 2O$				See Additional $O_2^+$ Losses
	$O^+ + O_2 + M \rightarrow O_2^+ + O$				See Additional $O_2^+$ Gains
	$O_2^+ + O_2^- \rightarrow O_2 + 2O$				See Additional $O_2^+$ Losses
	$O^+ + O_2^- \rightarrow O_2 + O$				See Additional $O_2^-$ Losses
	$O^- + O_2 \rightarrow O_2^- + O$				See Additional $O_2^-$ Gains
	$O^+ + O^- \rightarrow 2O$				See Additional $O^-$ Losses
	$O^+ + O_2^- \rightarrow O + O_2$				See Additional $O_2^-$ Losses
	$e + O_2 \rightarrow O^+ + O + 2e$				See Additional $O^+$ Gains
	$O^- + O_2 + M \rightarrow O_2^- + O$				See Additional $O_2^-$ Gains
	Additional $N_2^+$ Losses				
36	$O_2^- + N_2^+ \rightarrow O_2 + N_2$	$2 \times 10^{-7}$			Niles React. 51
37	$O_2 + N_2^+ \rightarrow O_2^+ + N_2$	$2 \times 10^{-10}$			Niles React. 89

38	$O_2 + N_2^+ \rightarrow NO^+ + NO$	$2 \times 10^{-16}$			Niles React. 123
39	$O_2^- + N_2^+ \rightarrow O_2 + 2N$	$1 \times 10^{-7}$			Niles React. 176
40	$N + N_2^+ \rightarrow N_2 + N^+$	$1 \times 10^{-12}$			Niles React. 90
41	$N_2^+ + O \rightarrow NO^+ + N$	$2.5 \times 10^{-10}$			
42	$O_2^- + N_2^+ + N_2 \rightarrow O_2 + 2N_2$	$2.0 \times 10^{-25}$			Niles React. 66

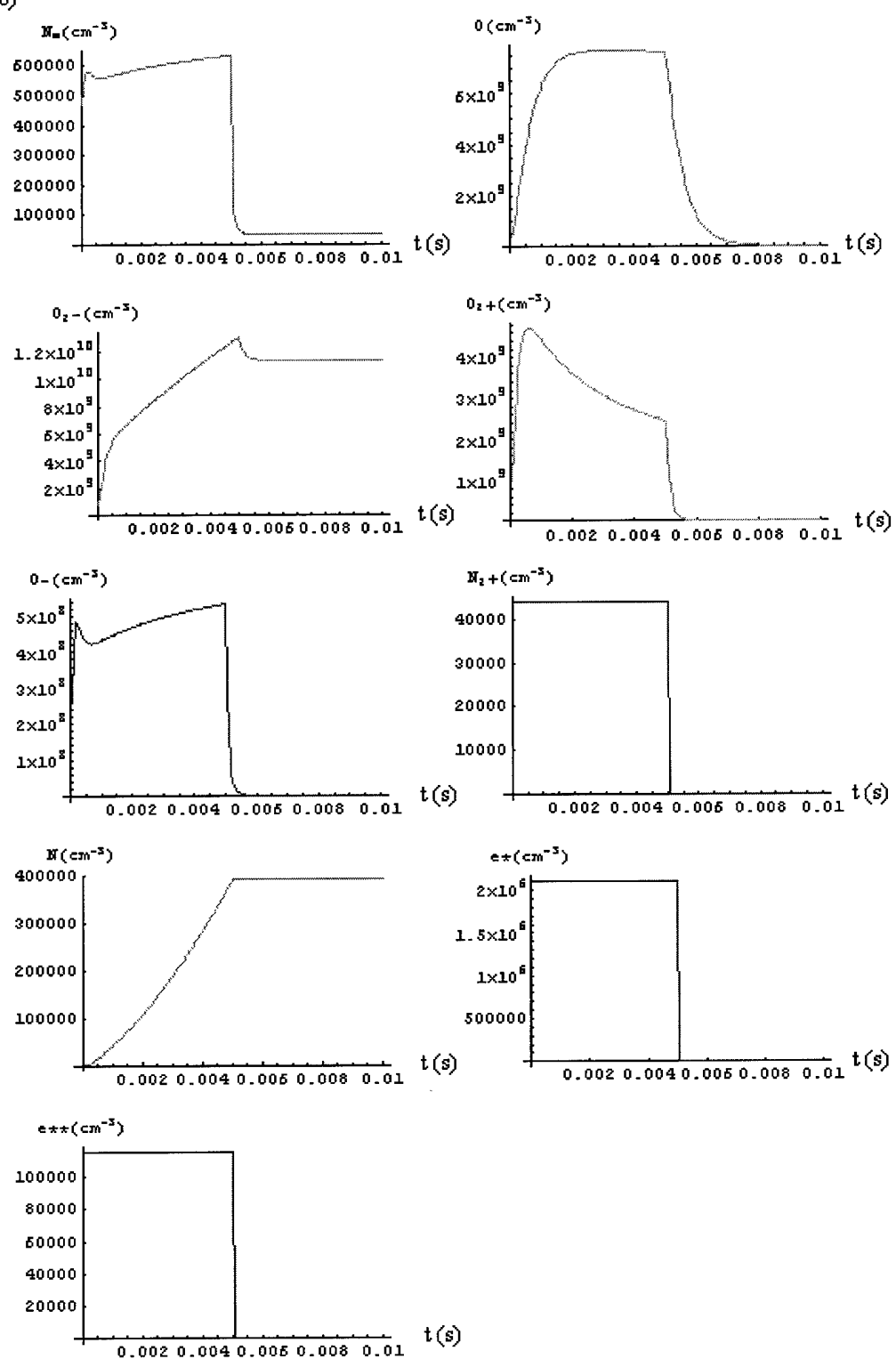
## Appendix D: Results of Rate Equation Calculations

Figure 39 shows a sample of the results of the chemical kinetics calculations with different source term values. The graphs in Figure 39 represent the densities of the constituents of the plasma as a function of time. The graph labeled  $N_e$  is the electron densities in the low thermal electron energy range ( $< 0.1$  eV) as defined in Table 11. The graphs labeled  $e^*$  and  $e^{**}$  are the electron densities in the high and medium energy ranges respectively. All references to reaction numbers in this appendix are referring to the reactions listed in Table 15. For the calculations presented in this appendix the electron beam was turned on for 0.005 s and then turned off. Therefore, these graphs represent the response of the air to an influx of electrons and ions and then the relaxation of the constituents of the plasma after the source has been removed. Figure 39 shows that the most abundant constituents other than molecular nitrogen and oxygen are the positive and negative ions of molecular oxygen. The negative ions of molecular oxygen have a high concentration primarily because of the three-body attachment processes of electrons with molecular oxygen (reactions 3, and 4) in the low and medium energy ranges. The positive ions of molecular oxygen have a high concentration because of charge exchange, reaction 37, which results in a rapid transfer of electrons from neutral oxygen molecules to positive nitrogen ions forming positive oxygen ions and neutral nitrogen molecules. Atomic oxygen and its negative ion are also in plentiful supply because they are a product of the very fast dissociative attachment process given by reaction 1. This analysis is true for the range of source terms shown in Figure 39. Other reaction processes only start becoming dominant at higher electron beam currents.

a)



b)



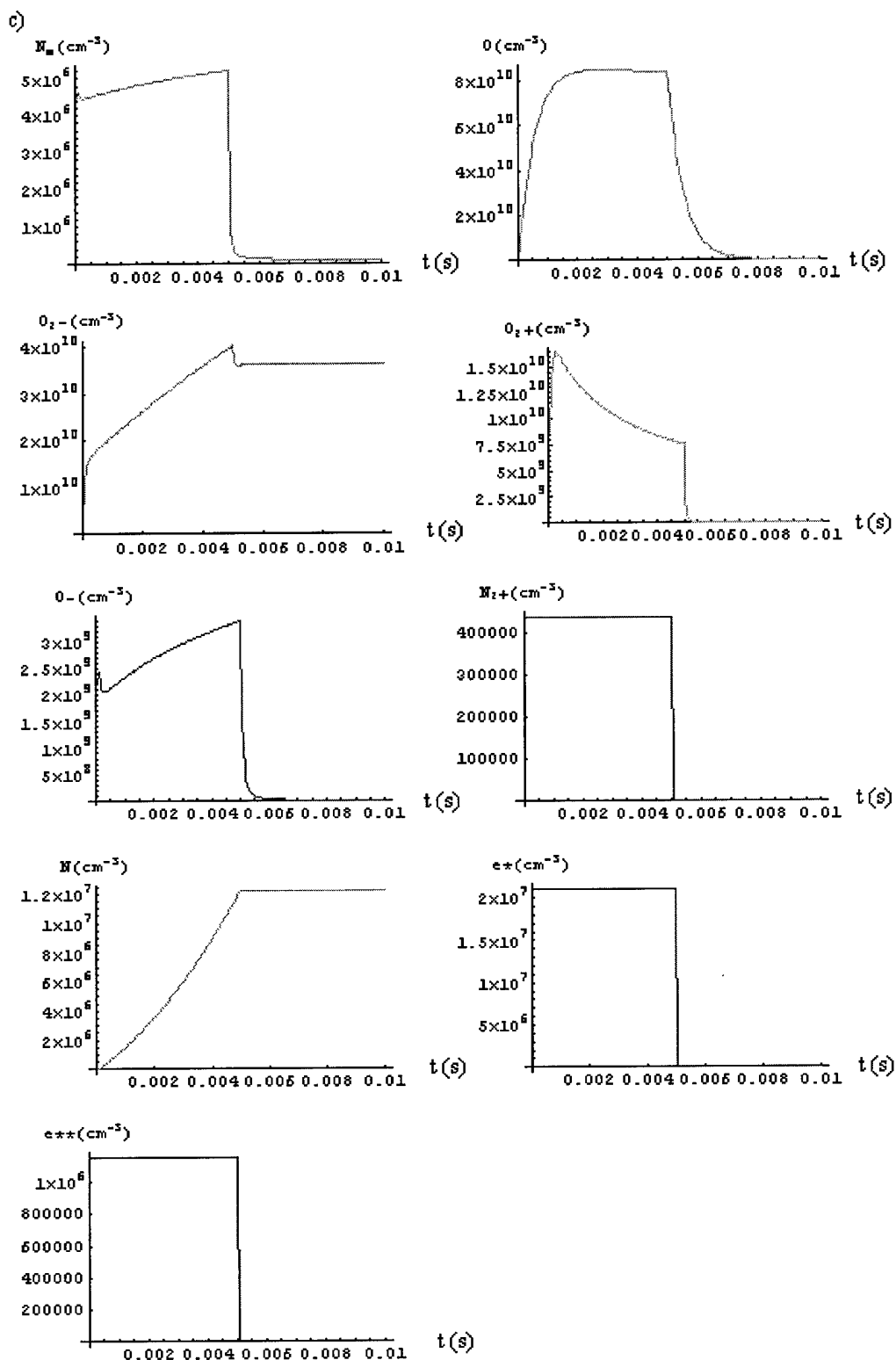


Figure 39. Chemical Kinetics Results for Electron Beam Pulse of 5 ms with Source Terms,  $\gamma$ , of a)  $2 \times 10^{13}$  b)  $2 \times 10^{14}$  c)  $2 \times 10^{15}$

## Bibliography

- Al'pert, Ya. L. Radio Wave Propagation and the Ionosphere. New York: Consultants Bureau, 1963.
- Budden, K.G. Radio Waves in the Ionosphere. Cambridge Ma: Cambridge University Press, 1961.
- Clemmow, P. C. and Dougherty J. P. Electrodynamics of Particles and Plasma. Reading MA: Addison-Wesley Pub. Co., 1978.
- Dettmer, John W. Discharge Processes in the Oxygen Plasma. Air Force Institute of Technology (AU), Wright-Patterson AFB OH, March 1978.
- Digital Visual Fortran. Version 5.0A. CD-ROM. Computer Software. Digital Equipment Corporation, San Diego CA, 1997.
- Evans, Robley, D. The Atomic Nucleus. New York: McGraw-Hill Book Company, 1955.
- Ginzburg, V.L. The Propagation of Electromagnetic Waves in Plasmas. New York: Pergamon Press, 1970.
- Haslegrove, J. "Ray Theory and a New Method for Ray Tracing" The Physics of the Ionosphere: 355-364 (1955).
- Kiemele, Mark J. and others Basic Statistics. Colorado Springs Co: Air Academy Press, 1997.
- Kim, Y.-K., Irikura, K. K., and Rudd, M. E. "Electron-Impact Ionization Cross Sections" n. pag. <http://physics.nist.gov/ionxsec>. 1 September 2000.
- Kim, Y-K., Santos, J. P., and Parente, F. "Extension of the Binary-Encounter-Dipole model to Relativistic Incident Electrons," Physical Review A, 62: 052710-1-052710-13 (Fall 2000).
- Lawson, J.D. The Physics of Charged-Particle Beams. Oxford: Clarendon Press, 1988.
- Lewis, E. E. and Miller, W. F. Computational Methods of Neutron Transports. New York: John Wiley & Sons, Inc. 1984.
- Mathematica for Students. Version 4.0. CD-ROM. Computer Software. Wolfram Research, Champaign IL, 1999.
- McDaniel, Earl W. Collision Phenomena in Ionized Gases. New York: John Wiley & Sons, Inc., 1964.

Mott, N. F. and Massey, H. S. W. The Theory of Atomic Collisions. Oxford: Clarendon Press, 1965.

Niles, Franklin E. Survey of Two-Body and Three-Body Reaction-Rate Coefficients for the Ionized Stratosphere and Mesosphere. Report No. 1702. Aberdeen Proving Ground, Maryland: USA Ballistics Research Laboratories, March 1974.

Niles, Franklin E. "Airlike Discharges with CO<sub>2</sub>, NO, NO<sub>2</sub>, and N<sub>2</sub> as Impurities." Journal of Chemical Physics, 52:408 (1970).

NIST Electron Elastic-Scattering Cross-Section Database. Version 2.0. CD-ROM. Computer Software. U.S. Department of Commerce, Gaithersburg MD, 2000.

Orear, J. and others. Nuclear Physics. Chicago IL: The University of Chicago Press, 1950.

Ramos, David O. A Simulation of Electric Field Driven Electron Drift Limited by Collisions with Gas Mixtures Using a Monte Carlo Null Collision Technique. MS thesis, Wright-State University, Dayton OH, August 1990.

Sommerfeld, Arnold Optics. New York: Academic Press, 1964.

Sturrock, Peter A. Plasma Physics. New York: Cambridge University Press, 1994.

## REPORT DOCUMENTATION PAGE

*Form Approved  
OMB No. 074-0188*

The public reporting burden for this collection of information is estimated to average 1 hour per response, including the time for reviewing instructions, searching existing data sources, gathering and maintaining the data needed, and completing and reviewing the collection of information. Send comments regarding this burden estimate or any other aspect of the collection of information, including suggestions for reducing this burden to Department of Defense, Washington Headquarters Services, Directorate for Information Operations and Reports (0704-0188), 1215 Jefferson Davis Highway, Suite 1204, Arlington, VA 22202-4302. Respondents should be aware that notwithstanding any other provision of law, no person shall be subject to a penalty for failing to comply with a collection of information if it does not display a currently valid OMB control number.

**PLEASE DO NOT RETURN YOUR FORM TO THE ABOVE ADDRESS.**

<b>1. REPORT DATE (DD-MM-YYYY)</b> 03-05-2001			<b>2. REPORT TYPE</b> Master's Thesis		<b>3. DATES COVERED (From - To)</b> Jun 2000 – Mar 2001	
<b>4. TITLE AND SUBTITLE</b>  ATTENUATION AND REFRACTION OF AN ELECTROMAGNETIC WAVE IN AN ELECTRON BEAM GENERATED PLASMA			<b>5a. CONTRACT NUMBER</b>			
			<b>5b. GRANT NUMBER</b>			
			<b>5c. PROGRAM ELEMENT NUMBER</b>			
<b>6. AUTHOR(S)</b>  Lockwood, Nathaniel, P., Captain, USAF			<b>5d. PROJECT NUMBER</b>			
			<b>5e. TASK NUMBER</b>			
			<b>5f. WORK UNIT NUMBER</b>			
<b>7. PERFORMING ORGANIZATION NAMES(S) AND ADDRESS(S)</b>  Air Force Institute of Technology Graduate School of Engineering and Management (AFIT/EN) 2950 P Street, Building 640 WPAFB OH 45433-7765				<b>8. PERFORMING ORGANIZATION REPORT NUMBER</b>  AFIT/GM/ENP/01M-06		
<b>9. SPONSORING/MONITORING AGENCY NAME(S) AND ADDRESS(ES)</b>				<b>10. SPONSOR/MONITOR'S ACRONYM(S)</b>		
				<b>11. SPONSOR/MONITOR'S REPORT NUMBER(S)</b>		
<b>12. DISTRIBUTION/AVAILABILITY STATEMENT</b>  APPROVED FOR PUBLIC RELEASE; DISTRIBUTION UNLIMITED.						
<b>13. SUPPLEMENTARY NOTES</b>						
<b>14. ABSTRACT</b> Artificially generated plasmas may be employed to alter the propagation characteristics of electromagnetic waves. The purpose of this report is to study the propagation of electromagnetic wave in an electron beam generated plasma. To understand the physics related to this concept requires the development of computational tools dealing with a plasma created by an electron beam, an assessment of the temporal and spatial evolution of the plasma, and a characterization of the refraction and attenuation of electromagnetic (EM) waves in a collisional plasma. Three computer programs were developed to characterize the effectiveness of an electron beam generated plasma in refracting and attenuating an EM wave. The spatial extent and density distribution of a plasma generated by a relativistic electron beam was determined using an axisymmetric Monte Carlo model. This plasma density distribution was used as a source term in the second code, a temporal solution of the plasma evolution based on a time dependent analysis of the plasma rate equations. The third code developed, evaluates the attenuation and refraction of an EM wave in the resulting plasma by using a ray tracing method based on the eikonal approach of Sommerfeld. The theoretical foundation and validation procedures are presented for each program. A limited exploration of the dependence of the plasma distribution on neutral density and the electron beam energies was performed. At a neutral density corresponding to 5 km of altitude, the plasma longitudinal extent ranged from 52 to 868 cm and the radial extent ranged from 18 to 292 cm for initial electron energies between 100 keV and 1 MeV respectively. Plasma chemistry plays a critical role in determining the electron plasma density and dictates the beam format required to achieve a desired level of EM wave attenuation.						
<b>15. SUBJECT TERMS</b> Plasma, Electron Beam, Monte Carlo model, Attenuation, Refraction, Eikonal, Eikonal Approach, Plasma Chemistry						
<b>16. SECURITY CLASSIFICATION OF:</b>		<b>17. LIMITATION OF ABSTRACT</b>		<b>18. NUMBER OF PAGES</b> 164	<b>19a. NAME OF RESPONSIBLE PERSON</b> Prof William F. Bailey, ENP	
<b>a. REP ORT</b> U	<b>b. ABST RACT</b> U	<b>c. THIS PAGE</b> U	<b>17. LIMITATION OF ABSTRACT</b>  UU	<b>18. NUMBER OF PAGES</b> 164	<b>19b. TELEPHONE NUMBER (Include area code)</b> (937) 255-3636, ext 4501	

Standard Form 298 (Rev. 8-98)  
Prescribed by ANSI Std. Z39-18

*Form Approved  
OMB No. 074-0188*